

**“Non-adiabatic reaction pathways in the dissociative  
adsorption of Oxygen on an Al(111) surface”**

Dissertation zur Erlangung des  
naturwissenschaftlichen Doktorgrades  
(Dr. rer. nat.)

dem Fachbereich Chemie  
der Universität Essen  
vorgelegt von

**Marcello Binetti**

aus Brindisi (Italien)

Essen, 2001

Tag der Disputation: 3 August 2001

Vorsitzender: Prof. Dr. Reinhard Zellner

1. Gutachter: Prof. Dr. Eckart Hasselbrink

2. Gutachter: Prof. Dr. Aart W. Kleyn

Die vorliegende Arbeit wurde in der Zeit von Februar 1996 bis Dezember 2000 am Fritz-Haber-Institut der Max-Planck-Gesellschaft in Berlin, am Physik Institut der Odense Universität, Denmark, und am Institut für Physikalische und Theoretische Chemie der Universität Essen unter der Leitung der Prof. Dr. Eckart Hasselbrink durchgeführt.

Hiermit bestätige ich, die vorliegende Arbeit nur mit den angegebene Hilfsmitteln, ohne fremde Hilfe angefertigt zu haben.

# Abstract

In the present work the results of an experimental study on the initial stages of aluminum oxidation are reported.

Despite a long-standing theoretical and experimental effort, this process still presents some puzzling characteristics. Among them, the direct, activated character of the chemisorption process: the initial sticking coefficient  $S_0$  is approximately 1% for thermal molecules,  $E_i = 0.025$  eV, but rises to 90% at  $E_i = 0.9$  eV.

This findings are at variance with the results of recent *density functional theory* calculations, predicting near unity reaction probability, even at low  $E_i$ . In an attempt to clarify the dynamics of the initial stages of the oxidation process, I investigated the O<sub>2</sub>/Al interaction by means of molecular beam and laser spectrometric techniques (resonantly enhanced multiphoton ionization - REMPI). The results of the present work, coupled to the finding of *scanning tunneling microscopy* investigations performed by A.J. Komrowski and A.C. Kummel of the University of California, provide compelling evidence for the existence of an abstractive pathway for the dissociation of oxygen on aluminum.

The REMPI study also allowed to highlight the dependence of the abstraction coefficient on both the translational and rotational energy of the incoming oxygen molecules.

# Contents

<b>1. Introduction</b>	<b>1</b>
1.1 Dynamics of gas-surface interactions	1
1.1.1 Potential energy surfaces (PES)	1
1.1.2 Adiabatic vs. non-adiabatic reactions	4
1.1.3 Energy dissipation	4
1.1.4 Direct vs. precursor mediated processes	5
1.2 O <sub>2</sub> chemisorption on metals: a brief review	7
1.3 Why study O <sub>2</sub> /Al(111)?	8
1.4 This work	11
<b>2. Experimental</b>	<b>12</b>
2.1 The Ultra High Vacuum chamber (UHV)	13
2.2 The Molecular Beam	18
2.2.1 The velocity distribution	19
2.2.2 Rotational vs. vibrational cooling	22
2.2.3 Clustering	24
2.3 The Laser	25
2.4 The High Vacuum chamber (HV)	26
2.5 Electronics for synchronization and data acquisition	27
2.5.1 Data acquisition chain for the oxidation experiment (in UHV)	28
2.5.2 Data acquisition chain for the laser calibration experiment (in HV)	29
<b>3. REMPI of oxygen atoms</b>	<b>31</b>
3.1 Spectroscopy of oxygen atoms	32
3.2 Laser's wavelength calibration	33
3.3 The background	35
<b>4. Experimental Results</b>	<b>40</b>
4.1 The instrumental function of the REMPI-ToF spectrometer	40
4.2 Detection of recoiled O-atoms from the abstractive chemisorption	43
4.3 Energetic distribution of the recoiled atoms	46
4.4 O-atoms emission as function of the incident angle	50
4.4.1 The molecular beam intensity	55
4.5 O-atoms emission as function of the oxygen dose	56
4.6 O-atoms yield as function of Etrans of the molecular beam	57
4.6.1 Probability for the abstraction reaction	60
4.6.2 About the experimental uncertainty	67
<b>5. Discussion</b>	<b>70</b>
5.1 On the reaction dynamics	75
5.2 Abstraction probability vs. incident polar angle	76
5.3 O-atom yield vs. Surface coverage (Q)	79
5.4 Abstraction probability vs. Beam Energy	80
5.4.1 Effect of the vibrational excitation	83

5.4.2 Effect of the rotational excitation .....	84
5.5 A brief review of recent theoretical studies .....	88
5.6 Toward a reaction model .....	91
<b>6. Concluding remarks .....</b>	<b>94</b>
Appendix A .....	96
Appendix B .....	97
References .....	99
Publications .....	106
Acknowledgements .....	107
Curriculum Vitæ .....	109

## 1. INTRODUCTION

Oxidation reactions are of enormous importance in a variety of fields ranging from metallurgy to heterogeneous catalysis and (micro)electronics. They have been subject to intense studies for many years but, due to their complexity, they are not yet fully understood at the molecular level. According to a generally established view, the actual oxide growth is preceded by an *induction period*. This can be divided into sequential stages, each characterized by increasing levels of gas exposure. Initially, oxygen molecules approach a clean surface. Part of these molecules adsorb and dissociate. The resulting atomic fragments end up chemisorbed on that surface (*dissociative sticking*). At higher exposures, a chemisorbed layer is formed. Eventually, the nucleation of the oxide sets in. In real life, the situation can be complicated by the existence of intermediate molecular precursor states, by the overlapping of the three ideal stages, the coexistence of different chemisorbed phases, the diffusion of chemisorbed atoms toward inner layers and surface reconstruction. In the present work, I restricted myself to the study of the initial stage of dissociative chemisorption.

Dissociative sticking involves the breaking of molecular bonds and the rearrangement of the surface bonds to accommodate the adsorbate. It represents an important step, often the rate limiting one, in the gas-surface reactions. Therefore, much theoretical and experimental work has been devoted to its characterization. Hydrogen dissociation on metal surfaces has served as a model system for the general class of bond-breaking processes at surfaces [Gross, 1998]. This reaction is well understood and modeled in terms of density functional theory (DFT) within the local density approximation (LDA), with some corrections taking non-local effects into account. A comparably clear picture has not yet arisen for reactions involving more complicated diatomic molecules, like  $O_2$ . As the brief review in Section 1.2 will show,  $O_2$  reactions with metal surfaces originate a wide variety of different chemisorption mechanisms. This has been attributed both to the higher reactivity of  $O_2$  as compared to  $H_2$ , and to the presence of equivalent electrons in the half-filled binding molecular orbital (Highest Occupied Molecular Orbital - HOMO) of  $O_2$ . The latter requires the inclusion of electron correlation effects in the models, considerably increasing the complexity of the theoretical analysis. A further complication arises from the possible non-adiabatic character of the charge transfer processes leading to  $O_2$  dissociation [Katz, 1999]. Hence, to foster our understanding of  $O_2$  dissociative chemisorption on metals, a different model system is needed. In the remainder of this chapter, I will show that the  $O_2/Al(111)$  interaction is a suitable candidate for such role.

### 1.1 DYNAMICS OF GAS-SURFACE INTERACTIONS

Before proceeding with the discussion of  $O_2$  chemisorption, it is opportune to introduce some basic concepts and terminology relative to the interaction of gases with surfaces. Classical mechanics can provide useful examples to this end.<sup>1</sup>

#### 1.1.1 Potential energy surfaces (PES)

Let us consider a ball rolling on a horizontal surface toward a wall. A trough is located along the wall, as shown in Fig. 1.1. If the ball is always in contact with the surface, it follows the minimum potential energy path. The ball would acquire its lowest

---

1. This section is mainly based on the excellent review published by George Darling and Stephen Holloway [Darling, 1995] and on the PhD thesis of Lars Österlund [Österlund, 1997-PhD].

potential energy, if it could fall into the trough. This is prevented by the barrier located at the trough's rim. Some kinetic energy is needed to overcome this barrier. On the other hand, if the kinetic energy is high enough, the ball may bump against the wall and be reflected back on the plane.<sup>1</sup>

This situation is similar to the one experienced by a gas molecule hitting a surface, as can be easily seen replacing the ball and the wall with a molecule and a surface, respectively. Fig. 1.1 is also useful as a conceptual picture of a *potential energy surface* (PES). In principle, the PES contains all the information relative to the interaction between the gas molecule and the surface. If it could be solved completely, it would describe the interaction exactly. If one considers that the density of atoms present at a solid surface is of the order of  $10^{16}/\text{cm}^2$ , this would require the solution of equations with  $\approx 10^{16}$  variables, clearly an impossible task. However, a thorough description of dissociative chemisorption can usually be attained with PES of much smaller dimensionality, as it has been shown for the  $\text{H}_2/\text{Cu}$  system [Hammer, 1994].

A cut along the parallel to the ball trajectory in Fig. 1.1 would describe its interaction with the wall as a function of their reciprocal distance. It corresponds to the *potential energy curve* (PEC) for the interaction, and it is the one-dimensional analogous of the PES. Besides being of historical interest, PECs are still widely used because they allow to get an insight in the dynamics of the reaction at surfaces.<sup>2</sup> In such cases, the potential of the molecule-surface system is usually plotted as a function of the *reaction coordi-*

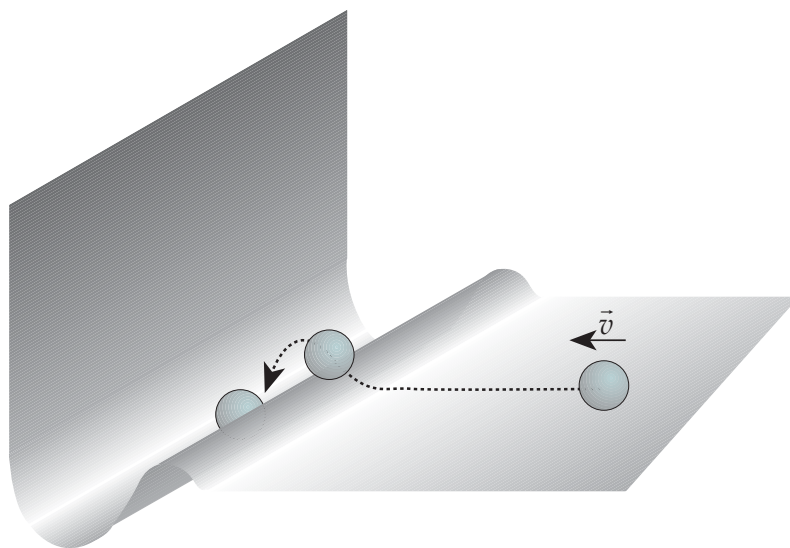


*Fig. 1.1: Illustration of the concept of a potential energy surface. The trajectory of the ball is determined by the topography of the surface. Its energy will be minimal when it moves along the trough. If the wall and the ball are respectively replaced by a surface and a molecule, this picture illustrates the lowering in the potential energy for a molecule upon adsorption. The corrugation before the trough represents an adsorption barrier.*

1. It is worth mentioning that, if no dissipative forces (*i.e.* friction) were present, the ball would not get trapped in the configuration of lowest potential energy (*i.e.* the trough).
2. The very idea of PES, introduced by Lennard-Jones in his seminal work on dissociative chemisorption of  $\text{H}_2$  on metal surfaces, was formulated in terms of one-dimensional PECs [Lennard-Jones, 1932].

nate, which represents the motion of the system through a number of degrees of freedom. An example of a two-dimensional PES is given in Fig. 1.2.a), where an *elbow potential* is shown. The Z-axis represents the distance of the molecular center-of-mass from the surface and the r-axis represents the molecular bond length. These are the most important coordinates for a qualitative understanding of dissociation processes at surfaces. The *reaction path* coordinate system is also illustrated in Fig. 1.2.a). The reaction path is a curved trajectory along the PES, often taken to be the path of the steepest descent from the barrier maximum. In this case, the motion of the particle is divided into two components: a tangential motion (parallel to the vector  $\mathbf{s}$ ) along the trajectory, and a vibrational motion (parallel to the vector  $\mathbf{p}$ ) normal to it. The vibration at large Z is the one of the incoming molecule. It evolves gradually into the vibration of the products (*i.e.* the two dissociated atoms) as the molecule approaches to the surface. The advantage using reaction path coordinates is, that the dynamical behaviour of a system can be qualitatively described in terms of vibrationally adiabatic (effective), one-dimensional potentials. Some examples are shown in the panel b) of Fig. 1.2, where the two cases of early (E) and late (L) dissociation barrier in the reaction region are shown.

The PES in Fig. 1.2.a) is much more than an ideal example: such *elbow potentials* allowed to correctly model the dissociative chemisorption of  $\text{H}_2$  on Cu(111), highlighting the role played by the molecular vibrational excitation in the promotion of dissociative sticking [Hammer,1994]. At the same time, this conceptual framework allowed a

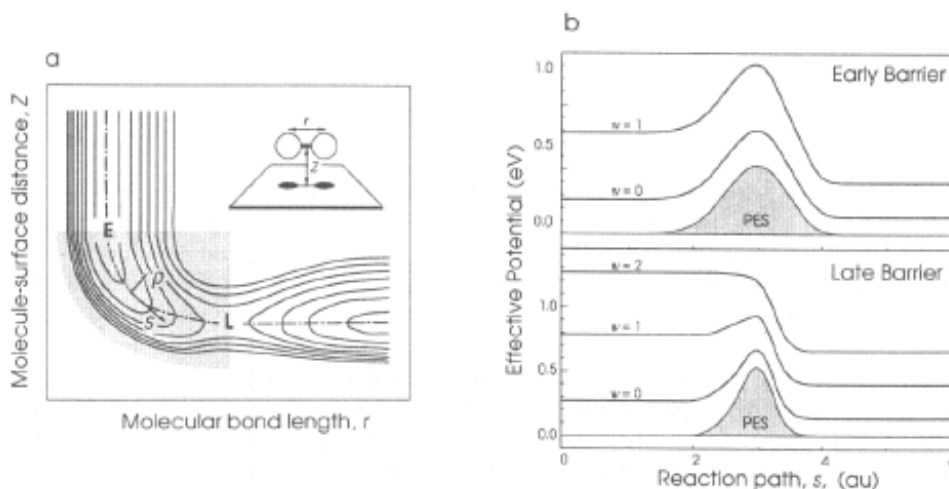


Fig. 1.2: a) Example of two-dimensional PES, the so-called “elbow potential”. The two coordinates are the distance of the molecule center-of-mass from the surface ( $Z$ ) and the molecular bond length ( $r$ ). The reaction path coordinate system is illustrated by the two vectors named  $\mathbf{p}$  and  $\mathbf{s}$ . The two cases of early (E) and late (L) dissociation barrier in the reaction region (shaded area) are shown. b) Vibrationally adiabatic effective potentials for early and late barrier PESs. The “vibrational mass” of the molecule increases from the reduced mass to the total mass as the molecule moves through the reaction region, causing a drop of the vibrational levels. In case of an early barrier, this phenomenon occurs after the barrier crossing and does not affect the dynamics. For a late barrier, the same event results in a vibrational state dependent decrease in the barrier height [Darling, 1995].

natural explanation for the vibrational excitation of H<sub>2</sub> and D<sub>2</sub> molecules backscattered from the Cu(111) surface, as measured by Rettner *et al.* [Rettner, 1992].

### 1.1.2 Adiabatic vs. non-adiabatic reactions

Usually, the huge differences in the electronic and nuclear masses results in a comparable difference between electrons and nuclei velocities. In this case, their motions can be separated: the nuclei appear static to the electrons, whose distribution set up the potential governing the motion of the former. This is the *Born-Oppenheimer approximation* (BOA), also known as *adiabatic approximation*.<sup>1</sup> In the example in Fig. 1.1, this would correspond to a ball *always* in contact with the surface, while rolling over the barrier and into the trough. If its velocity is too high, the ball may jump over the barrier, and fly until it hits the wall or falls into the trough. During its flight time, the ball is not in its energetic ground state. Something similar takes place when the nuclear velocity becomes comparable to the electronic one: then the BOA may break down and the motion of the adsorbing molecules must not be confined to the electronic ground state anymore.

The existence of such processes has been demonstrated in a number of cases, for highly electronegative species (*e.g.* halogens or O<sub>2</sub>) interacting with alkali metal or semiconductor (Si) surfaces [Greber, 1995; Jensen, 1995]. The current interpretation of these phenomena is based on the model originally proposed by Brako and Newns to explain the occurrence of non-adiabatic charge transfer processes upon scattering of atom at surfaces [Brako, 1989]. When a molecule approaches a surface, its affinity level is broadened and lowered so much, that it crosses the Fermi energy of the system. At low translational energies, this level is progressively occupied by electrons from the substrate (adiabatic process). At high translational energies, the affinity level might survive unoccupied. In this case, the incoming molecule evolves on an electronically excited branch of the PES and the process is non-adiabatic. When the level is eventually filled, the excess energy of the system can be dissipated through radiative emission, Auger decay or emission of negatively charged halogen or oxygen atoms.

The understanding of non-adiabatic processes has ripened in the context of halogen and O<sub>2</sub> interaction with alkali metals. A comprehensive review on this topic has recently been published by Greber [Greber, 1997].

Some evidence for non-adiabatic charge transfer processes, has also been found in the context of O<sub>2</sub>/Al interaction. Studies performed by Kasemo and coworkers in the early '70s showed that oxygen chemisorption on metal films caused photon emission with a probability of about 10<sup>-7</sup> per incoming molecule [Kasemo, 1974]. This was interpreted as evidence for the existence of a non-adiabatic reaction pathway [Kasemo, 1979]. Nevertheless, due to the lack of structural characterization of the metal films, the role of the surface defects could not be elucidated.

Further considerations on the non-adiabaticity of O<sub>2</sub>/Al(111) interaction will be presented in Chapter 5.

### 1.1.3 Energy dissipation

Energy dissipation must take place, if a molecule or its fragments are to be trapped at a surface. The excess energy is usually dissipated in the heat bath of the solid, whereas

---

1. The term *adiabatic approximation* indicates that the system evolves on a single adiabatic state.

the non-adiabatic scenario constitutes a remarkable exception. In the classical limit, the energy exchange between an incoming particle of mass  $m$  and a surface atom of mass  $M$ , is given by the so called Baule formula [Baule, 1914]

$$\Delta(T_s) = \frac{4\mu}{(1+\mu)^2} \left( E_i - \frac{1}{2} kT_s \right) \quad (1.1)$$

where for  $T_s$  is the surface temperature,  $\mu$  is the mass ratio  $m/M$  and  $E_i$  is the kinetic energy of the incoming particle.<sup>1</sup> The efficiency of the energy transfer has its maximum when the mass of the incoming particle matches the mass of the scattering center, a condition almost ideally satisfied in the scattering of  $O_2$  molecules ( $m=32$  a.u.) with Al atoms ( $m=27$  a.u.).

Another available channel for energy dissipation is the creation of electron-hole ( $e-h$ ) pairs. It is certain that atom scattering induces electronic excitation of the surface, since Amirav and Cardillo measured a transient current induced by Xe atoms scattered at an InP(100) surface [Amirav, 1986]. They estimated that 5% of the energy loss was due to electronic excitation, in the range between 2 and 10 eV for the energy of the incident atoms. The microscopic dynamic of the process is extremely complex to model and is still unclear. Moreover, due to the weak chemical interaction in that system, it is not self-evident how those results might be extended to the case of reactive scattering. This topic will be further discussed in Section 5.1

#### 1.1.4 Direct vs. precursor mediated processes

It is usual to classify dissociative chemisorption processes as either *direct* or *precursor mediated*. In direct processes, the molecule may proceed through different intermedi-

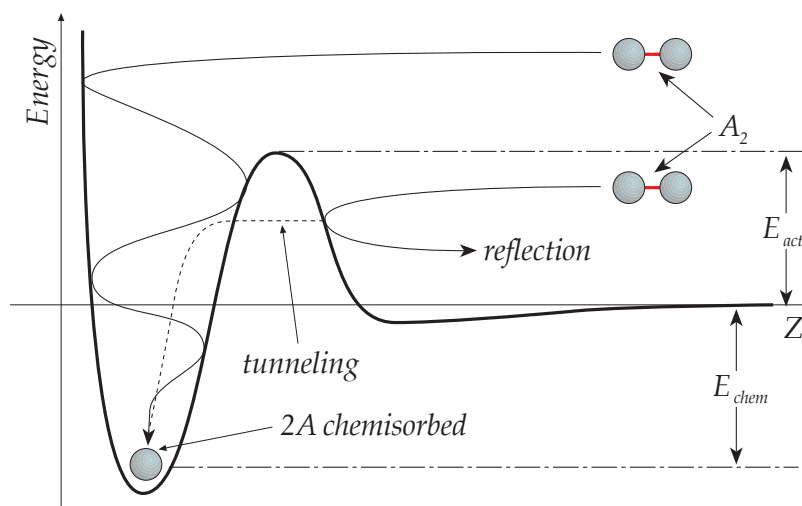


Fig. 1.3: One-dimensional sketch of direct chemisorption. If the kinetic energy of the molecule is enough to overcome the dissociation barrier  $E_{diss}$ , it can directly dissociate and access the chemisorbed state. If the kinetic energy is lower than  $E_{act}$ , the molecule may still tunnel through the barrier or, more likely, scatter away.  $E_{chem}$  is the chemisorption energy.

1. This formula is valid if  $\Delta(T_s)$  is much larger than the upper limit of the phonon band edge, so that quantum effects can be neglected.

ate states, but it will not reside in any of them for a long time.<sup>1</sup> Therefore, the dissociation probability will strongly depend on the dynamics of the incoming molecules. This situation is sketched in Fig. 1.3: if the incoming molecule  $A_2$  has enough energy, it can directly overcome the chemisorption barrier and dissociate. At energies lower than  $E_{act}$ , the molecule has still a finite probability to tunnel through the barrier to reach the dissociatively chemisorbed state. In this case, however, the most likely outcome is non-reactive scattering.

A precursor mediated process is sketched in Fig. 1.4, where the incoming molecule is trapped for a long time in an intermediate state of energy  $E_{prec}$ , before the reaction proceeds. This molecule can thermalize with the substrate and lose the information about its initial dynamical state. In this case, the dissociation will be determined by the substrate temperature, not by the dynamical parameters of the incoming molecule. The latter may desorb while attempting to overcome the activation barrier toward dissociation. In this case, the molecule will leave the surface in thermal equilibrium with the former, with an energy  $E_{th}$ . The life-times of molecular precursor states can be so long, that their spectroscopical detection is possible [Gland, 1980]. At the other extreme, their life-times can be so short, that only partial thermalization is attained. In this case, the final state of the desorbed molecule will still bear some dependence on the initial state [Kleyn, 1996].

In this brief introduction, I focused onto one-dimensional potentials, assuming that the knowledge of the interaction potential as a function of the distance  $Z$  between its center of mass and the surface is sufficient to characterize the gas-surface reaction. It should be borne in mind, that often the reaction dynamics may be understood only if the role of the internal molecular degrees of freedom is taken into account [Hammer, 1994].

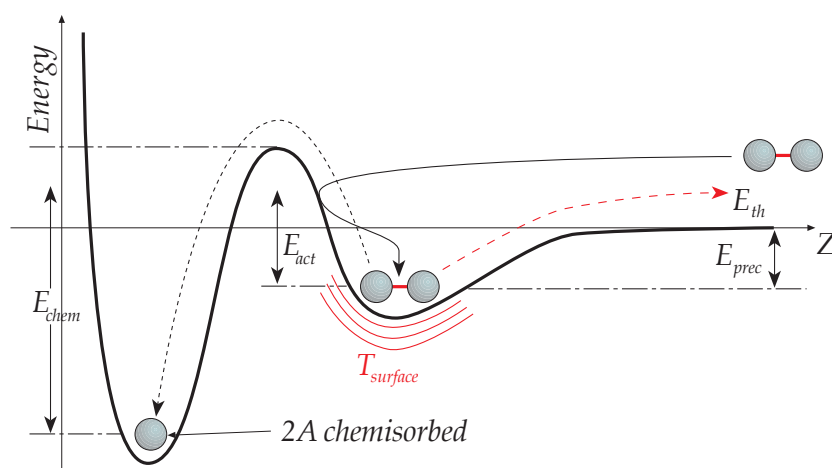


Fig. 1.4: One dimensional sketch of precursor mediated chemisorption. The molecule is trapped in a molecular precursor state, where it can thermalize with the surface. Thermal energy from the substrate allows the molecule to overcome the barrier toward dissociation. During this last reaction step, the molecule may gain enough energy to desorb.

1. These time scales are not absolute, and must be evaluated in each specific case.

## 1.2 O<sub>2</sub> CHEMISORPTION ON METALS: A BRIEF REVIEW

As already mentioned, dissociative chemisorption of oxygen on metal surfaces is a complex process. It involves multiple charge transfer steps, probably non-adiabatic, between adsorbate and substrate [Katz,1999]. The translational energy  $E_{\text{trans}}$  of the incoming molecules can promote their dissociative chemisorption on the surface. This may happen either directly or through the population of a molecularly chemisorbed precursor state (a process briefly termed as *direct molecular* chemisorption). A direct process has been demonstrated for oxygen chemisorption on W(110) and Cu(100) [Hall,1993]. The chemisorption of O<sub>2</sub> on Ru(001) presents two different regimes: direct molecular chemisorption at low O<sub>2</sub> translational energies ( $E_{\text{trans}} < 100 \text{ meV}$ ) and direct chemisorption at higher energies [Davis,1997 and references therein]. Whenever direct chemisorption is active, no evidence for a stable molecularly chemisorbed state at low coverages and low temperatures has been found. The initial sticking coefficient,  $S_0$ , was observed to increase with the translational energy of the incoming molecules and to scale with the normal translational energy.<sup>1</sup>  $S_0$  was found to be independent of the substrate temperature  $T_s$ , apart from Ru(001). The latter system presents the peculiarity of a  $S_0$  growing with  $T_s$  at  $E_{\text{trans}} < 100 \text{ meV}$ , whose interpretation is still not clear [Wheeler,1996].

The existence of a stable, low coverage and low temperature molecularly chemisorbed state does not necessarily imply the existence of a direct molecular pathway for the chemisorption. An example in this sense is given by the adsorption of thermal O<sub>2</sub> on the hexagonally reconstructed surface of Pt(100).<sup>2</sup> O<sub>2</sub> adsorbs molecularly on this surface at 123K, but desorbs without dissociation when the sample is heated. This behaviour suggests a one-dimensional potential energy surface for this system, with a molecularly chemisorbed state and a large barrier toward dissociation. A similar situation has been recently demonstrated for Ag(110), where the chemisorption of O<sub>2</sub> at 75K lead to the population of two distinct chemisorbed states  $\alpha$  and  $\beta$ . Only one of them, namely  $\beta$ -

**Table 1.1: Adsorption mechanism for O<sub>2</sub> on selected metal surfaces**

Direct molecular chemisorption	Direct dissociation	Ambiguous mechanisms
O <sub>2</sub> /Pt(111)	O <sub>2</sub> /W(110)	O <sub>2</sub> /Pt(100)-hex
O <sub>2</sub> /Ag(110)	O <sub>2</sub> /Cu(100)	O <sub>2</sub> /Ag(110)
O <sub>2</sub> /Ir(110)	O <sub>2</sub> /Ru(001) <sup>b</sup>	
O <sub>2</sub> /Ir(111)		
O <sub>2</sub> /Pd(111)		
O <sub>2</sub> /Ru(001) <sup>a</sup>		

Notes: <sup>a</sup> $E_{\text{trans}} < 100 \text{ meV}$ ; <sup>b</sup> $E_{\text{trans}} > 100 \text{ meV}$ .

1. Although  $E_{\text{trans}}$  is a scalar, it is usually decomposed into two components relative to the surface (normal and parallel), like the molecular velocity. For a molecule approaching the surface at an angle  $\theta$  from the normal, the component of the molecular velocity normal to the surface scales as  $\cos\theta$ . The normal translational energy is defined as  $E_{\text{trans}} \cos^2\theta$  [cf. Section 4.4].
2. The Pt(100) surface reconstructs into the more stable Pt(100)-hex-R0.7 structure.

$O_2$ , is a precursor to dissociation at higher temperature. Upon heating,  $O_2$  trapped in the  $\alpha$ -state desorbs intact [Bartolucci, 1998].

Direct molecular chemisorption has been demonstrated for Pt(111), Ag(110), Ir(110), Ir(111) and Pd(111) [Davis, 1997; Kolasinski, 1994]. In these cases, the existence of a stable molecularly chemisorbed state was coupled to an increase of  $S_0$  with  $E_{\text{trans}}$  and an inverse dependence of  $S_0$  on the  $T_s$ . This is interpreted as a thermally-driven, kinetic competition between dissociation and desorption from the molecularly chemisorbed, intermediate state.

Noteworthy is also the case represented by the  $O_2/Ag(111)$  system, an example of precursor mediated dissociative chemisorption, where more than one precursor state is involved [Kleyn, 1996].

### 1.3 WHY STUDY $O_2/Al(111)$ ?

The brief review above, gives evidence of the complexity of the  $O_2$  chemisorption process. Model systems are needed, that might allow comparison of theoretical predictions with experiments. For both practical and theoretical reasons, the  $O_2/Al$  interaction might become one of those model systems. From an applicative standpoint, aluminum is interesting because it is the lightest among the metals used for structural purposes. It readily oxidizes in air, building a thin (of the order of 10 atomic layers), extremely stable oxide layer which prevents further corrosion of the bulk metal. Aluminum is also widely used in microelectronics to realize both electrical connections and metal/oxide junctions. From a scientific viewpoint, it is a prototypical *free electron metal*, whose properties are relatively simple to model (jellium metal). Hence, the electronic structure of this metal offers the possibility to directly investigate the contribution of  $s$  and  $p$  electrons to the chemisorption energy. This is an important feature, considering that the interaction between the metal  $s$  and  $p$  electrons and non-metal adsorbates is found to be the principal contributor to the energetics of the metal-adsorbate bonding. Clearly, interactions between the orbital of the adsorbate and the  $d$ -orbital of the metal are also important for transition metal system, but even in those cases most of the adsorption energy comes from the  $s$ ,  $p$  interactions. [Whitten, 1996]

Among aluminum low indexes surfaces, the (111) shows the most marked jellium-like properties [De Santis, 2000]. Its interaction with oxygen has been investigated in a number of studies [Batra, 1984]. Nevertheless, the dynamics of the chemisorption reaction is still poorly understood. For example, it is well-known that the initial sticking coefficient ( $S_0$ ) of Al(111) exposed to thermal oxygen is very low (approx.  $10^{-3}$ ). This has been a long-standing problem, since O/Al chemisorption is estimated to be highly exothermic (7.5 eV) and even the most recent calculations indicate, that a dissociation barrier should affect only rare entrance channels, if any [Jacobsen, 1995; Yourdshahyan, 2001]. In a recent molecular beam study, Österlund *et al.* have demonstrated that the initial sticking coefficient,  $S_0$ , is strongly dependent on the translational energy of the incoming molecules [Österlund, 1997]. The mechanism responsible for this effect is yet unclear.

The publication of the seminal STM study of Brune *et al.* on the initial stage of oxygen chemisorption on Al(111) at room temperature, stirred a considerable debate and is one of the main motivations for the present work. In their study, Brune and coworkers imaged the surface of an Al(111) single crystal by STM, after exposure to  $O_2$  from the

background [Brune, 1992]. Exposure to  $O_2$  caused the appearance of protrusions on the metal surface, which were identified as isolated chemisorbed O-atoms. An initial sticking coefficient  $S_0=0.005$  for  $O_2$  was determined. The distance between two nearest adsorbates was estimated by means of the following statistical analysis of adatom densities in the STM images. First the density of O-atoms around a given one was calculated, as the ratio of the number of O-atoms in an annulus of given radius centered on that adatom, to the area of the annulus. This procedure was repeated for several atoms and for increasing distances, yielding the adatom density as a function of the reciprocal adatom distance. Then, the average of this function for all adatoms was normalized to the adatom density of the whole image. The width of the used annuli was  $40\text{\AA}$ . The obtained density distribution scattered little around the value of 1, showing that the atoms were randomly distributed over the surface. An estimate of  $80\text{\AA}$  was given, for the mean separation of the adatoms,  $d_{\text{sep}}$  [Brune, 1993]. The adsorption sites showed no correlation up to a coverage  $\Theta=0.015$ , then islands started to build up. Formation and growth of islands continued with increasing oxygen exposure. Oxide nucleation started around  $\Theta = 0.2$ , well before the saturation of the first monolayer for chemisorbed oxygen. The sticking coefficient was reported to drop with increasing oxygen exposure. In an attempt to rationalize the unusually high value of  $d_{\text{sep}}$ , it was proposed that the incoming oxygen molecules might chemisorb with their axis parallel to the surface, dissipating the excess energy as translational motion of their fragments parallel to the surface (“hot adatoms”).

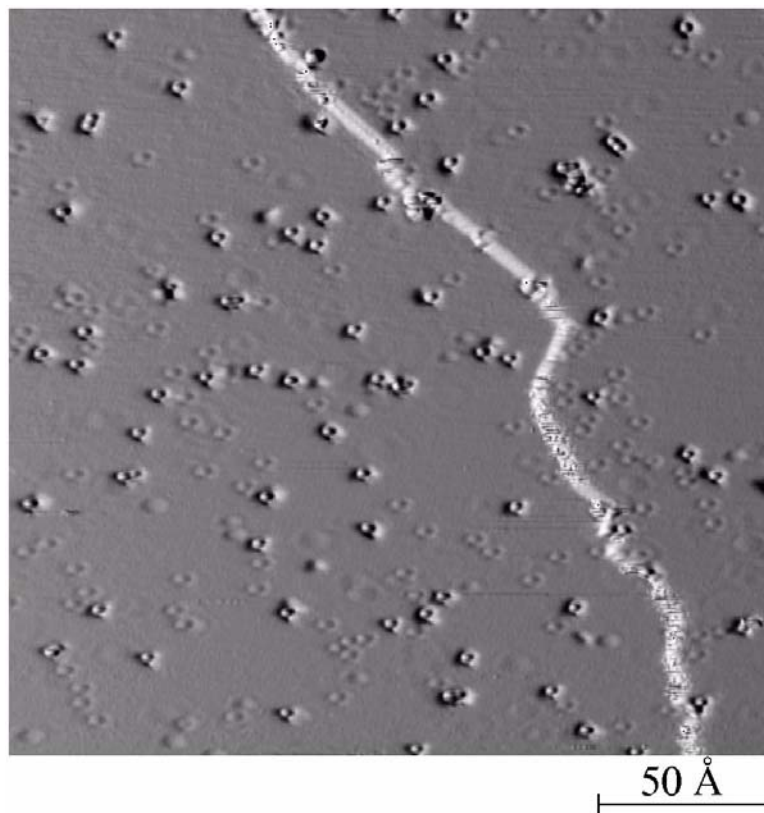


Fig. 1.5: STM image of two adjacent terraces of the Al(111) surface covered by 66 single O-atoms and 6 pairs. Oxygen coverage  $\Theta=0.020\text{ML}$  ( $I_t=8\text{nA}$ ,  $V_t=-0.5\text{V}$ ). Grey scale according to height. [Brune, 1992].

The interpretation of the adsorbate distance in terms of hyperthermal motion of hot adatoms has been critically reviewed and essentially discarded in two theoretical studies. Modeling the transient motion of O-adatom on Al(111) by means of molecular dynamics and an effective medium model potential, Engdahl and Wahnström found that atoms moving close to the surface should experience a highly corrugated potential, leading to a fast randomization of the trajectories [Engdahl, 1994]. Upon comparison of the available STM data with the results of their simulation, they proposed a value of the order of 50 Å for the experimental  $d_{\text{sep}}$ , but confirmed the random character of the adatom distribution. However, according to their calculations, an initial energy of 9.5 eV per atom was required to reproduce the experimental value for  $d_{\text{sep}}$ . On the contrary, an initial energy of 2.83 eV per atom, closer to the expected values for the dissociative chemisorption of O<sub>2</sub> on Al(111), could not account for separations higher than 10 Å. Similar results were obtained by Wahnström *et al.* in a later dynamical simulation on model potentials fitted to first principle data [Wahnström, 1996; Jacobsen 1995]. They also pointed out that atoms moving further away from the surface should experience a less corrugated potential, leading to more elongated trajectories. For molecules dissociating with their axis pointing away from the parallel to the surface, the inner fragments should chemisorb directly at the impact point. The outer fragments instead, might move along a “cannonball”-like trajectory. While spending a considerable part of their flight-time away from the surface, the recoiling atoms would move on a smooth PES, experiencing a lower electronic friction and landing far away from the dissociation point.

Moreover, the chemisorption energy of one single oxygen atom is sufficient to break the O<sub>2</sub> molecular bond. Hence, depending on the details of the energy release and on the orientation of the molecular axis prior to dissociation, at least a fraction of the recoiling atom should be able to permanently escape from the surface, resulting in an abstraction process. The two envisioned mechanisms, *hot-adatoms* dissociation and *abstractive/cannonball* dissociation, are shown respectively in the upper and lower panels of Fig. 1.6.

If abstractive dissociation takes place, oxygen atoms should be released in front of the aluminum surface during the oxidation process. Their detection would demonstrate the existence of an abstraction channel for this reaction. The present work was expressly conceived to check the validity of this hypothesis.

Although exotic at first sight, the existence of abstraction mechanisms has been proved for a number of systems, where chemical species with high electron affinities (typically halogens) interact with alkali metals or semiconductors [Strömquist, 1996; Li, 1995; Jensen, 1995]. Abstraction has been invoked to explain the emission of negative oxygen ions during the oxidation of alkali metals [Greber, 1997]. While the present work was in progress, the availability of an abstraction pathway in the interaction of halogens with Al(111) has been also demonstrated [Pettus, 2000].

Recently, two different STM studies reopened the controversy about the very interpretation of Brune’s STM image. According to the interpretation of Varga’s group in Vienna, the features on the surface should be non-resolved pairs of O-atoms [Leonardelli, 2000]. Similar measurements performed in Kummel’s group supported the original interpretation of the protrusions as single atoms [Komrowski, 2001]. The latter interpretation is also supported by the results of a density functional study performed in the group of Nørskov [Jacobsen, 1995].

A broader discussion on this topic and a review of recent theoretical works will be presented in Chapter 5.

#### 1.4 THIS WORK

In this study, molecular beam and laser spectrometric techniques were used to investigate the availability of an abstractive pathway for the aluminum oxidation reaction. An Al(111) single crystal in a ultra high vacuum (UHV) vessel was exposed to a controlled amount of oxygen by means of a pulsed molecular beam. At the same time, a laser tuned to the opportune frequency was focused in front of the sample, to resonantly ionize the atoms possibly emitted during the oxidation process. A Time-of-Flight (ToF) mass spectrometer was used to detect the resulting O-ions. The present work constitutes the first experimental proof for abstraction as a dominating reaction path for the interaction of oxygen with a metallic system.

In the next Chapter, I will describe the experimental apparatus. Chapter 3 is devoted to an introduction into the Resonantly Enhanced Multi-Photon Ionization (REMPI) spectrometry and the problem of discriminating the signal from the background. The experimental results are presented in Chapter 4 and discussed in Chapter 5. Chapter 6 contains a brief summary of this work. A list of the acronyms and symbols used in the text is given in the Appendixes.

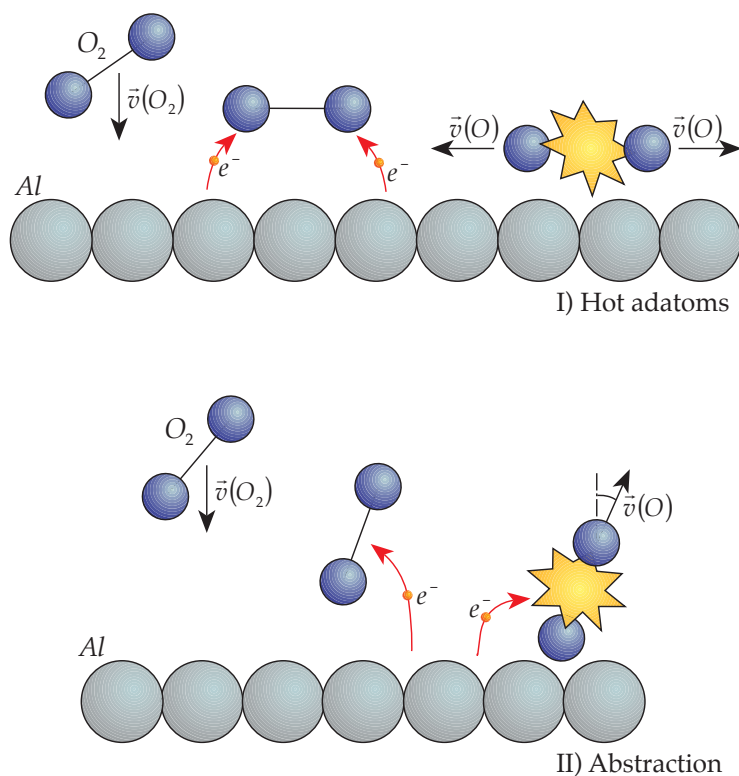


Fig. 1.6: Pictorial view of the mechanisms proposed for  $O_2$  dissociative chemisorption on Al(111). The incoming molecule may approach the surface under two different geometries: parallel (side-on) or almost perpendicular (head-on). I) In the first case, two hyperthermal fragments are released. II) In the second case, one fragment is directly absorbed. Its counterpart may permanently escape the surface.

## 2. EXPERIMENTAL

Experiments were performed to check the possible emission of oxygen atoms during the first stage of aluminum oxidation at room temperature. Two different apparatuses, an Ultra High Vacuum (UHV) chamber and a High Vacuum (HV) chamber, were available. The two chambers were equipped with similar home-built ToF mass spectrometers. The HV chamber was used for laser and ToF spectrometer calibration. The actual oxidation experiment was performed in the UHV chamber, exposing an aluminum sample to a controlled and reproducible amount of  $O_2$  by means of a three-stage, differentially-pumped molecular beam. The oxygen atoms emitted during the oxidation process were resonantly ionized using a tunable dye laser and detected with the ToF mass spectrometers.

The experimental setup, sketched in Fig. 2.1, is described in the remainder of this chapter. It can be grouped in the following functional units:

- the UHV chamber;
- the molecular beam;
- the laser;
- the HV chamber ;

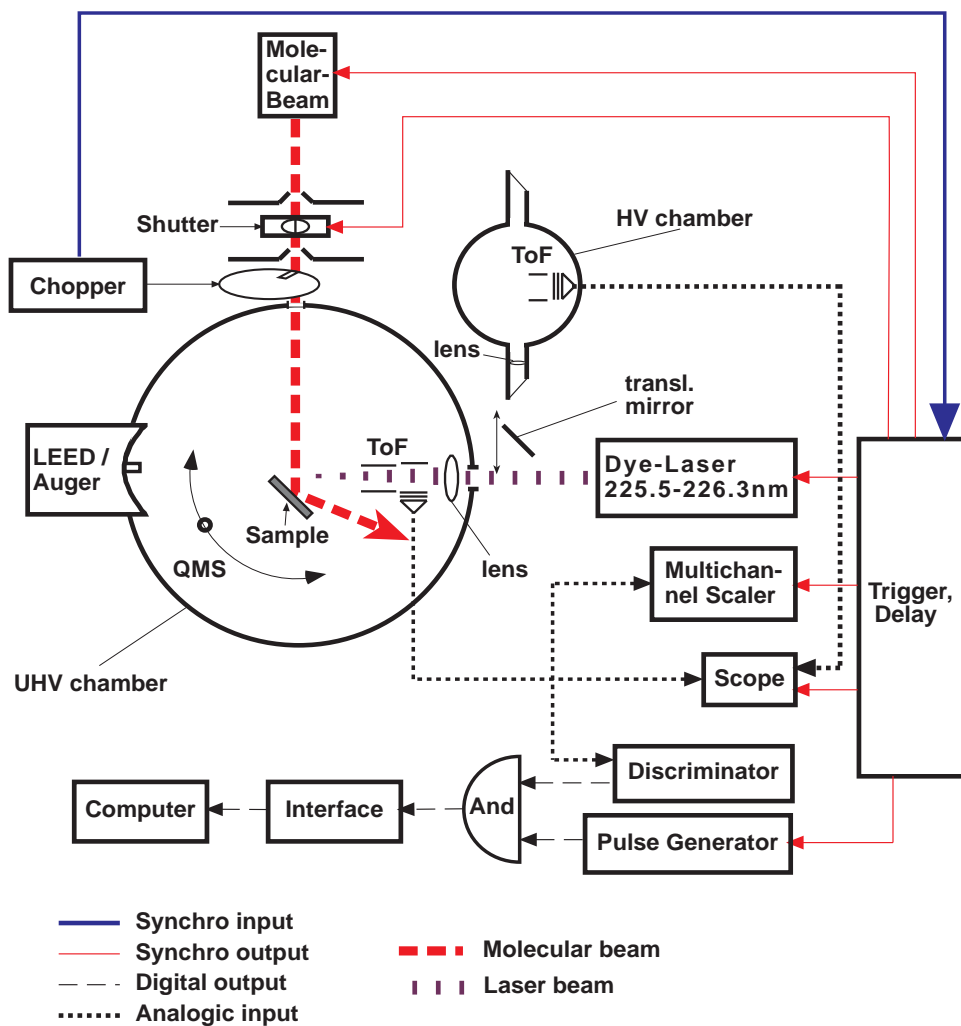


Fig. 2.1: Block diagram of the experimental apparatus.

- electronics for laser and molecular beam synchronization and for data acquisition.

## 2.1 THE ULTRA HIGH VACUUM CHAMBER (UHV)

The UHV chamber was described in detail elsewhere [Engel, 1978]. It is a stainless steel vessel, composed of two half-cylinders. Each of them has a diameter  $\varnothing$  of 60 cm and a height  $h$  of 70cm. The two halves are joined by a copper sealed Wheeler flange. The chamber is pumped to a base pressure in the low  $10^{-10}$  mbar by a combination of three parallel pumping system:

- a water cooled turbomolecular drag pump (Pfeiffer TMU521), with a pumping speed of 520l/s and a nominal base pressure of  $5 \cdot 10^{-11}$  mbar; this is backed by a Rotary Vane Vacuum pump (Pfeiffer DUO 016 B) with a pumping speed of 4l/s and a nominal base pressure of  $10^{-4}$  mbar; a zeolite trap (Caburn) is inserted between the two pumps to prevent backstreaming of oil vapors from the rotary pump through the turbopump and into the UHV chamber;
- an ion-getter pump (Varian 9210066) with a pumping speed of 400l/s;
- a titanium sublimation pump.

Both the ion-getter and the titanium sublimation pumps are located in the lower half of the chamber. The turbopump is connected to the upper half of the chamber through a CF 150 flange. The pressure at the forepump is measured with a Pirani manometer. The pressure in the UHV chamber is measured with an ionisation gauge. Both of the gauges are driven by a VG IGC 26 control unit.

A commercial (VAB) manipulator is located in the upper part of the chamber. It has a XY-stroke of  $\pm 25$  mm with  $\pm 5 \mu\text{m}$  resolution parallel to the ground, a Z-stroke of 50 mm with  $\pm 5 \mu\text{m}$  resolution. The manipulator supports a home built,  $LN_2$  cooled cold finger, that can be rotated  $360^\circ$  around its Z axis with a precision of  $\pm 0.5^\circ$  [Bornscheuer, 1997]. The cold finger supports a home built sample holder, shown in Fig. 2.2. It is made of copper and can be easily cooled down to  $90 \pm 0.2$  K.

The sample is a disk of  $\varnothing = 10$  mm, cut from a high purity aluminum single crystal (purity=99.999%). Its face is aligned perpendicular to the (111) direction, to a precision

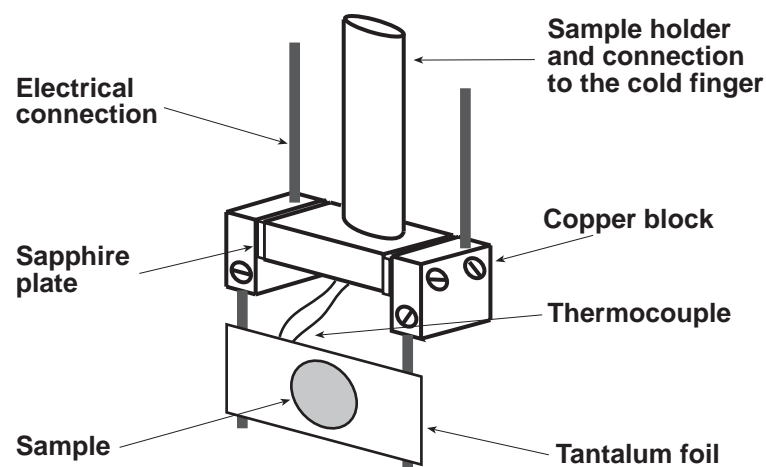


Fig. 2.2: Schematic view of the sample holder mounted in the UHV chamber. The reader is referred to the text for its description.

of  $\pm 0.5^\circ$ . It has been used in previous UHV-STM investigations [Wintterlin, 1988]. The sample is held between two tantalum foils (thickness=0.075 mm), spotwelded to two tungsten wires ( $\varnothing=1$  mm). These wires are held in the two copper blocks located at the end of the sample holder. Two sapphire plates electrically isolate the copper blocks from the rest of the sampleholder, but allow thermal connection with the cold finger. The crystal can be resistively heated, by means of a DC voltage applied to the tungsten wires: the tantalum foils, heated by this current, heat the crystal conductively. The heating rate can be varied between 1 and 10.0 K/s. For the present work, it was fixed to 3.0 K/s. The temperature is measured by two pairs of type K thermocouples, spotwelded on the tantalum supporting foils close to the sample.

In the upper half of the chamber are also present:

- a movable Low Electron Energy Diffraction (LEED)/Auger electron gun (Varian 981-2125) with a coaxial four grids retarding optic (Varian 981-0127) for LEED/Auger analysis;
- an all-metal bakeable straight-through valve (Varian 951-5052), connecting the molecular beam and the UHV chamber;
- a sputter gun (Leybold IQE 10/35) for *in situ* surface preparation;
- a home-built Resonantly Enhanced Multi-Photon Ionization (REMPI) ToF mass spectrometer.

The crystal was cleaned by means of repeated cycles of sputtering with  $\text{Ar}^+$  ions accelerated to a kinetic energy of 500 eV [Wintterlin, 1988]. The cleanliness of the surface was assessed by means of Auger Electron Spectroscopy (AES). It is known, that the LMM Auger transition for metallic Al, which is located at 68 eV, is shifted to 54 eV upon oxidation [Michel, 1980]. AES spectra of the surface, recorded after venting the system, showed the 54 eV peak, a 272 eV peak due to carbon contamination and a 510 eV peak due to the KLL transition of oxygen. Sputtering cycles were repeated until the peak at 68 eV reached saturation and the other peaks disappeared. The Al-LMM signal is almost 40 times more intense than the O-KLL one, at excitation energies of 3 kV [Davies, 1976]. Due to the different relative intensities of the two transitions, the saturation of the metallic Al signal (68 eV peak) was always reached *after* the O-KLL signal had disappeared. Hence, saturation of the Al-LMM signal was interpreted as a proof of the sample cleanliness. Once cleaned, the sample was annealed to 700 K, to recover the long-range order of the surface. Annealing cycles of 10 minutes at 700 K were repeated until LEED images of the surface were characterized by bright spots and lack of a diffuse background, denoting a well-ordered surface. After venting the chamber, the cleaning procedure required extended sputtering (up to some hours). To recover a clean surface between single experimental runs, one cycle of 15' sputtering followed by a 10' annealing cycle was usually sufficient.

The home-built ToF spectrometer has been described in detail elsewhere [Nessler, 1996]. The scheme in Fig. 2.3 shows its working principle. The laser beam enters the UHV chamber through a quartz Brewster window. The use of Brewster windows instead of normal flat viewports minimizes transmission losses due to reflection. A 250 mm lens and two  $90^\circ$  prisms are rigidly connected to the ToF-tube. All of the laser optics used in these experiments were made of UV-grade fused silica, an amorphous form of silicon dioxide, characterised by high UV transmission, a low thermal expansion coefficient and a high laser damage threshold. The first prism steers the laser light paral-

l to the sample and the entrance of the ToF-tube. The lens focuses the laser beam at a fixed distance from the tube, along its axis. Here, atoms or molecules are ionized, which will be eventually detected by the Multi-Channel Plates (MCPs). The second prism reflects the laser light onto a second Brewster window and out of the UHV chamber. This, together with the *off-axis* positioning of the MCP's, allows to minimize the noise due to laser stray light.

The ToF-tube is a stainless-steel cylinder, whose ends are closed by a high-transparency metal mesh. It constitutes a Faraday's cage, and its inner region is free from electrical fields. A negative voltage is applied to the cylinder to extract the positive ions from the laser focus region located ca. 2 cm in front of the tube. Inside the tube, four electrostatic deflectors help steering the ions. Different ionized species have approximately the same kinetic energy as they enter the ToF-tube. But, due to their different *charge-to-mass* ( $q/m$ ) ratio, their velocities are different. Therefore, ions with different  $q/m$  ratio will need different times to cross the ToF-tube. The ratio between the flight times, two different ions  $a$  and  $b$  need to cross a given ToF-tube, can be calculated applying the energy conservation principle:

$$t_a = t_b \sqrt{\frac{m_a q_b}{q_a m_b}}. \quad (2.1)$$

Since the delays are a function of the  $q/m$  ratio of the ions considered, the ToF-tube acts as a mass spectrometer. At the other end of the tube, another electrostatic deflector ( $90^\circ$  deflector) steers the mass-selected ions toward a chevron stack of MCPs (MCP, Galileo, 1397-1900), with a  $\Delta V$  of 2000 V across them. Since two different ions reach the detector at *different times*, their MCP signal will also be separated in time. Actually, Eq. 2.1 only holds for the flight time of the ions through the ToF-tube, which cannot be measured. The flight time experimentally determined, is the one the ions need to travel from the laser focus, through the ToF tube, to the MCPs, where they are detected. So Eq. 2.1 is

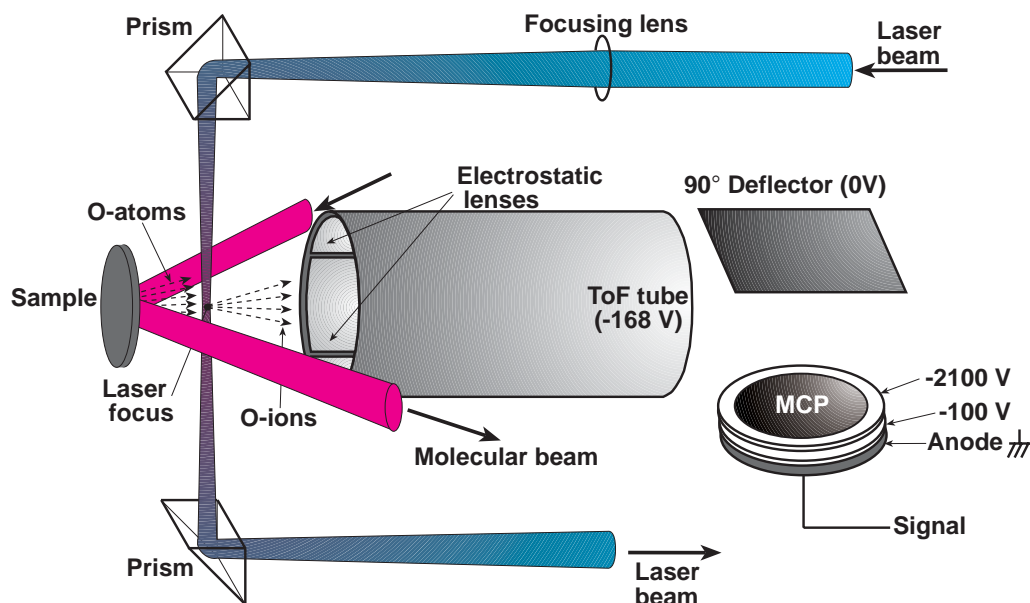


Fig. 2.3: Scheme of the REMPI-ToF spectrometer. A detailed explanation of its working principle is given in the text.

expected to be valid only as an approximation. Nevertheless, for a 8 cm long ToF-tube and an extraction potential of -160V, the difference between experimental and calculated delay time for  $O^+$  and  $NO^+$  is less than 5%. The REMPI-ToF spectrometer is mounted on two threaded bars and can be moved. In this way, its distance relative to the sample can be varied.

The detection efficiency ( $\Sigma$ ) of the spectrometer was estimated by means of a computer simulation using a commercial software (MacSimion, v. 2.04). The trajectories of O-ions moving in the electrical field generated by the potentials applied to the ToF-tube, were calculated for a set of randomly generated values of initial velocities and orientations of the ions. The distribution of both energy and starting point was gaussian. The potentials are listed in Fig. 2.4. The ratio of the number of trajectories ending onto the MCPs to the total number of the calculated ones, gives an estimate of  $\Sigma$ . It was found close to 80%. A typical diagram showing the calculated trajectories is depicted in Fig. 2.4. The efficiency for O-atoms detection was also determined experimentally. This procedure is presented in detail in Section 4.1, together with a more detailed analysis of the ion flight time within the spectrometer.

The choice of the focusing lens in Fig. 2.3 deserves a further comment, because of its effect on the sensitivity of the experimental setup. The focal length ( $f$ ) determines the waist of the focused beam, which governs both the laser fluence ( $\Phi$ ) and the physical dimension of the volume where REMPI detection can take place.  $\Phi$  is defined as the flux of photons (#) through a surface normal to the direction of propagation of the light beam, normalized to the surface area. If the beam waist is circular, with radius  $w_0$ , then

$$\Phi = \frac{\#}{\pi w_0^2}. \quad (2.2)$$

$\Phi$  is an important parameter because the intensity of a  $n$ -photon transition is proportional to the  $n$ -th power of the fluence [Section 3.1]. To determine accurately the laser active volume ( $V_L^{act}$ ), it cannot be neglected that the beam waist grows slowly with the distance

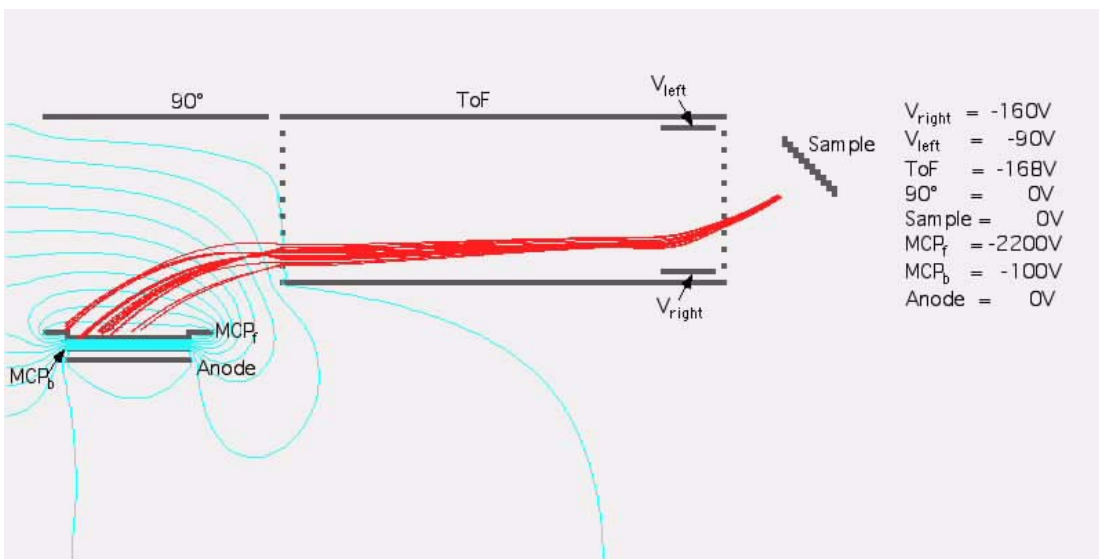


Fig. 2.4: Simulated trajectories of the ions through the ToF spectrometer (Simulation software: MacSimion 2.04).

from the focus. In order to understand qualitatively the effect of  $f$  on  $V_L^{act}$ , the latter can be approximated with a cylinder of a given height ( $h$ ), whose base radius is  $w_0$  [Section 4.6.1]. If the number density of O-atoms ejected per gas pulse during the oxidation reaction  $n_o$  varies smoothly near the laser focus, the number of atoms available for the ionization process will be proportional to the detection volume. Given that both the cross-sections governing the (2+1)REMPI process,  $\sigma^{(2)}$  and  $\sigma_{pi}$  [Section 3.1], are independent from the laser fluence, the intensity ( $I$ ) of the measured signal can be written as

$$I = n_o \cdot (h\pi w_0^2) \sigma^{(2)} \sigma_{pi} \Phi^3, \quad (2.3)$$

and, eventually,

$$I = n_o \cdot (h\pi w_0^2) \sigma^{(2)} \sigma_{pi} \left( \frac{\#}{\pi w_0^2} \right)^3. \quad (2.4)$$

If lenses with short  $f$  are chosen (tight focusing), the beam waist  $w_0$  decreases and  $\Phi$  grows. In the limit for *very* short  $f$ , all of the O-atoms present in the active volume will be ionized and the signal intensity will be proportional to the  $V_L^{act}$ . Since the active volume decreases with the beam waist, an excessively tight focusing of the laser reduces the signal intensity. On the other hand, mildly focusing lenses allow wider beam waists but smaller  $\Phi$ . In the limit for *very* long  $f$ , the amount of O-atoms available for the ionization grows, but the probability of resonant excitation processes drops, because of their multi-photon nature. Again, the signal intensity drops. An optimal value for the focal length of the focusing lens should be determined, which represents the best compromise between these two diverging requisites.

Using a high vacuum chamber (base pressure of  $5 \cdot 10^{-5}$  mbar) Krenzen investigated the effect of  $f$  on the intensity of the (2+1)REMPI signal for O-atoms produced upon  $\text{NO}_2$  photodissociation. An optimal value of  $f=588$ mm was determined [Krenzen, 1999]. For the actual UHV experiment, to avoid damages to the deflecting prisms, an  $f=250$ mm lens was adopted. Unfortunately, this is expected to reduce the signal intensity to about 1/10 of its optimal value. Here it should be stressed, that a better compromise between prisms safety and signal intensity might be possible. The topic is worth of further investigation, since even a moderate increase in the  $f$  length could lead to a significant increase in the signal intensity.

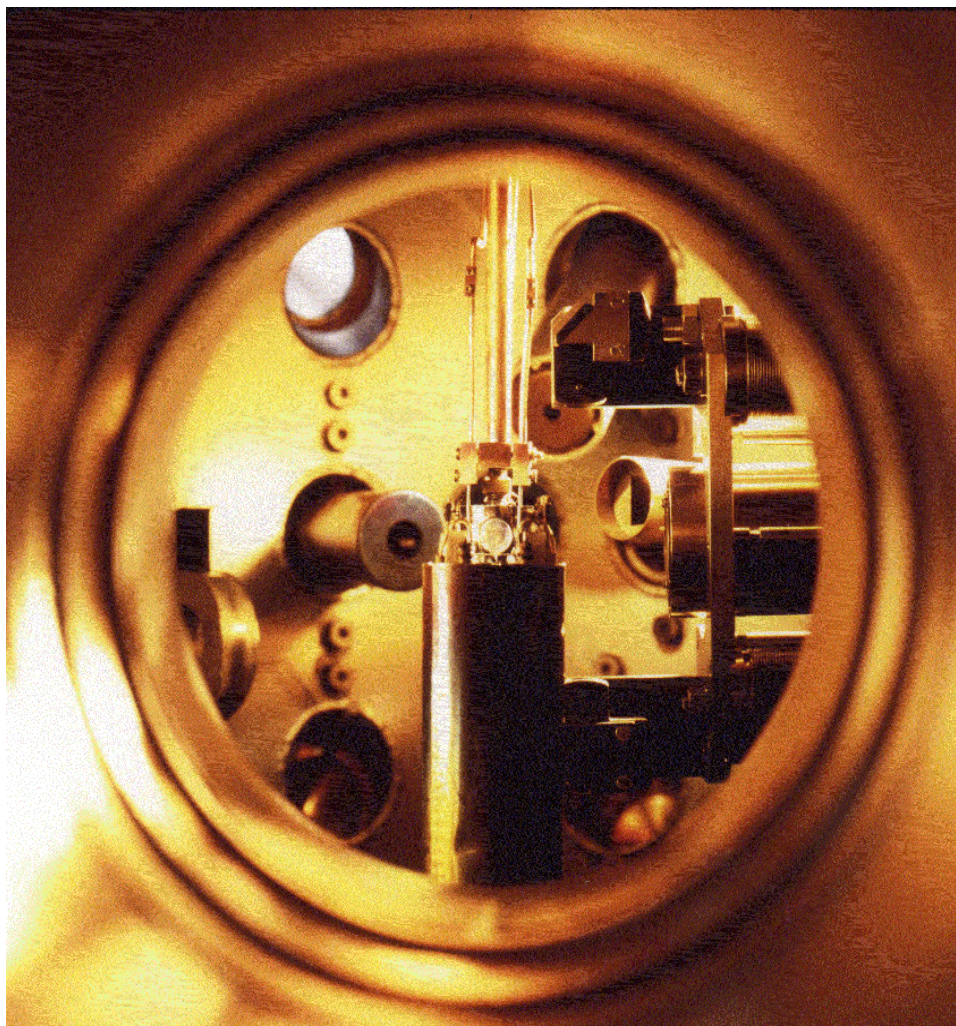
A Quadrupole Mass Spectrometer (Balzers QMS 311) is mounted on a rotatable plate, located inside the UHV chamber. Its ionization volume has a diameter of approximately 5mm and is positioned at the same height as the molecular beam. The QMS can be moved on arcs of circumferences of variable radii centered on the sample position. The molecular beam can be crossed in two points, diametrically located with respect to the sample. In these experiments, the radius of this circumference was 55mm.

Fig. 2.5 offers a partial view inside the UHV chamber: the sample holder (from the top) holds the sample in the middle of the chamber; the QMS is visible as a cylinder underneath the sample; its ionization chamber is behind the sample; the two prisms and the entrance of the drift-tube of the REMPI-ToF spectrometer are visible on the right side of the picture.

## 2.2 THE MOLECULAR BEAM

For the analysis and interpretation of the experimental results, presented in the chapter 4 and 5 respectively, it is important to know the characteristics of the molecular beam. Therefore, they will be shortly described in the remainder of this section.

The three-stages, differentially-pumped supersonic Molecular Beam has already been described in detail elsewhere [Budde, 1988]. Each of the three stages is pumped by a diffusion pump (pumping speed of 1200l/s). A cold trap is inserted between each pump and the chamber, to prevent backstreaming of the pump oil into the molecular beam chamber. This also reduces the pumping speed to 520l/s. The beam source, a pulsed valve (General Valve, Type-9,  $\text{\O} = 275 \mu\text{m}$ ) is located in the first stage of the apparatus, at a working pressure of  $10^{-3}$  mbar. It was backed with  $\text{O}_2$  (Messer-Griesheim 5.5) at an absolute pressure of 3 bar and operated at 10 Hz. Gas pulses of ca. 1 ms duration were produced. After the supersonic expansion, a skimmer ( $\text{\O} = 0.93$  mm) cutted a portion of the gas pulse and allowed it into the second stage ( $P = 10^{-6}$  mbar). Here a mechanical shut-



*Fig. 2.5: A partial view inside the UHV chamber: in the middle, the aluminum sample held by the sample holder; the QMS appears as a cylinder underneath the sample; the ionization chamber is located behind the sample; on the right side the deflection prisms and the entrance of the ToF-tube are visible.*

ter (Uniblitz LS-6), also operated at 10Hz, reduced the pulse length to approx. 400 $\mu$ s. After crossing another skimmer ( $\varnothing=1.7$ mm), the gas pulses reached the third stage ( $P=10^{-7}$ mbar) where a home-built Fizeau-type chopper, rotating at 160Hz, further reduced the pulse duration to approximately 160 $\mu$ s. A set of circular holes, of varying diameters, is machined into a movable screen. By means of this set of diaphragms the gas pulses can be shaped prior to their admission into the UHV chamber. The diaphragms are located in front of the valve, that connects the molecular beam to the UHV chamber. Two different settings were used throughout this experiment. Initially, the pulses were shaped by a 3mm diaphragm, later a 2mm diaphragm was adopted. The measured peak flux was  $2.5 \cdot 10^{10}$  mol $\cdot$ cm $^{-2}$  $\cdot$ pulse $^{-1}$ . The measured divergency of the beam is 0.17°. The molecular beam formed an angle of 45° with the normal to the sample surface.

For the present experiments, pulsed beams showed the advantage of a reduced duty cycle compared to continuous ones. This prolongs the time needed for the complete oxidation of the surface, allowing longer times for the acquisition of laser-ionization spectra. The main drawback connected to the use of pulsed valves as sources for molecular beams is, that they cannot be heated to noticeably increase the translational energy ( $E_{\text{trans}}$ ) of the expanding gas. To circumvent this problem, a short ceramic capillary ( $\varnothing=1$ mm, length=25mm) wrapped in a Thermocoax coil, was connected to the end of the pulsed valve. Circulating a DC current through the coil, the capillary could be heated up to 500K. The gas was heated while expanding through the capillary, and an increase in  $E_{\text{trans}}$  resulted [Weiße, 2000]. A further increase in  $E_{\text{trans}}$  was obtained by seeding O<sub>2</sub> in helium (5.0, Messer-Griesheim).<sup>1</sup> Expanding a mixture of 10% O<sub>2</sub>/He through the heated nozzle, a translational energy of 453meV for the O<sub>2</sub> molecules could be attained. During the whole experiment, the nozzle was either heated to 500K or left at room temperature, conventionally assumed to equal 300K.

REMPI detection of O-atom photofragments from the photodissociation of a NO<sub>2</sub> molecular beam was used to calibrate the detection electronics. The molecular beam was realized by supersonic expansion of a mixture of NO<sub>2</sub> (1.8, Messer-Griesheim) in O<sub>2</sub> or He as carrier gases. The use of a carrier gas was necessary to avoid freezing of NO<sub>2</sub> upon expansion and the consequent clogging of the pulsed valve.

### 2.2.1 The velocity distribution

Molecular beams are known to provide intense, monoenergetic and well-collimated sources of gas molecules (or vapours). These properties are governed by the molecular collision rates. Upon jet expansion, the collision rate drops rapidly and kinetic processes such as the cooling of internal states decrease and, eventually, terminate (“freeze”). Different degrees of freedom require different amounts of collisions to relaxate. Hence, the velocity distribution of the gas after the expansion (terminal velocity) differs considerably from the isotropic equilibrium Boltzmann distribution, which is characterized only

---

1. In a seeded beam, the gas under study (seeding gas) is diluted in an inert, lighter, carrier gas (usually helium). This mixture is fed to the nozzle. Due to their smaller mass, the molecules of the expanding carrier gas acquire a higher velocity than the molecules of the seeding gas. So, the carrier gas “drags” molecules of the seeding gas, increasing the latter’s kinetic energy. The reverse effect (anti-seeding) can be reached diluting the seeding gas in a heavier carrier gas: then the seeding gas is slowed down by collision with the heavier molecules. A serious drawback in this case, is the increase in the beam divergency [Larsen, 1974; Miller, 1988].

by the gas temperature.<sup>1</sup> Other relevant kinetic effects are the rotational and vibrational cooling of the molecules and their possible clustering.

The terminal *mean* velocity of the molecular beam was determined experimentally by means of time-of-flight techniques. The time interval between the opening of the pulsed valve and the maximum of the QMS signal was assumed as the flight time of the gas pulse. The QMS crossed the beam in two diametrically opposite positions, 110mm apart. The flight times were measured with the QMS in the two diametrically opposite location. The measurement of the difference in flight time allowed the measurement of both the terminal *mean* velocity and the translational energy of the beam. In this way,  $E_{\text{trans}}$  could be directly determined within an experimental accuracy of 8%. Parameters characterizing the translational energy distribution of the molecular beam at the seeding and heating conditions used within the experiment, are listed in Table 2.1.

During the adiabatic expansion, which leads to the formation of a supersonic molecular beam, the enthalpy of the gas is transformed into translational energy, according to the following equation

$$E_{\text{trans}} = C_p T_{\text{gas}}, \quad (2.5)$$

where  $C_p$  is the heat capacity of the gas at constant pressure and  $T_{\text{gas}}$  is the equilibrium temperature of the gas before the expansion, i.e. the temperature of the gas reservoir. From this equation, it is also possible to calculate the temperature of the gas before the expansion took place, once  $E_{\text{trans}}$  is given. This allows to measure the temperature reached by the gas, during its expansion through the capillary held at 500K. The values for  $T_{\text{gas}}$  listed in Table 2.1 are referred to the expansion of the gas through the capillary either at room temperature (300K) or heated to 500K. In the second instance, the difference between  $T_{\text{gas}}$  and the nozzle temperature arises from the incomplete thermalization

**Table 2.1: Molecular beam characteristics**

$T_{\text{gas}}$ [K]	Seeding [O <sub>2</sub> % in He]	O <sub>2</sub> velocity [m/s]	Terminal speed ratio	$E_{\text{trans}}$ [meV]	$E_{\text{trans}}$ spread [%]
300	100	736.7	29.5	90	4.5
462	100	902.3	22.0	135	6.1
300	20	1061.9	58.2	187	2.3
462	35	1133.3	49.3	213	2.7
300	10	1190.4	61.8	235	2.2
462	20	1373.9	55.6	313	2.4
462	10	1617.8	59.8	434	2.2

1. A thorough discussion of the continuum properties of the free jet expansion, as opposed to the one arising from nonequilibrium kinetic effects, can be found in the article by Miller [Miller, 1988].

of the gas with the capillary during the expansion process.  $T_{\text{gas}}$  (500 K) was obtained from  $E_{\text{trans}}$  measured for a beam of pure  $\text{O}_2$ , expanding through the capillary held at 500 K.

To determine the energy resolution of the beam, it is necessary to calculate its *final temperature* (velocity spread). First of all, a molecular beam can be characterized through its speed ratio ( $S$ ), that is the mean velocity divided by the thermal spread in velocities, as defined in the following equation

$$S = \frac{v}{\sqrt{\frac{2kT}{m}}} . \quad (2.6)$$

The molecules can be thought of as diffusing in the space from a point-like source. Therefore, the spread has to be divided into two components. The first one is perpendicular to the direction of motion and, in absence of collisions, represents the geometric cooling due to the spherical expansion of the gas. Actually, the amount of thermal perpendicular energy does not fall as  $1/r^2$  because parallel collisions constantly scatter molecules into the perpendicular directions, contributing to the tails of the perpendicular velocity distribution function. The second component is parallel to the direction of motion and will ultimately determine the energy resolution of the molecular beam, at the point of impact with the target. The velocity distribution parallel to the direction of propagation closely resembles a gaussian [Beijerinck, 1979].

For the terminal parallel speed ratio (*i.e.* the parallel speed ratio calculated far away from the nozzle, where no more collisions take place), the following formula can be used

$$S_{//,\infty} = A \left[ \sqrt{2} n_0 d \left( \frac{53C_6}{kT_0} \right)^{\frac{1}{3}} \right]^B \quad (2.7)$$

where  $n_0$  is the source density,  $d$  is the source diameter,  $k$  is the Boltzmann constant and  $T_0$  is the source absolute temperature [Beijerinck, 1983]. The values for the constants  $A$  and  $B$  are given in Table 2.2. The cross-section  $(53C_6/kT_0)^{\frac{1}{3}}$  is calculated assuming an intermolecular attractive potential  $C_6/r^6$ , which is adequate for the low temperatures reached upon expansion. It can be replaced by the hard sphere cross-section,  $\pi\sigma^2$ , if the expansion starts from a heated source. For the gases used in this study, namely  $\text{O}_2$  and He, the respective values of  $C_6/k$  are 8.31 and 0.154 in units of  $10^{-43} \text{K}\cdot\text{cm}^6$ , while  $\sigma(\text{He})=2.66 \text{ \AA}$  and  $\sigma(\text{O}_2)=3.49 \text{ \AA}$ . The terminal speed ratios ( $S_{//,\infty}$ ) calculated according to Eq. 2.7 are listed in Table 2.1. The corresponding values for seeded beams are obtained by mass weighted interpolation of the  $S_{//,\infty}$  values calculated for the pure gases.

**Table 2.2: Terminal speed ratio correlation, Eq. 2.7**

$\gamma$	$A$	$B$
5/3	0.778	0.495
7/5	0.783	0.353

### 2.2.2 Rotational vs. vibrational cooling

The total number of binary collisions experienced by a molecule during free jet expansions is typically of the order  $10^2$  to  $10^3$ . Therefore, any kinetic process requiring this number of binary collisions to approach equilibrium will be subject to kinetic lags or relaxation effects during the expansion. Processes requiring a higher number of collisions to reach the equilibrium will not relaxate during the expansion. As an example, the vibrational relaxation of simple diatomic molecules may require more than  $10^4$  collisions [Miller, 1988]. Therefore, the vibrational degree of freedom will freeze during the expansion before noticeable thermalization takes place. On the other hand, the number of collisions needed to thermalize the rotational degree of freedom of most of the diatomic molecules (also called *rotational number* or  $Z_R$ ) is of the order of 10 or 100. Hence, these modes may exchange energy and cool down during the initial part of the expansion before freezing. The values of  $Z_R$  for  $O_2$  is 2. Therefore, the rotational temperature of a diatomic gas after supersonic expansion is usually very low. On the contrary, the effect of the expansion process on the vibrational temperature of the same gas is practically negligible.

It is possible to estimate the rotational temperature of the molecular beam at different working conditions, using Poulsen's dimensionless collision parameter  $B$  [Poulsen, 1977]

$$B = \left( \frac{\pi\sigma^2}{Z_R} \right) \cdot \left( \frac{4}{\sqrt{\pi}} \right) \cdot n_0 d \quad (2.7)$$

and the graph in Fig. 2.6 [Miller, 1988]. This approach is rigorously valid only if the gas expansion is isentropic. The  $B$ -values for seeded beams are calculated by mass weighted

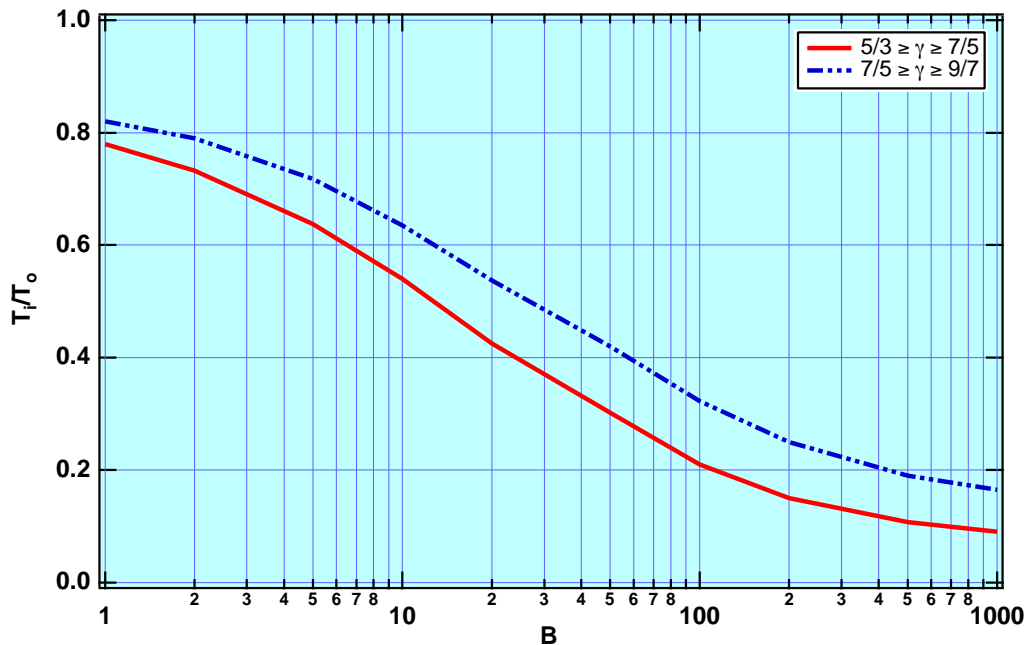


Fig. 2.6: Terminal internal temperature ( $T_i/T_0$ ) vs. dimensionless collision parameter ( $B$ ) from a rigorous non-equilibrium calculation.  $5/3 \geq \gamma \geq 7/5$ : rotational relaxation of a linear molecule (equilibrium:  $\gamma=7/5$ ; frozen:  $\gamma=5/3$ ).  $7/5 \geq \gamma \geq 9/7$ : relaxation of one vibrational mode (equilibrium:  $\gamma=9/7$ ; frozen:  $\gamma=7/5$ ) [Miller, 1988].

interpolation of the values obtained for the pure gases. The results are shown in Table 2.3 (the translational temperature of the beam is given as a reference).

At the given seeding conditions,  $T_{\text{rot}}$  appears to be independent from the actual composition of the beam. This is a quite surprising result, because a seeded beam should be rotationally hotter than a pure one. In fact, rotational cooling results from the redistribution of the rotational energy among the expanding molecules. This dynamical process takes place by means of the collisions of “hotter” molecules with “colder” ones. It proceeds until the density of particles is so low, that the amount of collisions is negligible (*i.e.*: until the degree of freedom is frozen). From classical mechanics it is known, that the energy transfer rate upon collisions is highest when the colliding particles have comparable masses. When the masses are different, this process still takes place, albeit at a lower rate. In the case of an expanding gas mixture, the presence of a lighter carrier gas should reduce the efficiency of rotational cooling, especially at high dilution. This effect is tendentially shown by the slight increase in the calculated value of  $T_{\text{rot}}$  for the heated beam, when the amount of  $\text{O}_2$  is reduced from 20% to 10%. However, at higher  $\text{O}_2$  concentration and lower  $T_{\text{nozzle}}$ , this effect is not reproduced by this model.

The model described above relies on the assumption that the expansion is isentropic. This may not be completely true in the present case, since the gas expansion takes place initially through a thin and long capillary, where the flow is probably in the viscous regime. To check the validity of the previously exposed model, the rotational temperature of the beam as a function of seeding and heating conditions has been experimentally determined by means of REMPI spectroscopy. (2+1)-REMPI spectroscopy of  $\text{O}_2$  in the wavelength range between 276nm and 306nm is possible. However, because of the competition between ionization and predissociation of the excited state, the determination of the rotational temperature is not facile [Sur, 1991]. On the contrary, the measurement and interpretation of REMPI spectra for NO is comparatively much simpler. Since both the masses and the inertia momenta of NO and  $\text{O}_2$  differ by only 6.5%, it is reasonable to think, that the supersonic expansion process for the two gases should be quite similar. On these premises, the molecular beam has been characterized studying the supersonic expansion of NO by means of (1+1)-REMPI, through the reaction

**Table 2.3: Rotational cooling and clustering**

$T_{\text{Nozzle}}$ [K]	Seeding [ $\text{O}_2$ % in He]	$T_{\text{trans}}$ [K]	$T_{\text{rot}}$ [K]	$D^*$ [ $\cdot 10^{-5}$ ]	$C^*$ [ $\cdot 10^{-2}$ ]
300	100	1.2	22.9	14.3	17.7
500	100	3.2	35.3	5.1	6.6
300	20	0.6	22.9	3.1	3.9
500	35	1.0	35.3	1.8	2.4
300	10	0.7	22.9	1.7	2.2
500	20	1.2	35.3	1.1	1.5
500	10	1.4	35.4	0.6	0.8



and



in the 226nm region [Laß, 2001]. The experimentally determined rotational temperatures are reported in Table 2.4 together with the calculated ones. The comparison of the two sets of values for  $T_{rot}$  shows, that the model underestimates the rotational temperature of the gas upon expansion. The reason is the non-ideality of the expansion process through the capillary where the isentropic approximation is no longer valid. In the remainder of the present work, the experimental values for  $T_{rot}$  will be used.

The effect of the increased nozzle temperature (500 K) on the population of the higher vibrational states is found to be negligible: the total decrease in the population of the vibrational ground state was less than 0.7%. The effect of the vibrational degree of freedom on the dissociative chemisorption of  $O_2$  on Al could not be investigated with this experimental setup.

### 2.2.3 Clustering

It is known, that the free-jet expansion provides a suitable flow field to study clustering and condensation kinetics. In our case, this would be an undesired side effect since relevant clustering increases the spread of the parallel velocity (i.e.: “heats up” the gas) and reduces the terminal velocity attainable by the beam. Hereafter, I will restrict to borrowing the most useful experimental rules, which allow us to safely neglect these processes. For a thorough analysis of this topic, the reader is referred to the already cited publication by R.D. Miller and references therein [Miller, 1988].

Following the scaling laws proposed by Hagena [Hagena, 1981], Beijerinck and Verster proposed a dimensionless parameters ( $C^*$ ) to characterize the formation of trimers and larger cluster in the expanding gas. For monoatomic gases, they proposed a safe upper limit of

$$C^* \equiv \frac{P_0}{\left(\frac{\varepsilon}{\sigma^3}\right)} \left(\frac{d}{\sigma}\right)^{0.88} \left(\frac{T_0}{\varepsilon/k}\right)^{-2.3} < 15. \quad (2.8)$$

**Table 2.4: Experimental values of the rotational temperature for NO upon supersonic expansion, under different heating and seeding conditions**

$T_{Nozzle}$ [K]	Seeding [O <sub>2</sub> % in He]	$T_{rot}^{exp}$ [K]	$T_{rot}$ [K]
300	100	36±4	22.9
300	10	54±6	22.9
500	100	75±6	35.3
500	10	154±7	35.4

This limit should be higher for biatomic gases [Beijerinck, 1981]. At the present experimental conditions, the values of this parameter are three orders of magnitude smaller than the limit in Eq. 2.8. Therefore, I am confident that trimerization is negligible.

According to Knuth's analysis of dimer-formation rate coefficients in free-jet expansions, dimer formation exceeding 1% in monoatomic gases can be avoided if the parameter  $D^*$  does not exceed 0.1 [Knuth, 1977]:

$$D^* \equiv \frac{P_0}{\left(\frac{\varepsilon}{\sigma^3}\right)} \left(\frac{d}{\sigma}\right)^{0.4} \left(\frac{T_0}{\varepsilon/k}\right)^{-2.4} < 0.1. \quad (2.9)$$

The calculated values for  $D^*$  and  $C^*$  are listed in Table 2.3. In the case of seeded beams, the parameter values were calculated as mass weighted interpolation of the values obtained for the pure gases.

Since the values of  $D^*$  calculated for our experimental condition are four orders of magnitude smaller than the limit in Eq. 2.9, dimer formation during the expansion can also be safely excluded.

### 2.3 THE LASER

A pump-dye laser system was used as laser source for O-atom spectrometry. The pump laser, a Q-switched Nd:YAG laser from Spectra Physics (GCR 190), operates at 10Hz repetition rate and emits pulses lasting approximately 10ns at 1064nm. Its second harmonic (355nm) was used to pump a dye laser (Sirah Precision Scan-G), in which a solution of Coumarin 47 (1:1 with Diazabicyclooctane in Propylene Carbonate) was circulated. The dye laser produced light pulses in the wavelength range between 451.2nm and 452.6nm, shorter than 10ns. It has a nominal linewidth ( $\Delta\lambda$ ) of 0.002nm at the wavelength range in use, corresponding to a bandwidth ( $\Delta\nu$ ) of  $0.1\text{cm}^{-1}$ . These pulses were frequency doubled in a  $\beta$ -BBO crystal (Radiant Dyes). The conversion efficiency of a Second Harmonic Generator (SHG) crystal depends strongly on the angle between the incoming laser beam and the optical axis of the crystal. Its alignment was preliminarily calibrated, monitoring the intensity of the SH emission with a pyroelectric detector (Sirah). The final adjustment was performed monitoring the intensity of the REMPI signal due to O-atoms generated upon  $\text{NO}_2$  photodissociation, as described in Section 3.2. The SH light was separated from the fundamental by means of a self-compensating set of four Pellin-Broca prisms (Sirah). Alternatively, to minimize transmission losses of the SH light, the four prisms were replaced by a  $45^\circ$  dielectric mirror with its maximum reflectivity centered at 226nm (Laser Components). One  $90^\circ$  prism steered the SH light pulses into the HV chamber. A set of three  $90^\circ$  prisms was needed to steer the frequency doubled light pulses into the UHV chambers. All of these prisms were made of UV grade fused silica (Melles Griot).

The intensity of the frequency doubled pulses, measured with a pyroelectric detector before and after each experimental run, was stable on the average. Deviation up to  $\pm 10\%$  for the intensity of two successive pulses were measured. An optimal average intensity of 3mJ/pulse was possible, but the experiments were routinely performed at a lower intensity (2.5mJ/pulse) to increase the dye lifetime.

Reflections at the prisms and absorption in air induced an attenuation of 43% between the laser intensity measured at the laser output port and the one measured at the entrance of the UHV system. In the following, the given laser intensities are always corrected for such losses.

#### 2.4 THE HIGH VACUUM CHAMBER (HV)

The HV chamber used for the  $\text{NO}_2$  photodissociation study is sketched in Fig. 2.7. It was already described in detail elsewhere [de Meijere, 1995]. It consists of a spherical body with two diametrically opposed Brewster windows. A ToF mass spectrometer, similar to the one in the UHV chamber, is located in the spherical body. Its axis is perpendicular to the optical path of the laser beam. The entrance of the ToF tube is located approximately 1 cm above the laser beam path.

The HV chamber was pumped to a base pressure of  $2 \cdot 10^{-5}$  mbar by means of a diffusion pump (Leybold), backed by a rotary pump (Leybold, Trivac D10).  $\text{NO}_2$  (1.8, Messer-Griesheim) was admitted to the chamber through a stainless steel needle valve (Whitey), up to a pressure of  $10^{-4}$  mbar. The two Brewster windows allowed the laser beam in and out of the chamber, to avoid the noise generated by stray photons. A 250 mm lens focused the laser light in the centre of the chamber, underneath the ToF detector. At the laser focus,  $\text{NO}_2$  was photodissociated and multi-photon ionization of its fragments took place [Section 3.2]. The ionized photofragments were accelerated by an extraction field, mass-separated in the field-free region of the ToF spectrometer [Section 2.1] and detected by a chevron stack of MCPs, with a  $\Delta V$  of -1700 V across them.

Fig. 2.8 show a REMPI-ToF spectrum for  $\text{NO}_2$  photodissociation. The photoionization signal detected at the MCPs shows two clearly distinguishable major peaks, each

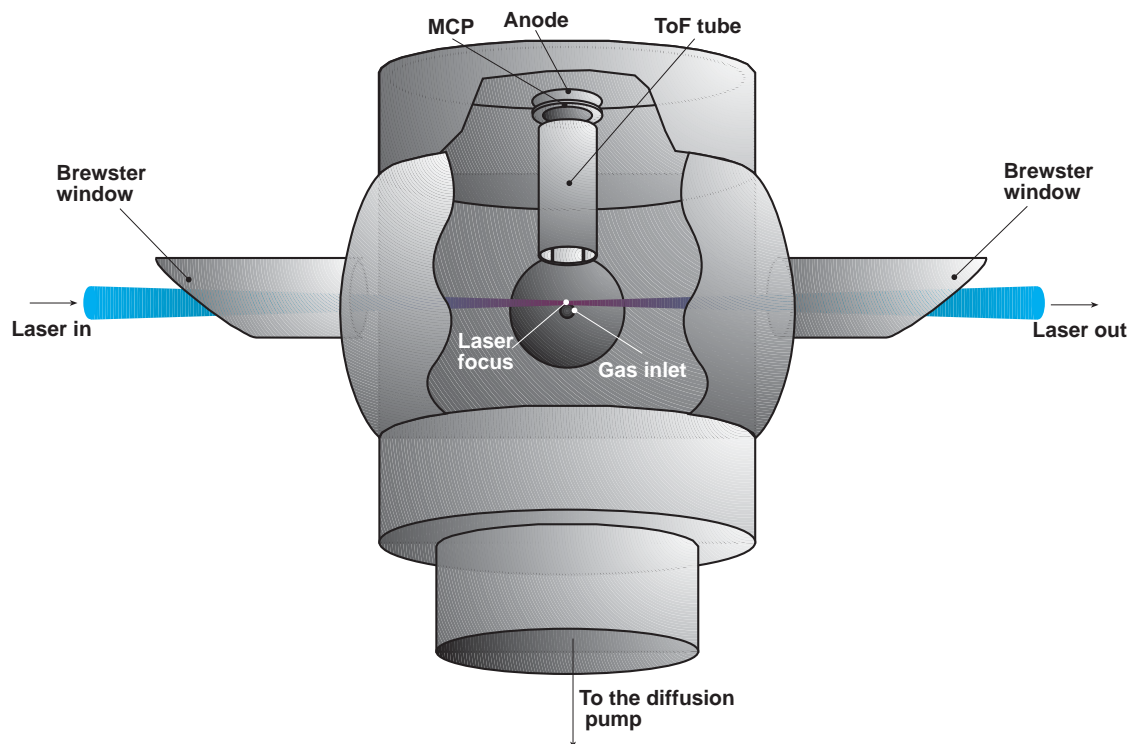


Fig. 2.7: Scheme of the HV chamber.

one with a FWHM of ca. 400ns. Scanning the frequencies of the laser light, variations in the intensity of the two peaks allowed a provisional distinction between atomic (O) and molecular (NO) species. The attribution of the peaks was confirmed by the analysis of the flight times of the two species. The origin of the time scale for the ToF spectra was provided by a Transistor-Transistor-Logic (TTL) pulse generated by the circuitry driving the Q-switch of the pump laser. The TTL pulse is simultaneous with the pump laser pulse. The collected signals were proportional to the density of the respective ionic species. These two peaks were  $1.35\mu\text{s}$  apart from each other. The ratio of the flight times, 0.733, is in excellent agreement with the expected value of 0.730 calculated for  $\text{O}^+$  and  $\text{NO}^+$  according to Eq. 2.1.

## 2.5 ELECTRONICS FOR SYNCHRONIZATION AND DATA ACQUISITION

The experiments presented in this work are characterized by the use of a pulsed  $\text{O}_2$  source (molecular beam) and a pulsed detector (REMPI-ToF mass spectrometer). To perform these measurements, it was necessary to carefully synchronize the pulsed molecular beam with the laser and the acquisition electronics. Frequency instabilities affecting mechanical devices are usually higher than the ones characterizing electronic devices. To avoid the problems due to the wandering of the chopper frequency, the whole experiment was synchronized with the chopper itself. An analog signal, synchronous with its rotating disk, was shaped into a TTL one by means of a home built Schmitt's trigger, its frequency was reduced to 10Hz and it was fed into the input of a Delay-Unit/Pulse-Generator (Stanford Research Systems, SRS DG535). This unit generated the signals that triggered the remaining electrical and mechanical components, as shown in Fig. 2.9 A.

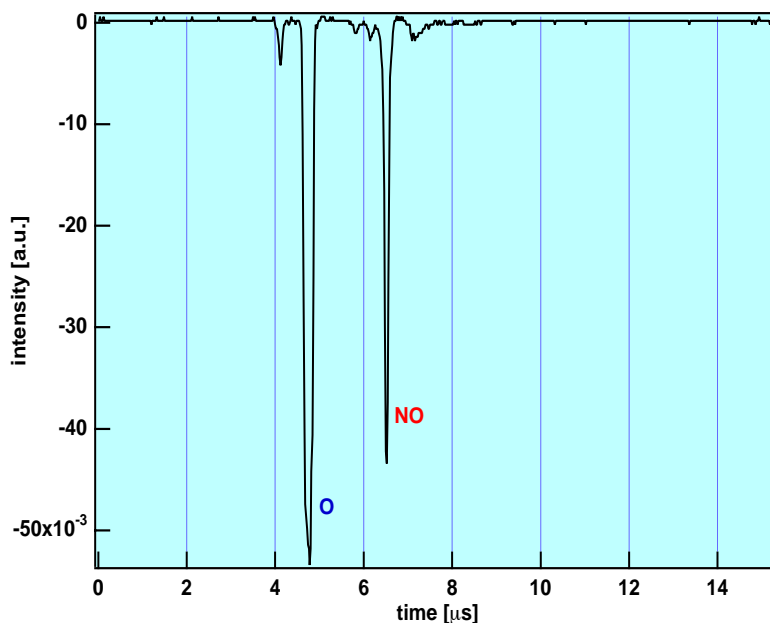


Fig. 2.8: REMPI-ToF spectrum of  $\text{NO}_2$  fragments, upon photodissociation in the HV chamber. Experimental conditions:  $\text{NO}_2$  partial pressure =  $8 \cdot 10^{-5}$  mbar; laser intensity =  $0.9 \text{ mJ/pulse}$ ; extraction potential =  $-160 \text{ V}$ ;  $\Delta V$  across the MCPs =  $-1700 \text{ V}$ .

### 2.5.1 Data acquisition chain for the oxidation experiment (in UHV)

A chevron stack of MCPs, with a  $\Delta V$  of  $-2000\text{ V}$  across them, is a high gain ( $10^7\div 10^8$ ) fast charge amplifier. An ion hitting the MCP produces a negative current pulse, approximately  $10\text{ ns}$  long, which originates a voltage pulse of some  $\text{mV}$ 's when terminated on a  $50\ \Omega$  resistive load, like the low impedance entrance channel of an oscilloscope (Tektronix 2432A, bandwidth= $300\text{ MHz}$ , sampling rate= $250\text{ MS/s}$ ). Under the given experimental conditions, less than 1 ion per laser and gas pulse was detected. Each of them was singly acquired. A preliminar study on the yield and time-of-flight distributions of abstracted oxygen atoms was accomplished feeding the MCPs output directly into a scaler (Stanford Research Systems, SR 430 Multi-Channel Scaler), as illustrated in Fig. 2.9A. The temporal evolution of the O-atom yield as function of the  $\text{O}_2$  dose was recorded using the detection chain displayed in the scheme in Fig. 2.9 B. In this case, the

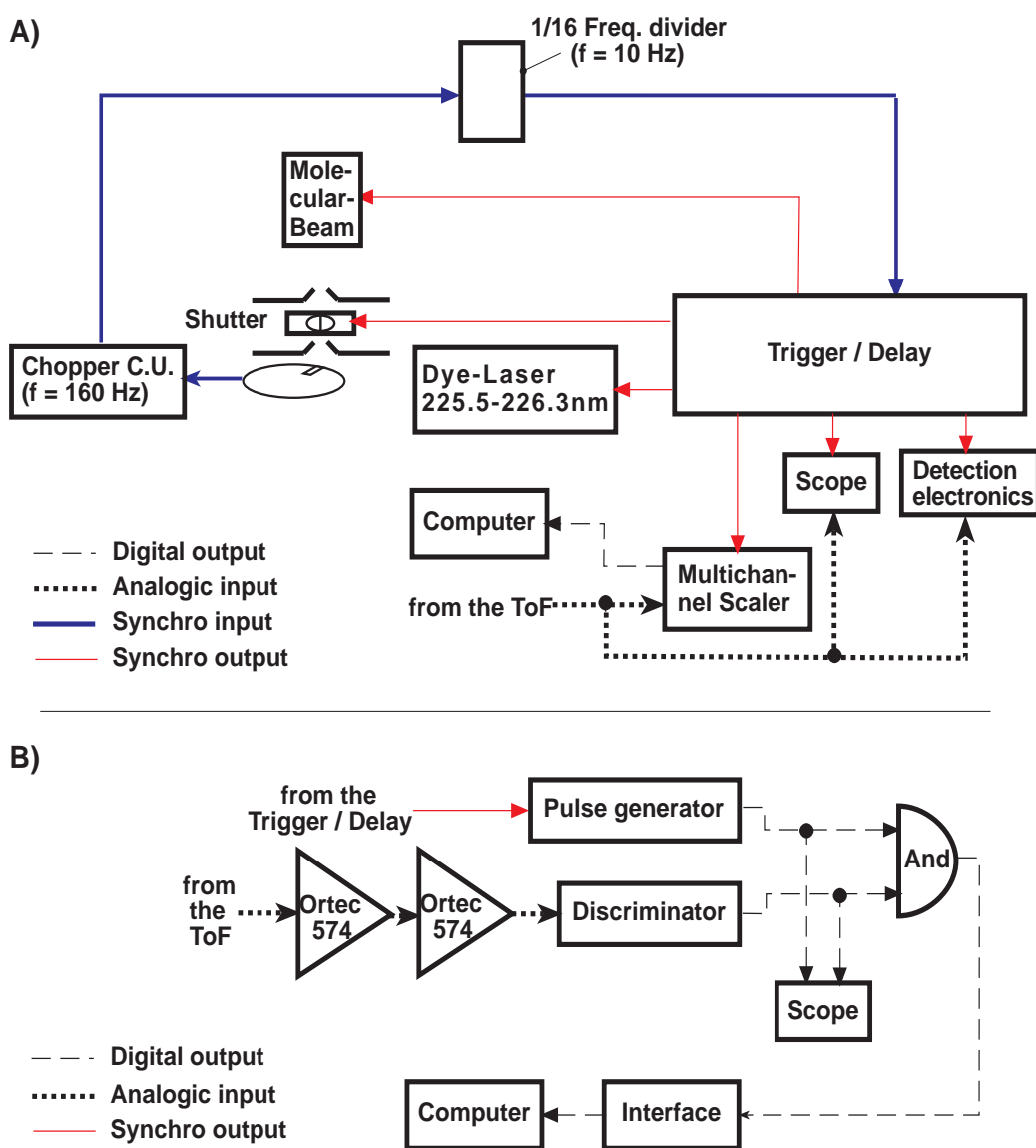


Fig. 2.9: A) Scheme of the synchronization circuit and the electronics for the detection of O-atoms ToF spectra. See text for details. B) Alternative electronics for O-atoms detection. See text for details.

MCPs output was amplified twice (Ortec, 574 Timing Amplifier) and then fed into a 100MHz discriminator (Ortec, 436 Discriminator). Its positive output, a 5V high and 500ns wide pulse, was set in coincidence with an acquisition window of 1.2 $\mu$ sec produced with a pulse generator (Philips, PM 5705). The output of the coincidence unit was sent to the digital input of a computer interface (Stanford Research Systems, SRS 245) and finally acquired by a computer (Power Mac 7100/66 AV) using a home-made program based on commercial software (National Instruments, LabVIEW 4). As a reference, the output of this detection chain was displayed on a two-trace digital oscilloscope (Tektronix 2432A).

The diagram in Fig. 2.10 shows an overview of the triggering signals used during the experiment performed in the UHV chamber. The delays are to scale. The lengths of the pulses represent the durations of the associated event, with the exception of the laser pulse (10ns), which would otherwise be too short to appear in this picture. The rotating disk of the chopper crosses the optical path between a light emitting diode (LED) and a photodiode. When the light from the LED crosses a thin slit on the disk, it can reach the photodiode and the  $t_0$  signal is produced. Two identical slits, 5mm wide, are machined symmetrically in the outer region of the chopper disk. The molecular beam can cross the chopper only in coincidence with one of these two slits. Appropriately dephasing the shutter and the pulsed valve with respect to the chopper, one single gas pulse was selected and admitted to the UHV chamber.

### 2.5.2 Data acquisition chain for the laser calibration experiment (in HV)

The fine tuning of the laser wavelength was performed monitoring the intensity of the REMPI signal due to O-atoms generated upon NO<sub>2</sub> photodissociation in the HV chamber. The detailed procedure is described in Section 3.2. Hereafter, only a brief comment on the detection of the REMPI signal is given. The ions generated upon NO<sub>2</sub> photodisso-

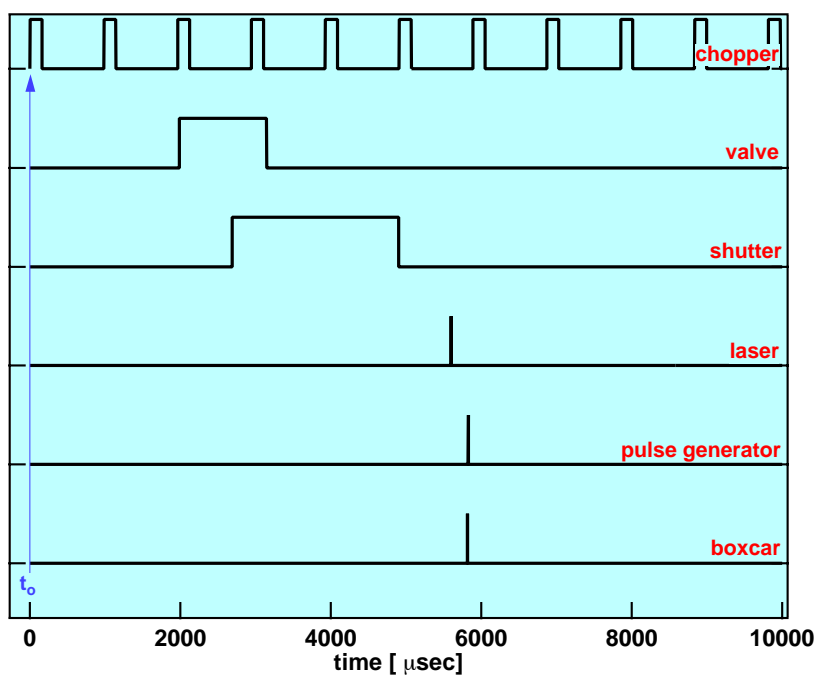


Fig. 2.10: Synoptical diagram of the delay time adopted in the experiment.

ciation were detected by means of two boxcar integrators and averagers (Stanford Research Systems, SRS 250). These were synchronized with the laser by means of the SRS DG535 unit. Their acquisition windows were set at a different delay time with respect to the laser pulse to monitor simultaneously the signals relative to the production of O and NO. Their output signals were collected with the computer interface (SRS 245) and finally acquired by the computer, that was driven by a home-made application based on LabVIEW 4. At the same time, as a reference, the output of the ToF spectrometer was displayed on the two-trace digital oscilloscope (Tektronix 2432A) together with one of the boxcar acquisition windows. The oscilloscope was triggered on the boxcar signal.

### 3. REMPI OF OXYGEN ATOMS

*Resonantly Enhanced Multi-Photon Ionization* (REMPI) spectroscopy is an established experimental technique since two decades. It is well-suited for the detection of neutrals (both molecules and atoms) in the gas phase and its main advantage lies in the quantum state selectivity coupled with a high sensitivity. Coupling REMPI spectroscopy with *Time-of-flight* techniques (REMPI-ToF), it is possible to separate the incoming ions according to their masses and energies. Gating the detector output, it is possible to select the ions according to their  $q/m$  ratio. This allows to efficiently reduce the background due to non-resonantly ionized atoms or molecules, and to enhance the element or isotope selectivity for the process investigated. Sensitivities of  $10^6 \text{ mol}\cdot\text{cm}^{-3}$  and quantum state are reported, corresponding to a partial pressure of  $10^{-10}$  mbar particles in a given quantum state [Zimmermann, 1995].

In a  $(n+1)$ -REMPI process, the *simultaneous* absorption of  $n$  photons causes the transition of a system from a specific rovibronic state (the ground state, of energy  $E''$ ) to a specific electronically excited rovibronic state (intermediate state, of energy  $E'$ ). Following a time honored tradition in spectroscopy, the quantum numbers of the ground state are indicated with the double prime ( $J''$ ), while the ones referring to the excited state are indicated with the single prime ( $J'$ ). The  $n$ -photons absorption is a *resonant* process: its cross-section  $\sigma_{J''}^{(2)}$  (the integrated absorption coefficient) is only significative when the energy difference between ground and intermediate state is exactly  $n$ -times the energy of the incoming photon:

$$n \cdot h\nu = E' - E'' . \quad (3.1)$$

The absorption of another photon causes the ionization of that system. The photoionization step too can be characterized through its cross-section ( $\sigma_{pi}$ ).

There are pros and cons connected to each experimental technique, and alternative approaches to this experiment (e.g.: Laser Induced Fluorescence, Single Photon Ionization or Quadrupole Mass Spectrometry) might be considered. Nevertheless, REMPI was chosen due to the following considerations:

The detection of photons is inherently less efficient than the detection of ions; moreover, the stray light from the excitation source might reduce the *signal-to-noise* ratio of the measurements or even saturate the detector.

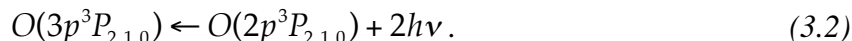
Multi-photon processes have smaller cross-sections than their single-photon counterparts. On the other hand, it is easier to obtain higher fluences for the less energetic photons involved in multi-photon processes than for the high energy photons necessary for single-photon processes ( $>10\text{eV}$ ). The trade-off between these two factors favors the multi-photon processes.

Atoms or molecules in the ground state are usually characterized by broad velocity distributions. This originates the Doppler broadening of the relative spectral lines. The intermediate state resonantly populated during REMPI is narrower than the ground state. As a result, linewidths of resonantly enhanced transitions are narrower than their non-resonant counterparts. This allows a better resolution of the translational energies of the ionized species.

In a process involving  $n$  photons, the intensity of the signal depends on the  $n^{\text{th}}$ -power of the laser intensity. Studying the intensity of the ionization signal as a function of the laser fluence, it is possible to identify parallel reaction channels leading to the same ionized products [Section 3.3].

### 3.1 SPECTROSCOPY OF OXYGEN ATOMS

The electronic states and transitions relevant for the (2+1) spectrometry of oxygen atoms are described in Fig. 3.1. Initially, an atom is in the ground state ( $2p^3P$ ). The simultaneous absorption of two photons brings it to the intermediate state ( $3p^3P$ )



The absorption of the third photon causes the ionization



Both the ground and the intermediate states are triplets. So, scanning the laser wavelength in the range between 225.5 nm and 226.3 nm should lead to nine different lines. Two transitions ( $0 \leftarrow 1, 1 \leftarrow 0 = J' \leftarrow J''$ ) are forbidden. Moreover, given the bandwidth of the laser light attainable within the present experimental setup and the Doppler width  $\Delta\nu_D$  of  $0.3\text{cm}^{-1}$  calculated for the O lines at the given experimental condition, the fine structure of the electronically excited state could not be resolved. In fact, the optimal bandwidth of the dye laser,  $\Delta\nu_F$ , is  $0.1\text{cm}^{-1}$ . In a 2-photon process, the overall bandwidth,  $\Delta\nu_{2\text{ph}}$ , is given by the random superposition of the  $\Delta\nu_{\text{SH}}$  characterising each of the two absorbed photons. The second harmonic photon results from the interaction of two photons at the fundamental laser frequency in the  $\beta$ -BBO crystal. Hence,  $\Delta\nu_{2\text{ph}}$  results from the random superposition of the bandwidths of four photons at the fundamental dye laser wavelength, and can be written as

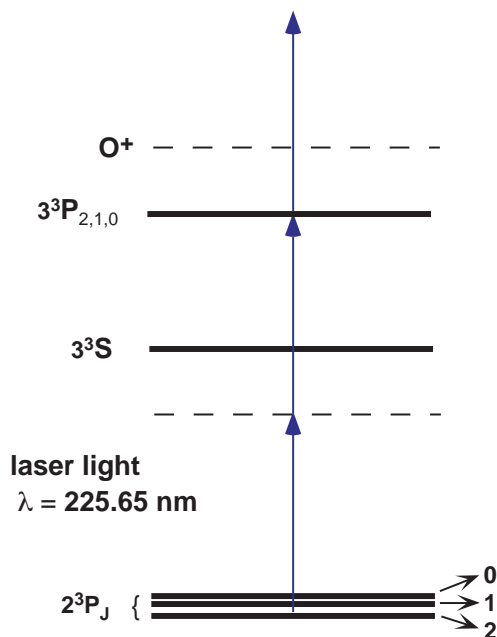


Fig. 3.1: Relevant states for REMPI of oxygen atoms.

$$\Delta\nu_{2ph} = \sqrt{4 \cdot \Delta\nu_f^2} = 2 \cdot \Delta\nu_f. \quad (3.4)$$

Based on this analysis, a value of  $0.2 \text{ cm}^{-1}$  for  $\Delta\nu_{2ph}$  was expected. If the laser bandwidth combines randomly with the intrinsic Doppler width of the O-lines, an overall bandwidth  $\Delta\nu_o$

$$\Delta\nu_o = \sqrt{4 \cdot \Delta\nu_f^2 + \Delta\nu_D^2} \quad (3.5)$$

can be defined, whose value is  $0.36 \text{ cm}^{-1}$  with the given experimental setup. The intrinsic widths of the oxygen lines,  $\Delta\nu_1$ ,  $0.555 \text{ cm}^{-1}$  for the unresolved  $3^3P_{0,1,2} \leftarrow 2^3P_2$  multiplet and  $0.159 \text{ cm}^{-1}$  for the unresolved  $3^3P_J \leftarrow 2^3P_{0,1}$  multiplet, are comparable to  $\Delta\nu_o$  and cannot be resolved [Bamford, 1987]. Assuming a random combination of  $\Delta\nu_o$  with  $\Delta\nu_1$ , the expected value of the experimental linewidths calculated according to the following equation

$$\Delta\nu_{\text{exp}} = \sqrt{\Delta\nu_o^2 + \Delta\nu_D^2}, \quad (3.6)$$

are  $0.66 \text{ cm}^{-1}$  and  $0.39 \text{ cm}^{-1}$  respectively, in agreement with the experimental results displayed in Fig. 3.2.

From the knowledge of the cross-sections for the reactions in Eq. 3.2 and Eq. 3.3, it is possible to determine quantitatively the amount of oxygen atoms present in the laser ionization volume [Bamford, 1986; Bamford, 1987]. Alternatively, if a source of O-atoms was available, it would be possible to calibrate the absolute sensitivity of the REMPI-ToF mass spectrometer measuring the amount of O-ions detected for a given partial pressure of atomic O. In the following sections I will show that  $\text{NO}_2$  photodissociation in the 225 nm range can be used to generate free O-atoms and a calibration of the instrument is possible.

### 3.2 LASER'S WAVELENGTH CALIBRATION

The 2-photon resonant excitation of O-atoms takes place between the ground state ( $2^3P_J$ ) and the metastable state ( $3^3P_J$ ).<sup>1</sup> Since both of these states are long-lived, the transition energies are well defined and the corresponding REMPI lines are narrow.

Based on thermodynamical consideration, the abstracted atoms were expected to be released mainly, if at all, in their ground states. So, a reliable source of oxygen atoms in the  $2p^3P$  multiplet was needed to calibrate the laser's wavelength. In this regard, the UV induced  $\text{NO}_2$  photodissociation reaction



showed two main advantages with respect to other processes:

- a high yield of atomic oxygen in the desired electronic state;
- the simultaneous presence of NO.

Photodissociation of room temperature  $\text{NO}_2$  according to Eq. 3.7 shows a threshold at 394.5 nm. The quantum efficiency of this reaction is 0.97 at wavelengths shorter than 313.0 nm [Calvert, 1966]. At laser wavelengths lower than 244 nm  $\text{O}(^1D)$  production

---

1. The lifetime for the  $3^3P$  state is 34.7 ns [Bamford, 1986]

becomes viable. The efficiency of this second channel grows rapidly with the photon energy. At wavelengths in the 225 nm range, the production quantum efficiency for  $O(^1D)$  and  $O(^3P)$  production are 0.54 and 0.46, respectively [Richter,2000]. As shown in Fig. 3.2,  $NO^+$  ions are generated in the same spectral region where oxygen photoionization takes place. The signal intensity due to O-ions is approximately one tenth of the intensity relative to NO-ions. It is known that (1+1) REMPI in the 226nm range allows to detect NO partial pressures as low as  $10^{-10}$  mbar in a given quantum state [Zimmermann, 1995]. Hence, a detection limit of  $10^{-9}$  mbar for O-atoms in a given quantum state can be inferred from the data displayed in Fig. 3.2. Since the cross-sections for photoionization from their electronically excited states are similar for both species, the differences in signal intensity must be traced back to different efficiencies of the excitation processes.<sup>1</sup> At 226nm, the  $A \leftarrow X$  transition for NO is a single-photon process, while the  $2^3P_J \leftarrow 3^3P_J$  transition for O is a two-photon process. Consequently, the former process is expected to be roughly four orders of magnitude more probable than the latter one. On the other hand, the manifold of quantum states available to NO and O upon  $NO_2$  photodissociation must also be considered to estimate the signal intensity. Upon photodissociation, NO is released in a distribution of vibrationally excited states, while only four quantum states are available to O atoms [Richter,2000]. Therefore, the ratio of the manifold of quantum states available to NO and to O is approximately  $10^4$ . Together with the differences in excitation probabilities, these effects allow to explain the ratio of the measured intensities displayed in Fig. 3.2.

The banded structure of the NO signal can be used as a reference if calibration of the laser's wavelength is needed.

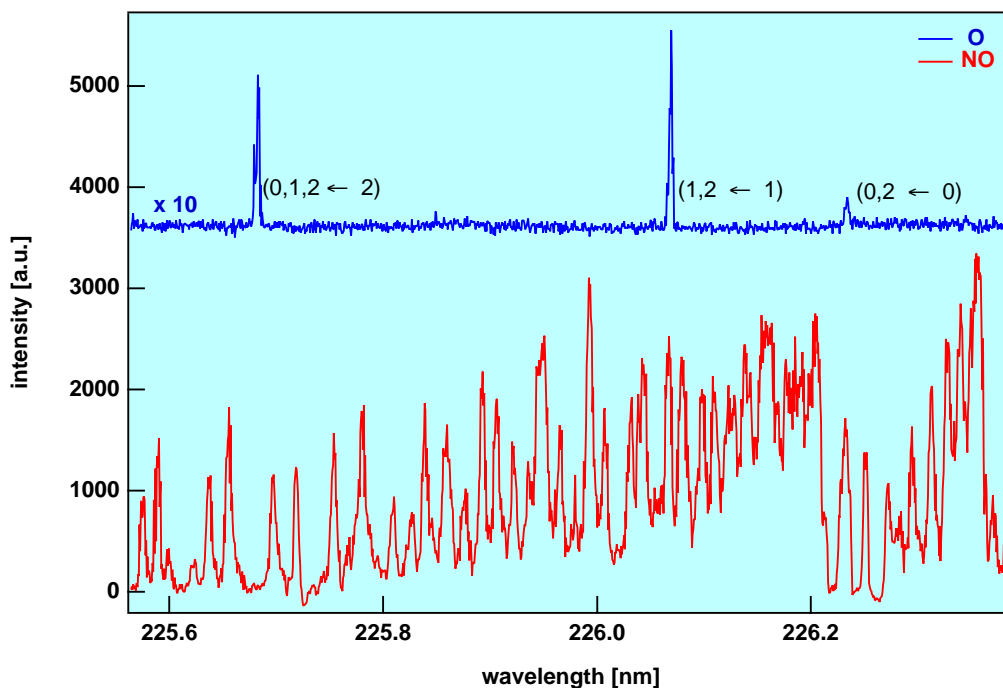


Fig. 3.2: REMPI spectra for NO and O upon  $O_2$  photodissociation [Krenzen, 1999].

1.  $\sigma_{pi} = (5.3 \pm 2.0) \cdot 10^{-19} \text{ cm}^2$  for O-atoms and  $\sigma_{pi} = (7.0 \pm 0.9) \cdot 10^{-19} \text{ cm}^2$  for NO [Bamford, 1986; Zacharias, 1980].

Switching on the dye laser always caused an erratic movement of the stepper motors which drive the grating and the BBO crystal, setting them out of phase with respect to each other. Moreover, the laser pulses heated the BBO crystal which, in turn, expanded until a dynamical equilibrium with the environment was reached. A coarse adjustment of the relative orientation of the BBO crystal to the laser beam was performed after each start-up, once the crystal had reached its thermal equilibrium. It was realized monitoring the intensity of the second harmonic emission with a pyroelectric detector. Then the laser was tuned to 225.655 nm and beam was steered into the HV chamber, where a partial pressure of  $1 \cdot 10^{-4}$  mbar  $\text{NO}_2$  was established. O-atoms were produced upon photodissociation of  $\text{NO}_2$  (Eq. 3.7), and the intensity of the  $\text{O}^+$  ion yield for the  $(0,1,2 \leftarrow 2)$  transition was monitored. Running the laser continuously for some minutes before each experimental run allowed the crystal to thermalize. Then the measured laser fluence stayed remarkably constant: differences in the averaged SH-intensity were less than 5% on the time scale of the experiment.

Initially, the molecular beam was run with a mixture of ca. 10%  $\text{NO}_2$  in  $\text{O}_2$ . Pure  $\text{NO}_2$  at room temperature freezes upon supersonic expansion. Consequently, the pulsed valve gets clogged. Diluting  $\text{NO}_2$  in a carrier gas, this problem was avoided and the pulsed valve could be operated without additional heating. In the seeded beam  $\text{NO}_2$  molecules acquired the same velocity as  $\text{O}_2$  ones. NO was produced upon photodissociation of  $\text{NO}_2$  from the molecular beam. The intense REMPI signal for NO at 226.226 nm was used to initially synchronize the beam with the laser firing. The  $\text{O}^+$  signal at the  $(0,1,2 \leftarrow 2)$  transition was used to synchronize the gate in the acquisition electronics. The same signal was used to synchronize the gate in the acquisition electronics. Before performing the actual Al-oxidation experiments, the gas manifold has been thoroughly degassed under vacuum and successively rinsed with Ar (4.8, Messer-Griesheim) and He (5.0, Messer-Griesheim). Then a molecular beam of  $\text{O}_2$  was allowed in the UHV chamber and the time evolution of the intensity of the most intense NO ionization line, at 226.226 nm, was monitored [Deézsi, 1958]. The gas line was considered clean, when that NO signal was completely extinguished. I am confident that contaminations of the  $\text{O}_2$  beam with  $\text{NO}_2$  have been avoided.

### 3.3 THE BACKGROUND

Apart from ionizing O atoms, photons in the energy range of choice can also dissociate oxygen molecules. At the laser intensities in use, the oxygen atoms stemming from this process might constitute a relevant source of background signal and interfere with the detection of the O-atoms due to the dissociation at the surface. Two main sources of  $\text{O}_2$  contaminating the vacuum of the UHV chamber were present throughout the experiment:

- a partial pressure of  $\text{O}_2$  coming from the background of gas present in the UHV chamber (ca.  $10^{-11}$  mbar);
- $\text{O}_2$  from the molecular beam deflected into the detection volume after scattering with the crystal ( $\leq 10^{-8}$  mbar).

The background from the rest gas was negligible compared to the one from the molecular beam. Moreover, the contribution from the background could be easily eliminated performing coupled measurements: first the O-ion yield was measured with the pulsed valve switched off; then the molecular beam was allowed into the UHV chamber,

and the same measurement was repeated while the beam interacted with the surface. The straight-through valve connecting the molecular beam source to the main chamber was left open in both cases. Point to point subtraction of the first measurement from the second allowed an accurate correction for the background originating from the rest gas in the UHV chamber.

To unravel the contribution from the molecular beam, the interaction of O<sub>2</sub> with UV light has to be considered more carefully. The different possible photodissociation pathways need to be identified to determine the overall number of photons involved in each of those processes. Since the molecule must be photodissociated prior to ionization of one of its fragments, in this case a higher number of photons will be needed to create an ion than in the case of direct (2+1) resonant ionization of atomic oxygen as such. The functional relationship between the ion signal intensity ( $I$ ) and the laser fluence ( $\Phi$ ) is a power law

$$I \propto \Phi^n, \quad (3.8)$$

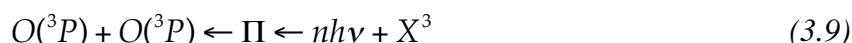
where  $n$  is the overall number of photons needed for the production of one single ion. Measuring the dependence of the ionization signal on the laser fluence it was possible to separate the different contributions to the overall ionization signal.

Upon interaction with UV light, O<sub>2</sub> can dissociate according to one of the following pathways: *optical dissociation* and *pre-dissociation* [Wayne, 1991].

*Optical dissociation* is characterized by dissociation from the electronic state where absorption first occurred. The spectrum of absorption leading to dissociation is a continuum, since the fragments may bear translational energy away from the dissociating molecule, and this energy is not quantized. At some longer wavelength, where it is not followed by dissociation, adsorption to discrete vibrational levels may result in a banded spectrum. These bands get closer together as the restoring force for the vibrations gets weaker. Ultimately, a continuum is reached whose onset energy (*convergence limit*) is the dissociation energy of the products formed.

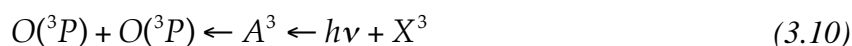
According to the notation in Fig. 3.3, two possible classes of transitions can be considered: the Schumann-Runge and the Herzberg I.

The *Schumann-Runge* system



starts at  $\lambda \sim 200$  nm with a sharp banded spectrum, which converges to its limit at  $\lambda \sim 175$  nm. Its cross section shows a maximum of  $10^{-17}$  cm<sup>2</sup> for  $\lambda \sim 145$  nm and drops sharply at wavelengths shorter than 130 nm [McEwan, 1985]. The laser light for O-atom detection produced with this experimental setup lies in the range between 225.5 nm and 226.3 nm. Hence, the *Schumann-Runge* transitions are energetically forbidden for both one-photon and two-photon processes.

*Herzberg I* transitions



would be energetically allowed as one-photon processes, but they are forbidden for electric dipole interactions. Therefore, optical dissociation can be ruled out in the present context.

**Pre-dissociation**, the second mechanism available for photodissociation, involves the population of an electronically excited state which crosses with a repulsive state. The name was adopted to describe the spectroscopic appearance of an absorption system, whose bands are blurred and diffused at a wavelength longer than the one corresponding to the optical dissociation limit. The spectroscopic diffuseness may be accompanied by chemical fragmentation. Pre-dissociation is understood to arise from the “crossing” of electronic states and the occurrence of radiationless energy transfer between them. Coming back to Fig.

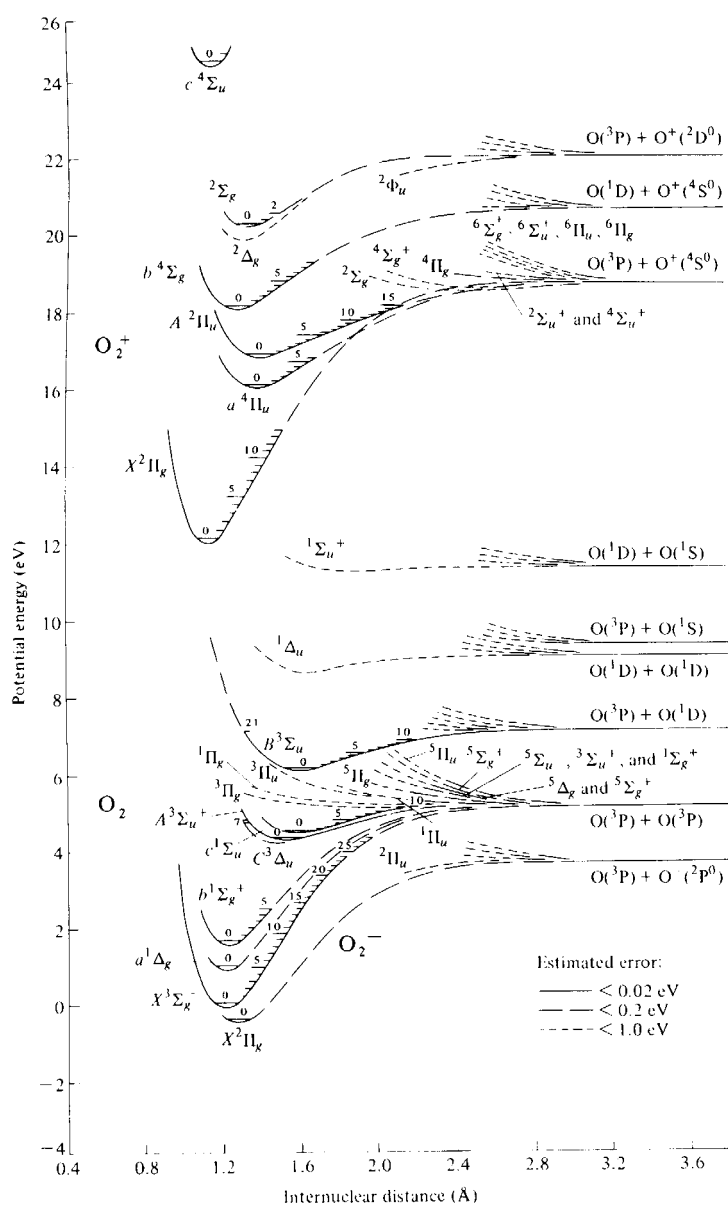
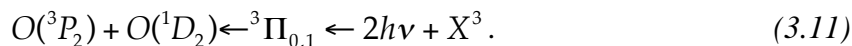


Fig. 3.3: Potential curves for the oxygen molecule and its positively and negatively charged ions [Steinfeld, 1985].

3.3, the simultaneous absorption of two photons may open different pathways, where the molecules are excited directly into one of the repulsive  $\Pi$ -states. As shown in a recent study by Bujisse *et al.*,  $O_2$  photodissociation near 225.65 nm proceeds mainly through the 2-photon excitation of the  ${}^3\Pi_{0,1}$  state and its subsequent predissociation according to the following scheme



Only one of the two atomic fragments is in the ground state and can be detected at the laser frequencies in use. Its counterpart is in an electronically excited state, 1.9 eV above the ground state. In this case, the intensity of the O-ion signal will depend on the 5<sup>th</sup> power of the laser intensity. Each of the 225.655 nm photons carries an energy of 5.49 eV. So this photodissociation reaction is exoenergetic by  $(2 \cdot 5.49 - 5.17 - 1.9) \text{ eV} = 3.91 \text{ eV}$ , producing O-atoms both in the ground state and in the first electronic excited state, with 1.95 eV of excess kinetic energy [Bujisse, 1998].

It might be argued, that at the high laser intensities used throughout this experiment ( $\sim 27 \text{ GW} \cdot \text{cm}^{-2}$ ), multiphoton ionization channels might also be open, which leads to singly and multiply charged *molecular ions*. Normand *et al.* studied the non-resonant disso-

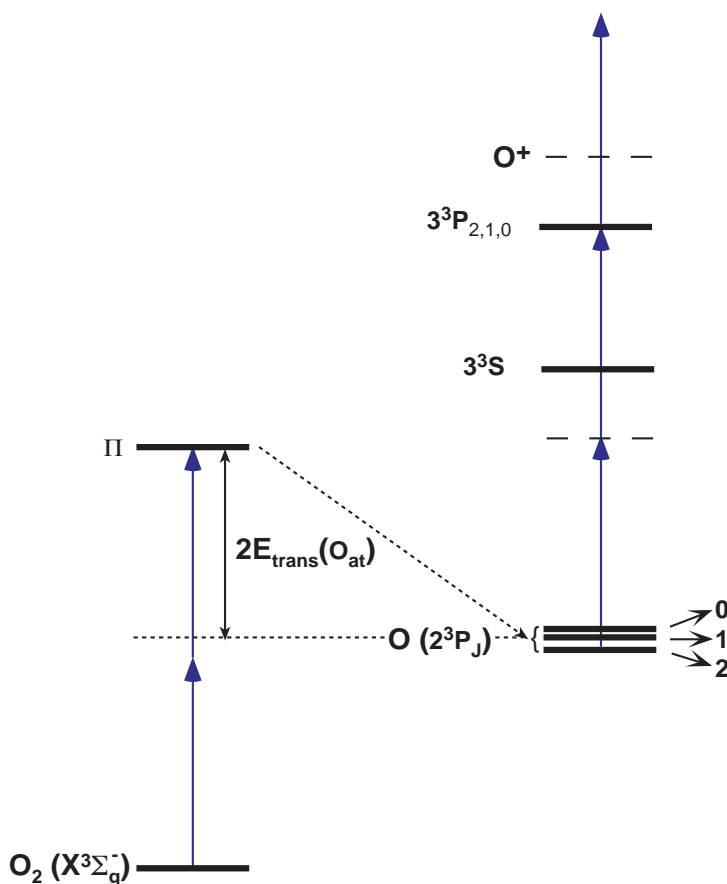


Fig. 3.4: Schematic representation of  $O_2$  photodissociation through a pre-dissociation channel [on the left side of the panel], in relation with (2+1)REMPI of the resulting O-atoms. Laser wavelength = 225.65 nm.

ciative ionization and multiple ionization of  $O_2$  in intense laser fields (up to  $5 \cdot 10^5 \text{ GW} \cdot \text{cm}^{-2}$ ) [Normand, 1991]. For the first ionization of  $O_2$



with 305 nm photons they found  $n=1.5$ . This reaction channel should be open also in our case, but the use of a ToF spectrometer easily allows to separate  $O_2^+$  from  $O^+$  ions due to their different *charge-to-mass* ratio. Using light at 305 and 610 nm,  $O_2^{2+}$  ions were detectable only for laser densities  $> 10^5 \text{ GW} \cdot \text{cm}^{-2}$ , four orders of magnitude higher than the ones available in our experiment. Although in the present case 225.5 nm light was used, the



process would still require more than 7 photons and is, therefore, highly improbable.

In the end, I can expect to detect  $O^+$  ions produced by either one of the following processes:

- (2+1) REMPI of ions produced **after** the photofragmentation of the molecules scattered from the beam, where *five* photons are needed;
- (2+1) REMPI of atoms produced upon **abstractive dissociation** of molecules at the metallic surface, where *three* photons are needed.

A schematical representation of the two processes is shown in Fig. 3.4. Based on Eq. 3.8, the two reaction channels for  $O^+$  production can be separated according to their dependence on the laser fluence.

## 4. EXPERIMENTAL RESULTS

Two independent STM studies suggested the existence of randomly distributed single O-atoms on the surface of an Al(111) single crystal, after exposure to thermal O<sub>2</sub>. To rationalize these findings, a reaction mechanism has been proposed whereby the surface abstracts one O-atom from the incoming molecule. The abstracted atom chemisorbs, while the recoiled atom permanently escapes the surface [Brune, 1992; Binetti, 2000].

Hereafter, I give experimental evidence for the existence of such a chemisorption pathway, during the first stage of the surface oxidation. The recoiled O-atoms were ionized by means of a (2+1) resonant multi-photon process and, eventually, detected with a ToF mass spectrometer. This work constitutes the first direct experimental demonstration for the existence of an abstraction pathway in the oxidation of an elemental metal surface.

In order to clarify the dynamics of this process, I studied the yield of the reaction as a function of both the polar incidence angle of the incoming molecules and of their translational and rotational energy. The energy distribution of the emitted atoms was also investigated.

### 4.1 THE INSTRUMENTAL FUNCTION OF THE REMPI-TOF SPECTROMETER

The flight-time of an ion through the REMPI-ToF spectrometer depends on its  $q/m$  ratio as well as on its initial kinetic energy. This flight-time can be explicitly calculated, by solving the equation of motion for ions propagating from the laser focus to the detector plates as a function of time. With reference to the diagram in Fig. 4.1, the complete ion trajectory can be divided into four sections, according to the characteristics of the ion motion. In the following, for the sake of simplicity, I will assume that the electric fields  $\vec{E}_1$ ,  $\vec{E}_2$  and  $\vec{E}_3$  are uniform. The electric field inside the ToF-tube tube is zero.

The ion is uniformly accelerated when moving between the laser focus and the ToF-tube entrance. This fraction of the flight-time lasts  $t_1$ ,

$$t_1 = -\frac{v_0}{a_1} + \sqrt{\left(\frac{v_0}{a_1}\right)^2 + 2 \cdot \frac{d_1}{a_1}}, \quad (4.1)$$

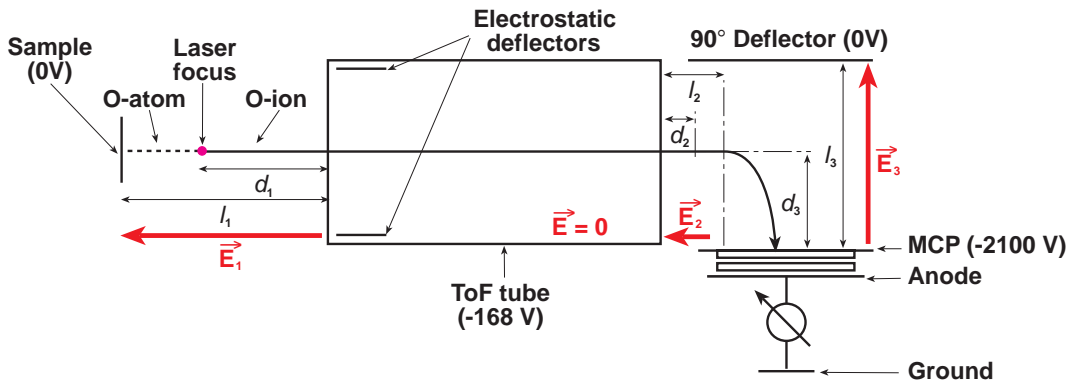


Fig. 4.1: Diagram for the calculation of the trajectories of O-ions inside the ToF-spectrometer.

where  $v_0$  is the initial velocity of the ion parallel to the axis of the ToF-tube, directed toward its entrance, and  $a_1$  is the acceleration due to the electric field in that region. The distance between the laser focus and the ToF-tube entrance,  $d_1$ , is fixed to 30 mm. The ions drift through the ToF-tube with constant velocity

$$v_1 = \sqrt{v_0^2 + 2 \cdot d_1 \cdot a_1} . \quad (4.2)$$

The length of the tube ( $l_{\text{ToF}}$ ) is 80 mm and the correspondig flight-time is

$$t_{\text{ToF}} = \frac{l_{\text{ToF}}}{v_1} \quad (4.3)$$

The ToF-tube is 5 mm away from the border of the MCP holder ( $d_2$ ). The ions leaving the ToF are accelerated along rectilinear trajectories before being deflected toward the MCP [Fig. 2.4]. This fraction of the flight-time lasts

$$t_2 = -\frac{v_1}{a_2} + \sqrt{\left(\frac{v_1}{a_2}\right)^2 + 2 \cdot \frac{d_2}{a_2}} , \quad (4.4)$$

with  $a_2$  being the acceleration due to the potential difference between the point where the ions leave the ToF-tube and the inflection point of their trajectory. The MCP holder and the 90° deflector can be seen as the parallel expansion of a plane parallel capacitor, whose field  $\mathbf{E}_3$  is perpendicular to the ToF-tube axis and to the initial direction of the ion motion. In this region, the motion of the ion is uniformly accelerated but independent from the previous kinematics. The duration of this fraction of the flight-time is

$$t_3 = \sqrt{2 \cdot \frac{d_3}{a_3}} , \quad (4.5)$$

where  $d_3$  is the distance between the exit point of the ion from the ToF-tube and the MCP, along the normal to the MCP plane. Since the ToF-tube has a diameter of 30 mm,  $d_3$  can vary between 15 mm and 45 mm. The accelerations  $a_i$  are given by

$$a_i = \frac{\Delta V_i \cdot q}{l_i \cdot m_O} , \text{ with } i = 1, 2, 3, \quad (4.6)$$

where  $q$  is the ion charge and  $m_O$  is its mass. The potential differences  $\Delta V_1$  and  $\Delta V_3$  are respectively measured between the sample and the ToF tube, and between the ToF-tube and the MCP; the distances  $l_1$  and  $l_3$  are measured between the sample and the ToF-tube entrance, and between the 90° deflector and the MCPs front plate.  $\Delta V_2$  is the potential difference between the ToF-tube and the inflection point of the trajectory: it amounts approximately to -400 V [Fig. 2.4]. The distance between the exit of the ToF-tube and the inflection point,  $l_2$ , is approximately 10 mm. The total flight time between the laser focus and the front plate of the MCPs is

$$t_{\text{flight}} = t_1 + t_{\text{ToF}} + t_2 + t_3 . \quad (4.7)$$

Since the time  $t_2$  amounts to less than 3% of the overall flight-time, the value of  $t_{\text{flight}}$  is rather independent from the details of the electrical field  $\mathbf{E}_2$ . Its inaccuracy is not expected to noticeably affect the results of Eq. 4.7.

The REMPI-ToF spectrum shown in Fig. 4.2 was measured upon photodissociation of  $O_2$  molecules from a thermal molecular beam. It was recorded with the dye laser set at a laser wavelength of 225.655 nm, corresponding to REMPI from the  $2^3P_2$  oxygen state. The sample, facing the ToF, was located outside of the molecular beam, 20 mm away from the laser focus. The electronic noise, occupying the first  $2\ \mu\text{s}$  of the spectrum, is due to stray laser light and has been filtered out in the figure. Its onset is taken as the origin of the time scale for the spectrum. A bimodal distribution of O-atoms is detected. The two components, named *Fast* and *Slow* in the picture, have a width (FWHM) of  $0.24\ \mu\text{s}$ . At the wavelengths in use, each photon carries an energy of 5.49 eV. As shown in Section 3.3, the 2-photon photodissociation of  $O_2$  is exothermic by  $\Delta E = 3.91\ \text{eV}$  and leaves the two fragments with a kinetic energy of 1.95 eV each [Bujisse, 1998]. Due to geometrical constraints of the experimental setup, the polarization plane of the laser formed an angle of ca.  $45^\circ$  with the axis of the ToF-tube. The trajectories of fragments originated upon photodissociation of molecules with their axis parallel to the laser polarization plane, form an angle of approximately  $45^\circ$  with the axis of the ToF tube. Because of the approximation used in the calculation, the calculated flight-times are ca. 10% lower than the measured ones. The resulting energy difference of the fragments accelerated in opposite directions is  $\Delta E \cdot \cos^2(\pi/4) = 1.00\ \text{eV}$ . The separation of the two peaks ( $0.32\ \mu\text{s}$ ) allows to estimate the energy resolution possible with the present configuration of the REMPI-ToF spectrometer. The choice of a lower extracting voltage would enhance the peak separation and the energy resolution at the expenses of the detection efficiency. An extracting voltage of -168 V was chosen as the best compromise. Due to the angle between the laser polarization and the ToF-tube axis, the two components could not be detected with the same efficiency and the *Slow* component appears to be ca. 25% of its *Fast* counterpart. This is a general effect due to the asymmetry of the electric field in front of the entrance of the ToF tube and was confirmed by means of ion trajectory simulations. The FWHM

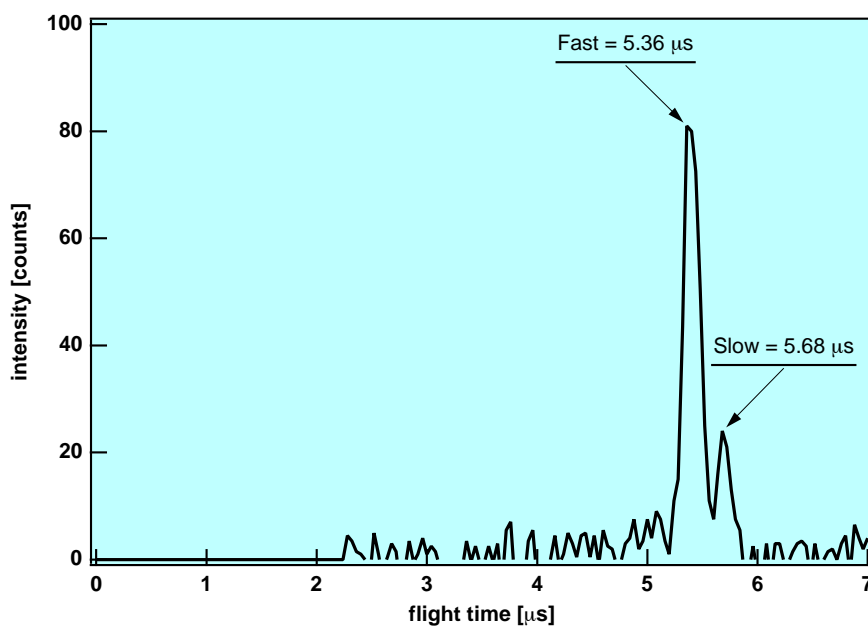


Fig. 4.2: Time-of-Flight spectrum of atomic oxygen detected after photodissociation of  $O_2$  from a thermal molecular beam. The electronic noise between  $t = 0 \div 2\ \mu\text{s}$  is due to stray laser light. Laser wavelength = 225.655 nm.

for the measured peaks is caused by the spread of the trajectories inside the ToF-tube: the difference in the flight-time calculated for  $d_3$  values of 15mm or 45mm, amounts to 300ns. The slightly narrower experimental widths of 240ns may be explained by a focusing effect of the four electrostatic deflectors located at the entrance of the ToF-tube. A summary of the experimental and calculated values for these quantities is given in Table 4.1.

#### 4.2 DETECTION OF RECOILED O-ATOMS FROM THE ABSTRACTIVE CHEMISORPTION

A typical ToF spectrum recorded upon interaction of a thermal O<sub>2</sub> beam (translational energy,  $E_{\text{trans}}=90\text{meV}$ ) with a freshly prepared Al surface is shown in Fig. 4.3. The angle between the beam and the surface normal (polar incidence angle,  $\theta$ ) was 45°. The circular diaphragm shaping the molecular beam prior to the access to the UHV chamber had a diameter of 3mm. The laser wavelength was tuned to 225.655nm and had an intensity of 0.71mJ/pulse. It was focused 6mm away from the crystal surface. The spectrum shows the accumulated intensity after 500 pulses. It was acquired with the detection scheme depicted in Fig. 2.9A. Two components are resolved in the time domain. Both of them disappeared when the laser wavelength was detuned, showing that they both resulted from the ionization of O-atoms. The flight-time difference suggests that the ensemble of O-atoms probed by the laser beam is characterized by a bimodal kinetic energy distribution. According to the previous analysis of the photodissociation processes at the laser wavelength in use [Section 3.3], two different reactions pathways should be active:

- 2-photon photodissociation of O<sub>2</sub>, followed by (2+1)REMPI detection of the fragments, already discussed in the previous section;
- (2+1)REMPI detection of O-atoms produced upon interaction of O<sub>2</sub> molecules from the beam with the metal surface.

The chemisorption of one single O-atom is estimated to be exothermic by 7.95eV [Jacobsen, 1995]. This energy release is enough to cause the dissociation of the O<sub>2</sub> molecule. In this case, 2.75eV excess energy has to be dissipated as translational energy of the O atoms, in the creation of *electron-hole* pairs in the metal and in the heat bath of the metal. If the molecule approaches the crystal with its axis perpendicular to it, a fraction of the exothermicity may allow the outer atom to permanently leave the surface. In other words, the surface may abstract an O-atom from the incoming molecule. The exact value for the kinetic energy of the recoiled atom depends on the details of the reaction. Nevertheless, it will be surely smaller than the kinetic energy of the atoms detected upon photodissociation of O<sub>2</sub> molecules [Section 4.1, Fig. 4.2]. The viability of these two reaction channels could explain the existence of the two components in the measured spectrum.

**Table 4.1: Comparison of the measured and calculated flight-times for O<sup>+</sup> ions**

	Flight-time <i>Fast</i>	Flight-time <i>Slow</i>	FWHM	$\Delta t(\text{Slow-Fast})$
measured	5.36 $\mu\text{s}$	5.68 $\mu\text{s}$	0.24 $\mu\text{s}$	0.32 $\mu\text{s}$
calculated	4.50 $\mu\text{s}$	5.00 $\mu\text{s}$	0.30 $\mu\text{s}$	0.50 $\mu\text{s}$
deviation	12.8%	9.0%	-20.0%	-56.3%

Namely, the slow component should derive from the photoionization of abstraction fragments, while the fast component should result from the photoionization of O-atoms produced upon photodissociation of  $O_2$  from the molecular beam [Eq. 3.11, Fig. 3.4]. The number of photons needed to generate an O-ion is different in the two cases: the (2+1)REMPI process requires 3 photons; (2+1)REMPI following the 2-photon photodissociation requires 5 photons. Hence, according to Eq. 3.8, the two peaks should show a different functional dependency on the laser fluence. Fitting the equation of a power law

$$I = k\Phi^n \quad (4.8)$$

to the experimental data, the value of the exponent  $n$  corresponds to the total number of photons needed for the ionization. In the factor  $k$ , the instrumental sensitivity as well as the cross-sections characterizing the multi-photon processes are convoluted.

For a monochromatic source, the fluence at the characteristic wavelength is directly proportional to the pulse energy. In Fig. 4.4, the accumulated intensities for each of the two peaks in Fig. 4.3 are plotted as a function of the laser pulse energy. The pulse energy is already corrected for the propagation losses due to the optics. The open symbols show the intensity of the slow channel and the solid symbols show the intensity of the fast channel. The lines represent fits to the experimental data consistent with Eq. 4.8. The fitting parameters are listed in Table 4.2.

For the upper curve, the value  $n=2.49\pm 0.07$  indicates a three photon process, where partial saturation of at least one of the steps in Eq. 3.2 and Eq.3.3 occurs. This is consistent with (2+1)MPI of O-atoms (and is therefore denoted *atomic*). The value  $n=4.44\pm 0.57$  for the lower curve shows that a more complex mechanism is taking place where five photons are involved: in this case, an  $O_2$  molecule must be photodissociated in

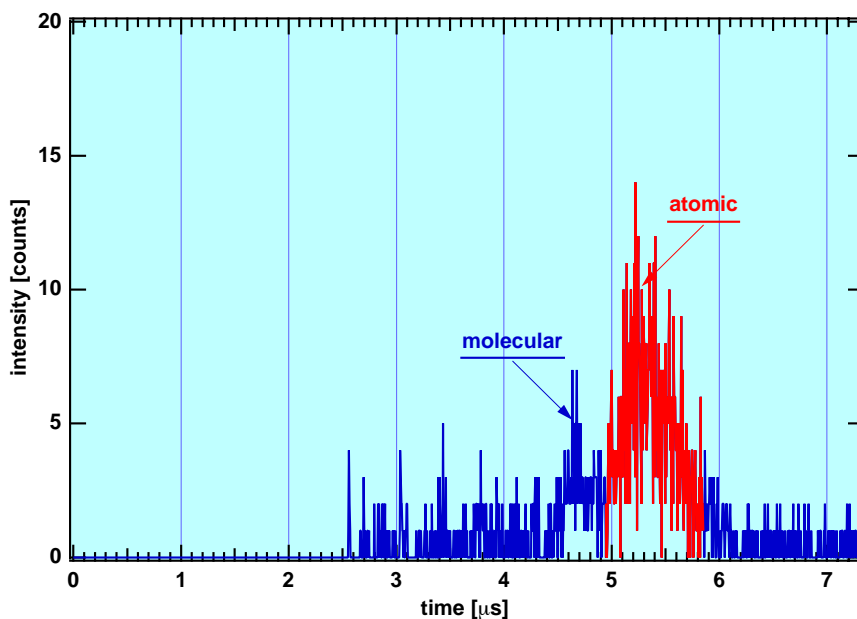


Fig. 4.3: ToF spectrum of atomic oxygen detected upon interaction of a thermal molecular beam of oxygen ( $E_i = 90$  meV) with the (111) surface of an aluminum single crystal.

**Table 4.2: Fitting parameter for the curves in Fig. 4.4**

Curve	$n$	$k$	$\sigma(n)$	$\sigma(k)$
atomic	2.49	1739.1	0.07	46.3
molecular	4.44	658.9	0.57	158.0

the gas phase, before ionization of one of its fragments. Again, partial saturation of the processes involved in the overall photoionization reaction is responsible for the deviation from the expected value of 5. This channel is correspondingly denoted *molecular*. Apart from supporting the previous interpretation of Fig. 4.3, Fig. 4.4 constitutes the first direct experimental evidence for the existence of an abstractive pathway for the chemisorption of oxygen on aluminum. The results in Fig. 4.2 show, that the contribution to the REMPI signal from the O<sub>2</sub> photofragments initially accelerated toward the ToF tube (identified with the *molecular* component in Fig. 4.3) is approximately four times more intense than the one due to O<sub>2</sub> photofragments initially directed away from the ToF tube. According to the simulation in Section 4.1, the latter should appear approximately 6  $\mu$ s after the time origin in Fig. 4.3. Being comparable to the background noise, it could not be resolved in this experiment.

In the following measurements a circular diaphragm with a diameter of 2mm was used to limitate the diameter of the molecular beam. The cross section of the molecular beam at the sample location was thus reduced to 3.2mm. Hence, the amount of O<sub>2</sub> scattered from the molecular beam into the volume probed by the laser, was reduced. The laser focus was moved to a distance of 10mm from the surface, along its normal. The

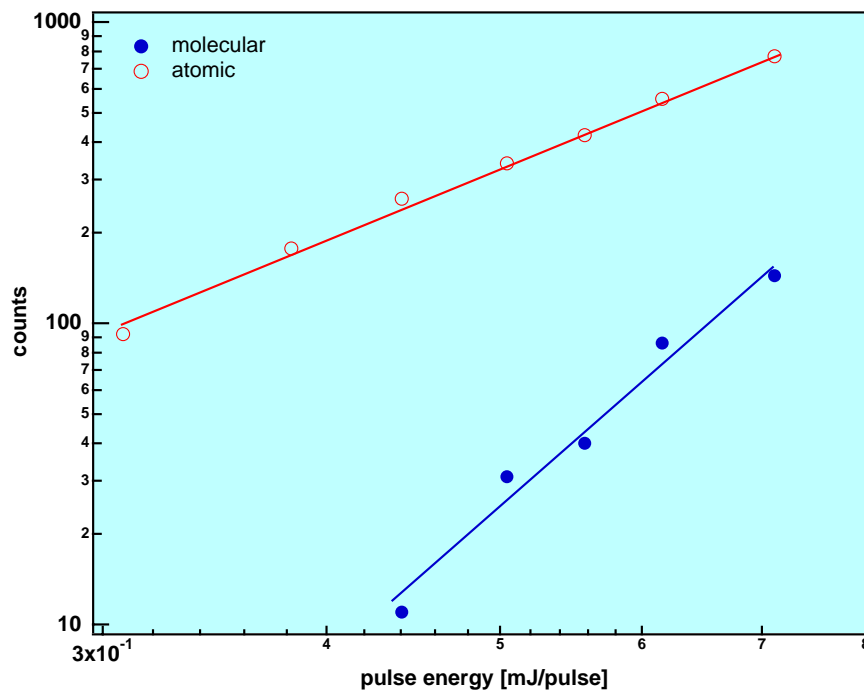


Fig. 4.4: Accumulated intensity for each of the two peaks in Fig. 4.3, as function of the laser fluence. The solid lines are fits to the Eq. 4.8.

overlap between laser and molecular beams was reduced further, orienting the surface normal at an angle of  $45^\circ$  with respect to the incoming  $O_2$  beam. This reduced the chemisorption efficiency to 80% of its peak value, but the fast component in the detected signal was reduced below the sensitivity of the REMPI-ToF spectrometer [cf. Section 4.4].

### 4.3 ENERGETIC DISTRIBUTION OF THE RECOILED ATOMS

ToF spectra of the O-atoms emitted during the initial oxidation of the Al(111) surface were recorded using a multi-channel scaler, according to the detection scheme depicted in Fig. 2.9A. The time resolution of the instrument,  $10^{-8}$ s, affects the determination of the kinetic energy by less than 2%. The Q-switch circuitry of the Nd:YAG pump laser provided the trigger signal for the scaler. The laser power was controlled before and after each single experimental run. It was regulated to 1.5 mJ/pulse during the whole experiment. The molecular beam energy could be varied by means of heating and seeding techniques [Section 2.2.1].

Each of the ToF spectra in the following Fig. 4.5 was recorded during the first stage of the oxidation of a clean Al(111) surface, typically between 5 and 10 minutes after its preparation. Each spectrum resulted from the accumulation of 500 gas pulses. The background was corrected by point to point subtraction of blank spectra, recorded while blocking the molecular beam prior to its access into the UHV chamber.

The absolute sticking coefficient of  $O_2$  on Al as a function of  $O_2$  translational energy has recently been measured by Österlund *et al.* [Österlund, 1997]. Starting from their results, I estimated the amount of oxygen adsorbed onto the surface ( $\Theta$ ) during these experiments. It was always well below 1/100 of a monolayer, assuring that only the initial stage of the chemisorption process was investigated in these experiments. The estimated coverages are shown in Table 4.3.

According to the manufacturer specifications, the laser pulses are shorter than 10 ns. The motion of the atoms during this time interval can safely be neglected. Hence, each laser pulse probed the density of atoms present at its focus, when the photons reached that location. The gas pulses lasted approximately  $160 \mu\text{s}$ , four orders of magnitude longer than the laser pulses. The laser was synchronized so, that the light pulse reached the focus location approximately  $80 \mu\text{s}$  after the gas pulse hit the sample. A simple calculation allows to estimate the lower limit for the kinetic energy of the detected O-atoms. Atoms released when the leading edge of the gas pulse hits the sample, must reach the location of the laser focus simultaneously with the laser beam in order to be ionized and

**Table 4.3: Oxygen coverage accumulated during the ToF experiment**

$E_{\text{trans}}$ [meV]	$\Theta$ [Langmuir]
90	0.0005
135	0.0026
187	0.0030
313	0.0034

eventually detected. Therefore, their velocity normal to the surface must be at least  $v_{\text{th}} \geq (10 \cdot 10^{-3} / 80 \cdot 10^{-6}) = 125 \text{ m/s}$ . This limits to 1 meV the minimal kinetic energy detectable with this experimental setup<sup>1</sup>.

In order to extract the energy distribution of the emitted atoms from the ToF spectra, two different approaches were followed. First, in a more qualitative way, the FWHM of the O-peaks in Fig. 4.2 and their respective delay were used to calibrate both the time scale and energy scale of the ToF spectra. Alternatively, given the equation of motion of the O-ions in the ToF-spectrometer [Section 4.1], the measured flight-time distribution was transformed into an energy distribution. Fitting the resulting energy distribution to an exponential curve, the most probable energy for the emitted O-atoms was determined.

The FWHM(O<sub>2</sub>) of the O-peak from O<sub>2</sub> photodissociation, 0.24  $\mu\text{s}$ , gives a reasonable estimate of the instrumental function of the REMPI-ToF spectrometer. The FWHM of the O-peak due to the abstraction at the surface ( $\Omega_{\text{exp}}$ ), is approximately 0.6  $\mu\text{s}$ . This second peak represents the convolution of the instrumental function of the spectrometer, with the width of the time of arrival distribution for O-atoms generated in the abstraction process ( $\Omega$ ).  $\Omega$  arises from two different effects: the geometrical distribution of O-atom trajectories starting from the Al surface after abstraction as well as actual differences in the translational energy of the outgoing O-atoms ( $\Omega_{\text{int}}$ ). The sample is a disk of 10 mm diameter. The focus is located 10 mm away from the sample. The laser beam waist is 26.3  $\mu\text{m}$  and can be considered as pointlike with respect to the sample. The acceptance angle ( $\alpha$ ) for the MPI process is defined as the aperture of the circular cone, whose vertex coincides with the laser waist and whose base is delimited by the sample. The O-atoms whose trajectories are contained in this cone, pass through the laser focus, can be ionized and, eventually, detected. An upper limit for the divergency of these trajectories is given by

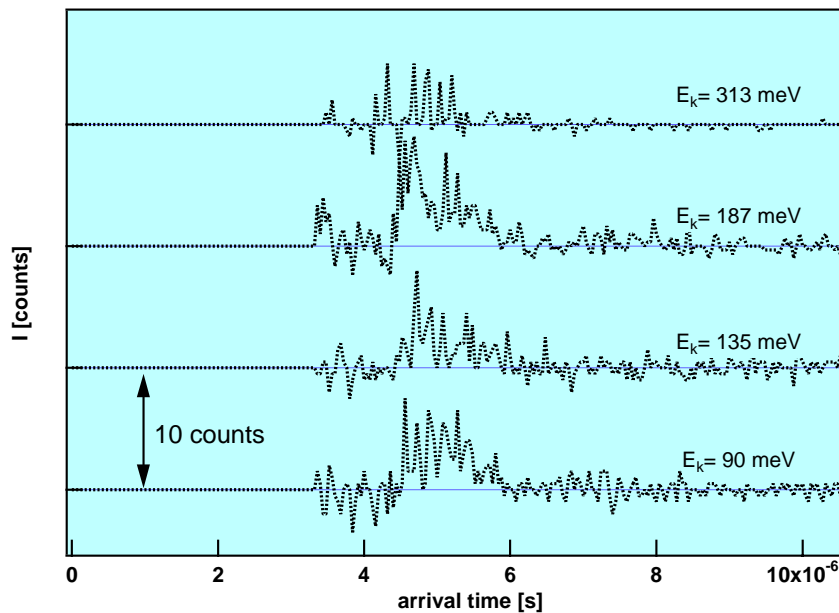


Fig. 4.5: ToF spectra of O-atoms emitted during the first stage of the Al(111) oxidation. The translational energies of the molecular beam are indicated.

1. For single atoms, kinetic and translational energies coincide.

$$\alpha = \arctan\left(\frac{5}{10}\right) \approx 27^\circ. \quad (4.9)$$

Since these atoms move on diverging trajectories, their velocity along the surface normal will be modulated by a  $\cos(\alpha)$  factor and, accordingly, their kinetic energy will be modulated by a factor  $\cos(\alpha)^2$ . This geometric broadening ( $\Omega_{\text{geom}}$ ) of the O-atom peak can only explain flight-time differences up to  $0.020 \mu\text{s}$ , much smaller than the measured broadening. Approximating the convolution of the distribution functions with the sum of the FWHM and the other broadening sources, I obtain the following estimate for  $\Omega_{\text{int}}$

$$\Omega_{\text{int}} = \Omega_{\text{exp}} - \left[ \text{FWHM}(\text{O}_2) + \Omega_{\text{geom}} \right] \approx 0.1 \mu\text{s}. \quad (4.10)$$

This implies a translational energy of the recoiled O-atoms ( $E_{\text{trans}}$ ) of  $\approx 0.400 \text{ eV}$ .

The ToF spectra shown in Fig. 4.5, were measured for molecular beams of different translational energies. They show common onsets and ends of O-atoms emission, meaning that the translational energy of the recoiled atoms is independent from the translational energy of the incoming molecules. This ToF spectra shows the distribution of the recoiled atoms in the domain of time, as a function of the detection time  $t_{\text{flight}}$ . Since the relationship between  $t_{\text{flight}}$  and the kinetic energy of the atoms  $E_{\text{trans}}(\text{O})$  is known [cf. Eq. 4.7], the intensity in ToF spectra can be displayed as a function of  $E_{\text{trans}}(\text{O})$  and the average kinetic energy of the recoiled atoms can be determined. The equation linking the measured to the transformed spectrum is

$$\frac{dI}{dt} = \frac{dI}{dt} \cdot \frac{dE}{dE} = \frac{dI}{dE} \cdot \frac{dE}{dt}. \quad (4.11)$$

Therefore

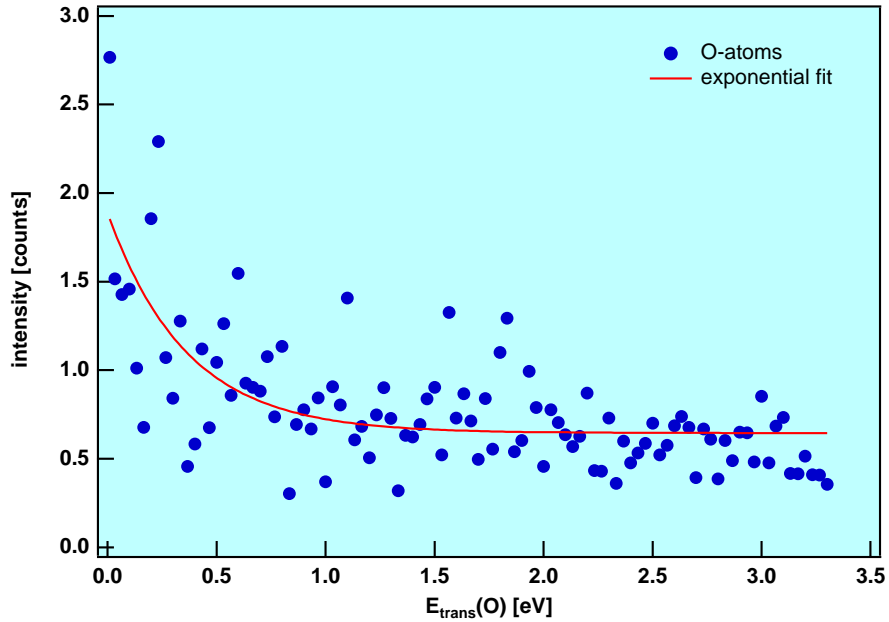


Fig. 4.6: Energy spectrum of O-atoms emitted during the first stage of the Al(111) oxidation.

$$\frac{dI}{dE} = \frac{dI}{dt} \cdot \frac{dt}{dE} . \quad (4.12)$$

Such a transformed spectrum is shown in Fig. 4.6, together with a fitting function of the type  $I \approx a \cdot \exp[-(E/E_0)] + b$ , where  $b$  is an offset accounting for the background.  $E_0$  is the average energy of the distribution. The noisy appearance of the spectra is due to the limited number of counts, *i.e.* the low *signal-to-noise* ratio of the measurement.

The analytical expression for  $t_{flight}$  as a function of  $E_{trans}(O)$  needed for the transformation could be determined through Eq. 4.1-4.4, but this procedure is cumbersome. Therefore, the expression was determined numerically, fitting a polynomial to the curve obtained calculating  $t_{flight}$  for several values of  $E_{trans}(O)$ . The use of a parabola gave the excellent result shown in Fig. 4.7.

Due to the limitations in the model, Eq. 4.7 underestimates the experimental flight-times by 12%.<sup>1</sup> This effect was accounted for in the calculated flight-times displayed in figure Fig. 4.7 and should not affect the present determination of O-atom kinetic energy. The mean values of  $E_{trans}(O)$  obtained in this way are displayed in Table 4.4, together with their uncertainties  $\Delta E$ , the mean values of the translational energy of the impinging  $O_2$  molecules  $E_{trans}(O_2)$  and of the speed of the recoiled O-atoms. The uncertainty on  $E_{trans}(O)$  is the variance of  $E_0$  calculated during the fitting procedure. The mean value for the speed was derived from the translational energy as

$$\langle v(O) \rangle = \sqrt{2 \langle E_{trans}(O) \rangle / m_O} . \quad (4.13)$$

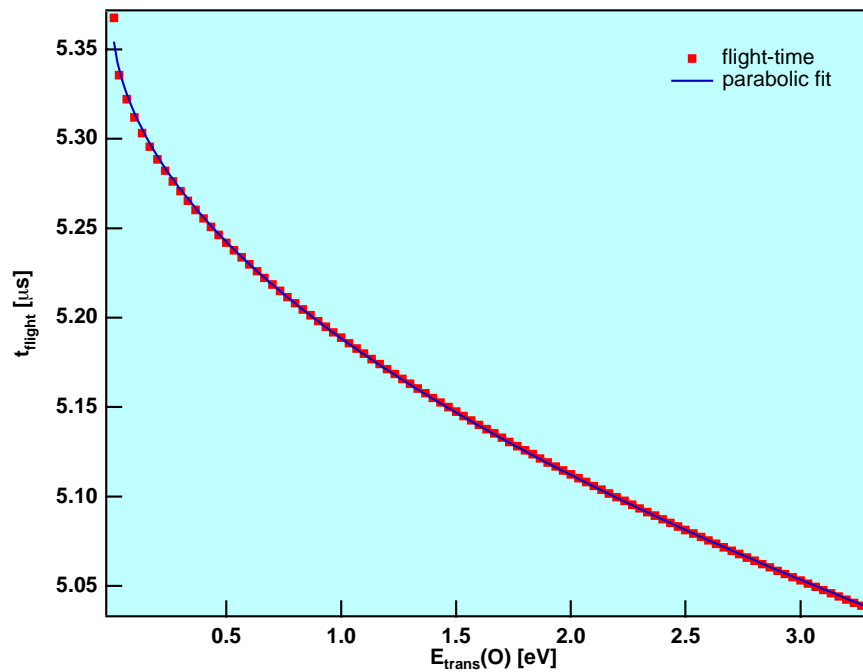


Fig. 4.7: The total flight time  $t_{flight}$ , as a function of the translational energy of the emitted O-atoms  $E_{trans}(O)$ .

1. According to a standard error propagation analysis, this should affect the accuracy of the translational energy determination by less than 16%.

A significant variation, 250%, in  $E_{\text{trans}}(\text{O}_2)$  left the average mean  $E_{\text{trans}}(\text{O})$  unchanged: the 4% variation of  $\langle E_{\text{trans}}(\text{O}) \rangle$  with  $E_{\text{trans}}(\text{O}_2)$  is well within the error margin of the  $E_{\text{trans}}(\text{O})$  determination, that is close to 20%. Therefore, I can conclude that the recoiled O-atoms showed an average mean  $E_{\text{trans}}$  of  $379 \pm 83 \text{ meV}$  and speed of  $2135 \pm 299 \text{ m/s}$ . These quantities are independent from the translational energy of the incident molecules, within the experimental accuracy.

The two different approaches illustrated above produce consistent results. In the following, the value of  $379 \pm 83 \text{ meV}$  for  $E_{\text{trans}}$  of the O-atoms will be adopted, because of the higher accuracy of the underlying fitting procedure.

#### 4.4 O-ATOMS EMISSION AS FUNCTION OF THE INCIDENT ANGLE

Complicated reactions like the dissociative sticking of molecules at surfaces occur on multidimensional Potential Energy Surfaces (PES), where a range of activation barriers may exist. Their magnitude depends on different parameters like the orientation of the incoming molecule, the point of impact on the surface unit cell, the internal excitation of the molecular degrees of freedom and so on. The translational energy,  $E_{\text{trans}}$ , of an incoming particle is usually one of the most important parameters governing the initial sticking probability,  $S_0$ , during reactive scattering. Studies of the dependence of  $S_0$  on the polar angle of the incoming beam, can help unraveling the details of the PES.

Although  $E_{\text{trans}}$  is a scalar quantity, it is usual to resolve it into two ‘‘components’’, *normal* ( $\perp$ ) and *parallel* ( $\parallel$ ). The two terms are referred to the components of the velocity of the incident molecule with respect to the crystal surface. In a scattering experiment, the polar incident angle ( $\theta$ ) is the angle formed by the molecular beam with the normal to the surface. The normal component of the velocity is

$$v_{\perp} = v \cos \theta \quad (4.14)$$

and the respective translational energy

$$E_{\perp} = \frac{1}{2} m_{\text{O}_2} v_{\perp}^2. \quad (4.15)$$

$E_{\perp}$  scales with the incident angle as

$$E_{\perp} \propto \cos^2 \theta. \quad (4.16)$$

**Table 4.4: Translational energies for O-atoms emitted during the initial oxidation of Al(111)**

$\langle E_{\text{trans}} \rangle(\text{O}_2)[\text{meV}]$	$\langle E_{\text{trans}} \rangle(\text{O})[\text{meV}]$	$\Delta E[\text{meV}]$	$\langle v \rangle(\text{O})[\text{m/s}]$
90	360	83	2083
135	376	88	2128
187	392	83	2173
313	385	78	2154

If  $S_0$  depends only on  $E_{\perp}$  of the incoming molecules, it scales as the square of the cosine of the incidence angle. In such cases,  $S_0$  is said to follow the Normal Energy Scaling (NES).

In their molecular beam scattering experiment on the chemisorption of  $O_2$  on Al(111), Österlund *et al.* demonstrated that  $S_0$  does not follow NES, but shows the peculiar dependence on the polar angle illustrated in Fig. 4.8 [Österlund, 1997]. Since abstraction is one of the possible processes leading to O-atom chemisorption on aluminum surfaces, it is natural to investigate if it shows an angular dependency similar to the one shown by  $S_0$ .

The O-yield was defined as the ratio of the accumulated O-atoms counts to the number of pulses and was studied as a function of the incident polar angle. Accumulated ToF spectra for 500 gas pulses were acquired by means of a multi-channel scaler (detection scheme in Fig. 2.9A). The polar angle was varied rotating the sample around its vertical axis. At the same time, the relative position of the REMPI-ToF detector and sample were adjusted to leave the focus in a fixed position, 10 mm away from the surface of the sample, along its normal. The laser intensity measured at the laser output port was kept at a constant value of 2.5 mJ/pulse. The  $O_2$  beam energy was varied between 90–313 meV heating the nozzle and seeding  $O_2$  in He, according to what is reported in Table 2.1. After subtraction of the background, the number of O-atoms was obtained by integration of the peak attributed to the O-atoms resulting from abstractive dissociation. The data in Fig. 4.9 are scaled to account for changes in the  $O_2$  partial pressure, due to different seeding and heating of the beam.

The yield is peaked around  $30^\circ$ , similarly to what has been measured for the sticking probability [Österlund, 1997]. Caution must be taken when comparing the two sets of experimental data at small incident polar angles. Under such conditions, the molecular beam crosses the laser focus and an increased background due to direct photodissociation of both incoming and backscattered  $O_2$  molecules might cause an apparent reduction

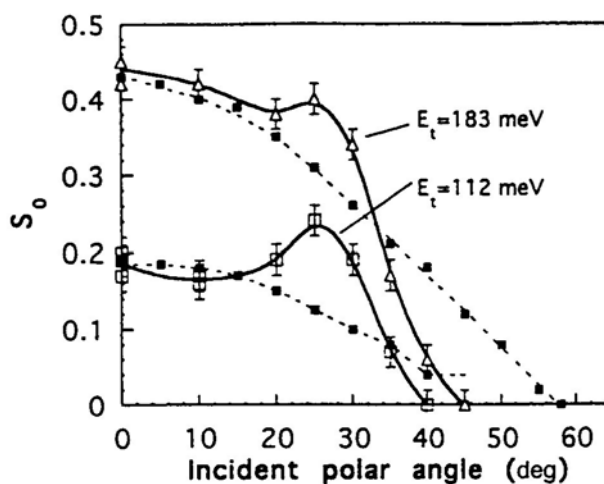


Fig. 4.8:  $S_0$  as a function of incident polar angle at two different molecular beam energies:  $E_{trans} = 112 \text{ meV}$  and  $E_{trans} = 183 \text{ meV}$ . The filled symbols and the broken line show the expected  $S_0$  values, if NES applies. The solid line is to guide the eye [Österlund, 1997].

of the signal coming from the surface reaction. Moreover, from previous experience with the same experimental apparatus, it is known that the detection efficiency of the ToF spectrometer is dependent on the relative orientation of its axis with respect to the sample normal. When dealing with very low signals, as it is the case for  $\theta$  close to  $0^\circ$ , an optimal setting of the spectrometer potentials might be difficult to achieve, furtherly reducing an already faint signal. For these reasons, the sensitivity of our REMPI-ToF spectrometer is non-optimal at small incidence angles. The situation is different at higher  $\theta$ , due to the reduced background. As  $\theta$  was raised above  $30^\circ$ , the abstraction efficiency also decreased, in qualitative agreement with the findings of Österlund *et al.* The signal decrease measured in this study is much slower than the one expected according to their data. In an attempt to clarify the reasons of this discrepancy, I studied the relative sticking coefficient of  $O_2$  on Al(111) as a function of the incident polar angle using AES to detect the chemisorbed oxygen. Here I assumed, that at the given experimental condition the amount of subsurface oxygen is negligible and the relative intensity of the measured AES peak for metallic Al is directly proportional to the number of chemisorbed atoms on the surface. The topic of quantitative Auger electron spectrometry will be discussed more in detail later [cf. Section 4.4.1]. At this stage, I will present some considerations concerning the surface sensitivity of this technique.

The sensitivity of AES is restricted to the first monolayers because the escape probability for an electron emitted by an atom in an Auger transition decays exponentially as the distance between the source and the surface increases. To quantify this concept, the *inelastic mean free path* (IMFP) for the electrons is defined. This is a measure of the average distance travelled by an electron through a solid, before being inelastically scattered. IMFP depends on the initial kinetic energy of the electron and the chemical composition of the solid. Most metals show very similar relationships between the IMFP and the incident energy and a general equation can be extrapolated. Nevertheless, for a more

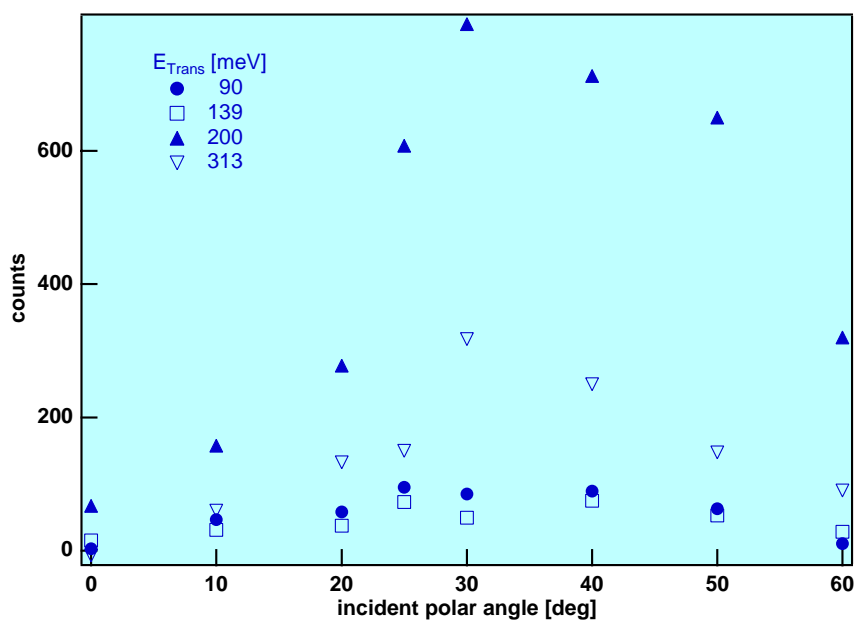


Fig. 4.9: O-atom emission as a function of incident polar angle at different molecular beam energies. The filled symbols indicate the thermal beams. The void symbols are for the hyperthermal beams ( $T=500K$ ).

detailed analysis it is necessary to resort to databases or predictive formulas. Powell and coworkers have proposed a predictive formula for the determination of IMFPs of electrons in solids, which has been tested for several materials, including aluminum [Powell, 1999]. Following their data, a value of 4.57 Å for the IMFP in aluminum has been adopted in this study. Usually elastic electron scattering cannot be neglected, and the surface sensitivity is correctly interpreted in terms of a mean escape depth (MED) [Powell, 1999]<sup>1</sup>. As far as AES of elemental solids is concerned, the probability that an electron released at a given depth in the sample leaves the latter in a given state (e.g.: without being scattered) is close to an exponential. Hence, an emission attenuation length (EAL) can be defined, that is correlated to the IMFP by the following relation

$$\lambda_{EAL} = k \cdot \lambda_{IMFP}, \quad (4.17)$$

where  $\lambda$  denotes the characteristic length. In the present case, LMM transition of Al at 68 eV,  $k=0.7$  and  $\lambda_{EAL}=3.2$  Å. The value  $D$  for the MED is given by

$$D = \lambda_{EAL} \cdot \cos \alpha \quad (4.18)$$

Eq. 4.18 has been derived for a cylindrical mirror analyzer. In the present experimental setup, Auger electrons are detected by means of a collector screen, with an acceptance angle of 120°. Integrating Eq. 4.18 over the acceptance angle, under the assumption of isotropic emission for the electrons, a value of  $D=0.48\lambda_{EAL}=1.5$  Å is obtained. Comparison of this value to the lattice constant of bulk Al at room temperature (4.05 Å), gives an idea of the surface sensitivity of the method: only 7% of the Al-LMM electrons emitted from the second layer can reach the detector without undergoing scattering processes. Even in the hypothesis of electron emission confined around the normal to the surface ( $\cos\alpha=1$ ), the mean escape depth is still 3.2 Å, and the contribution to the Auger signal by all the layers below the first one is lower than 30%.

The existence of subsurface sites for oxygen chemisorption on aluminum at sub-monolayer coverages has long been debated [Batra, 1984]. Recently, this system has been studied at room temperature by means of Negative Direct Recoil Spectroscopy (DRS). Experiments performed for coverages of 75% of the saturation have shown no subsurface oxygen within the instrumental detection limit of 2.5% [Mitrovic, 1998]. These findings support our assumption, that at the low coverage used in this work all the chemisorbed oxygen is located at the surface. Hence, the decrease in the intensity of the Auger peak at 68 eV upon exposure of aluminum to the O<sub>2</sub> beam is due to changes in the chemical composition of the first Al monolayer.

As already pointed out in Section 2.1, the sensitivity of the available Auger spectrometer is not sufficient to detect O at low coverages. On the other hand, the LMM transition for elemental Al at 68 eV produces a strong peak whose intensity is highly sensitive to contamination of the surface [Michel, 1980]. Therefore, the time evolution of the AES intensity at 68 eV was monitored while dosing the surface with O<sub>2</sub> from the molecular beam. The background pressure was usually  $2 \cdot 10^{-10}$  mbar and the rest gas analysis showed mainly contribution from mass 2 amu (H<sub>2</sub>) and mass 28 amu (most likely CO), with a contribution from mass 32 amu (O<sub>2</sub>) of  $2 \cdot 10^{-11}$  mbar. H<sub>2</sub> adsorption is hindered by

---

1. If elastic-electron scattering is neglected, the MED is equal to the IMFP times the cosine of the emission angle with respect to the surface normal.

a 1 eV barrier at room temperature [Pölzl, 1999]. CO physisorbs on Al(111) with a binding energy of 0.2 eV and desorbs at a temperature of 125 K [Chiang, 1980; Jacobi, 1989]. Therefore, only surface contamination from the background of thermal O<sub>2</sub> in the UHV chamber, whose sticking coefficient is approximately 0.01, should be of any concern. For these lengthy measurements, which could last as long as 160 minutes, the effect of adsorption from residual gases has been directly investigated. The variation of the intensity of the Al-LMM peak at 68 eV over a 160 minutes period was monitored while the molecular beam was blocked outside the UHV chamber. The intensity of the 68 eV peak remained almost constant, indicating that the surface contamination due to residual gases was negligible for time intervals comparable to the experiment duration. AES investigation of the surface before and after the experimental runs showed no traces of other contaminants. Then O<sub>2</sub> was allowed onto a freshly cleaned surface and the variation of the AES peak intensity was measured again. The results of these measurements, corrected for the absorption of O<sub>2</sub> from the background, are shown in Fig. 4.10.

The evolution of the relative intensity of the Auger peak for metallic aluminum (68 eV) with the O<sub>2</sub> exposure allowed to determine the molecular beam intensity [Section 4.4.1]. It is known from the literature, that this peak decreases linearly with increasing O<sub>2</sub> exposure until approximately one third of its original value is reached. Then, oxide nucleation starts and the slope of the signal at 68 eV reduces abruptly. The onset of a peak at 54 eV clearly marks the onset of the oxide layer growth [Gartland, 1977; Michel, 1980]. Recently, a combined STM-AES investigation demonstrated that oxidation starts at coverage values of  $\Theta_{\text{O}} \approx 0.2 \text{ ML}$  for chemisorbed oxygen [Brune, 1993]. Hence, the reduction of the AES signal to 75% of its original value after 140000 gas pulses shown in Fig. 4.10 indicates a chemisorbed oxygen coverage  $\Theta$  of 0.08 ML. The

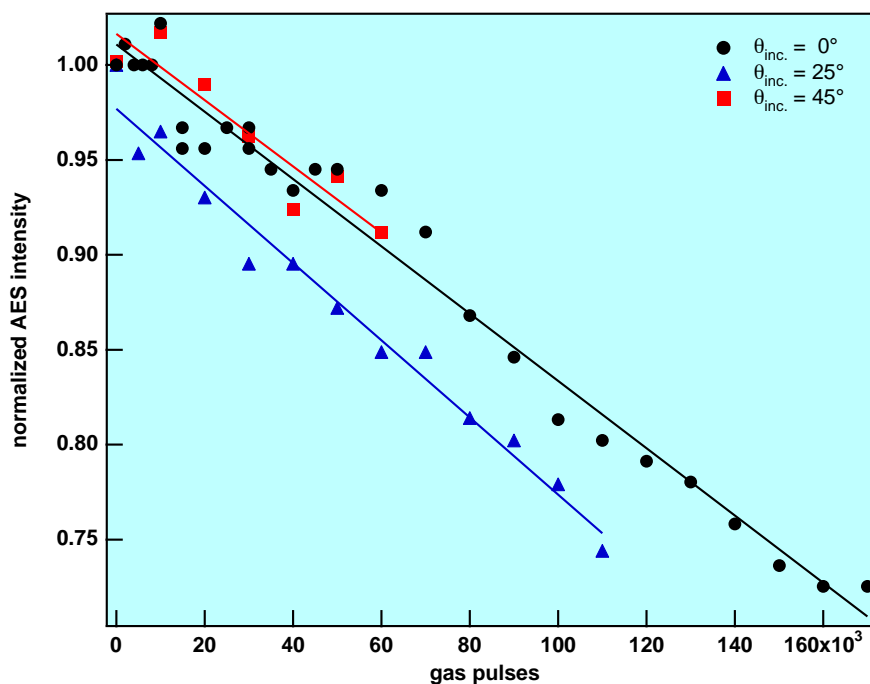


Fig. 4.10: Temporal evolution of the intensity of the Al-LMM AES peak (68 eV) as a function of the exposure to a thermal beam of O<sub>2</sub> for different incident angles ( $\theta$ ). The data are corrected for the absorption from residual gases.

solid lines are linear fits to the experimental data. The linear decrease of the intensity with the exposure indicates a constant value for the sticking coefficient at the investigated coverages. The slopes of the regression lines are a *relative* measure of the initial sticking coefficients ( $S_0^{\text{rel}}$ ) under the different  $\theta$  and are proportional to the true sticking coefficient  $S_0$ . The quantity measured within this approach is the amount of residual free aluminum sites after exposure of the sample surface to a fixed oxygen dose. For this reason  $S_0^{\text{rel}}$  has negative values. The dose is measured in molecular beam pulses. The linear decrease of the 68eV peak upon exposure of an Al(111) single crystal to a thermal molecular beam of pure O<sub>2</sub> in Fig. 4.10 supports the validity of this simple model.

This investigation was limited to chemisorption from a thermal O<sub>2</sub> beam and a limited set of geometries. More measurements would be needed to clearly understand the reason of the inconsistency with the data published by Zoric and coworkers. Nevertheless, these results show no rapid fall off for the  $S_0$  values at  $\theta_{\text{inc}} > 25^\circ$  and are consistent with our REMPI data. The measured values of  $S_0$  together with the experimental variance ( $\sigma$ ) are reported in the Table 4.5.

#### 4.4.1 The molecular beam intensity

Using the experimentally determined coverage and the *absolute* sticking coefficient known from literature, it was possible to deduce the O<sub>2</sub> dose delivered to the sample surface during each gas pulse [Österlund, 1997]. As previously discussed, the contribution to the Al-LMM AES signal from atomic layers beneath the first one is smaller than 30%. For simplicity, I will neglect this contribution altogether in the following calculation, assuming the measured intensity ( $I$ ) of the AES signal for the Al-LMM transition (68eV) from a clean aluminum surface to be proportional to the number of Al atoms present on the surface ( $n_{\text{Al}}$ ) and to a sensitivity factor ( $s_{\text{Al}}$ )

$$I = n_{\text{Al}} s_{\text{Al}}. \quad (4.18)$$

Chemisorption of O-atoms reduces the amount of free Al-atoms at the surface, causing a reduction in signal intensity, directly proportional to the oxygen coverage ( $\Theta$ )

$$\Theta = \frac{\Delta I_{\text{Al}}}{I_{\text{Al}}} \frac{3}{2} \Theta_0, \quad (4.19)$$

that is proportional to the exposure at low coverages. Here  $\Theta_0 \approx 0.2\text{ML}$  is the coverage where nucleation of Al<sub>2</sub>O<sub>3</sub> sets in. At this coverage the intensity of the 68eV AES peak

**Table 4.5: Experimental values for  $S_0^{\text{rel}}$  during the initial oxidation of Al(111) as a function of  $\theta_{\text{inc}}$**

$\theta_{\text{inc}}$ [deg]	relative $S_0$ [ $\cdot 10^{-6}$ ]	$\sigma$ [ $\cdot 10^{-6}$ ]
0	-1.77	0.05
25	-2.03	0.10
45	-1.74	0.30

was reduced by a factor of  $2/3$  with respect to its initial value [Brune, 1993]. In Eq. 4.19,  $\Theta$  represents the absolute O coverage.

Al crystallizes in a *fcc* structure with a lattice constant of  $a=4.05 \text{ \AA}$  at room temperature [Batra, 1984]. Knowing that the diameter ( $d$ ) of the molecular beam at the sample position is 3.2mm, the amount ( $N$ ) of Al free sites available to chemisorption can be determined as the ratio between the cross-sectional area of the beam and the area of the primitive unit cell spanning the (111) surface (i.e.: an equilateral triangle, whose side is  $a$ )

$$N = \frac{\pi d^2}{4} \cdot \frac{4}{\sqrt{3}a^2} = 1.13 \cdot 10^{14} \text{ sites.} \quad (4.20)$$

Hereafter, the value for the absolute initial sticking probability ( $S_0$ ) of  $O_2$  on Al measured by Österlund *et al.* will be adopted [Österlund, 1997]. The number of gas molecules,  $N(O_2)$ , delivered within one gas pulse can be derived

$$N(O_2) = \frac{N\Theta}{S_0 n} = 4.06 \cdot 10^8 \text{ mol/pulse,} \quad (4.21)$$

once the number of gas pulses  $n$  hitting the crystal is known. The density of molecules at the sample location,  $\rho(O_2)$ , in a gas pulse produced with a thermal beam of pure  $O_2$  is

$$\rho(O_2) = \frac{N(O_2)}{vt_{pulse}(\pi d^2/4)} = 4.28 \cdot 10^{14} \text{ mol/m}^3, \quad (4.22)$$

equivalent to an  $O_2$  partial pressure of  $1.63 \cdot 10^{-8}$  mbar.

#### 4.5 O-ATOMS EMISSION AS FUNCTION OF THE OXYGEN DOSE

In further experiments the O-atoms emission was investigated as a function of the surface exposure. These data were collected with the detection setup depicted in Fig. 2.9B. The signal due to the O-atoms generated in the abstraction process has been directly integrated and recorded with a computer. Its evolution with increasing exposure to  $O_2$  beam of 135, 187 and 434 meV translational energy is shown in Fig. 4.11. Each data point represents the counts accumulated in 100 laser shots. Prior to time  $t=0$  the shutter is closed and the molecular beam cannot reach the surface. The laser ran approximately for 3 min. to reach a stable power output before the measurements were started. The background was measured before and after each experimental run. The O-atom yield as a function of  $\Theta$  is displayed in Fig. 4.11 after subtraction of the average value for the background. Admittedly, these three emission diagrams are plagued by intensity fluctuation, which might be due to poor *signal-to-noise* ratio. Nevertheless, the two curves at higher translational energies present some similarities. The curve at 0.135 eV will be discussed separately.

At  $t=0$  the shutter is opened and a rise in the signal intensity is observed. The rise is not instantaneous. This is not an experimental artifact, since the detection/acquisition system does not perform any temporal averaging beyond that connected with the accumulation of one data point. Hence, the emission of O-atoms initially increases with exposure to  $O_2$ . After reaching the maximum, the O-yield decreases, rapidly approaching an intensity close to the half of its peak value. Then a slow decrease with time is observed.

At ca.  $t=800$ s the beam shutter is closed and the signal settles to its zero level. The oscillatory fine structure of the signal after the initial maximum is not reproducible.

Unlike the previous emission curves, the one measured with an  $O_2$  beam energy of 0.135eV shows fluctuation before reaching its top intensity, located approximately 200 seconds after the starting point of the measurement. Eventually the intensity decreases to reach a value close to one third of its maximum and remains constant, apart from fluctuation around this mean value, till the end of the measurement. The emission intensity is lower than the one measured at higher  $O_2$  translational energies. Both the reduced emission intensity and the absence of a clear decrease after prolonged exposure might result from the reduced sticking coefficient at lower kinetic energy.

#### 4.6 O-ATOMS YIELD AS FUNCTION OF $E_{\text{TRANS}}$ OF THE MOLECULAR BEAM

It is known that dissociative chemisorption of  $O_2$  on Al(111) surfaces is an activated process, exhibiting a strong dependence on the translational energy of the incoming molecules [Österlund, 1997]. Therefore, I investigated the dependence of the O-atom yield on the beam energy. The REMPI signal due to the recoiled O-atoms has been either acquired with a multichannel scaler or using boxcar averagers. Eventually, it was stored on a computer [Fig. 2.9A or Fig. 2.9B, respectively]. The beam energy was varied by seeding  $O_2$  in He, by heating the nozzle or by a combination of both methods. The molecular beam translational energies are reported in Table 2.1. The laser power was 2.5 mJ/pulse, as measured at the laser output port, and the beam was focused 10 mm away from the surface, along its normal. The O-atom yield, defined as the ratio of the accumulated O-atom counts to the number of gas pulses, is shown in Fig. 4.12 as a function of the beam energy. The vertical error bars show the standard deviation of the mea-

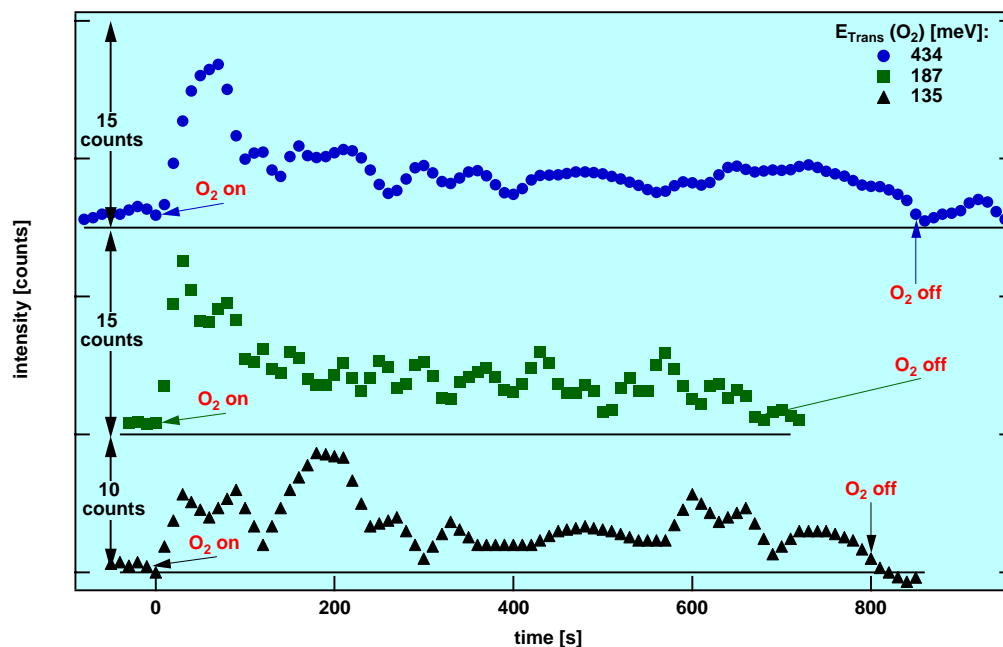


Fig. 4.11: O-atom emission as a function of the  $O_2$  dose, for different translational energy of the incident  $O_2$  beam. At  $t=0$  s the beam shutter was opened. After ca. 800s the shutter was closed again. Each data point represents the number of ions accumulated in 100 laser pulses.

sured yield and represent the reproducibility of the experiment. The horizontal error bars represent the uncertainty on the beam energy. The data presented here are measured at coverages  $\Theta < 0.01 \text{ ML}$  and are representative of the initial stage of the chemisorption process. In Fig. 4.12, neither  $\text{O}_2$  dilution due to seeding nor flux variations due to different molecular velocities are taken into account. For this reason, no clear dependency of the O-atom yield on the translational energy is visible.

The abstraction reaction can be modeled as a process where a flux  $J(\text{O}_2)$  of incoming  $\text{O}_2$  molecules interacts with an Al(111) surface and originates a flux of outgoing O-atoms,  $J(\text{O})$ . These two fluxes are linked by an abstraction coefficient  $\sigma_{\text{ab}}$ , which describes the probability of the actual reaction.  $\sigma_{\text{ab}}$  can be a complicated function of several quantities, characterizing both the incoming  $\text{O}_2$  molecules (translational, vibrational and rotational energies) and the substrate (temperature, crystal faces, steps and defects densities, etc.). The goal of this section is to determine  $\sigma_{\text{ab}}$  as a function of the energy of the incoming molecules, starting from the measured O-yield. The abstraction reaction can be written as

$$J(\text{O}) = \sigma_{\text{ab}} J(\text{O}_2). \quad (4.23)$$

To simplify the problem, I concentrated onto the case of Al(111) oxidation at room temperature. Since it is known from the literature that  $S_0$  is independent from the surface temperature, this limitation should not impair the ability to grasp the basic characteristics of the process [Österlund, 1997].

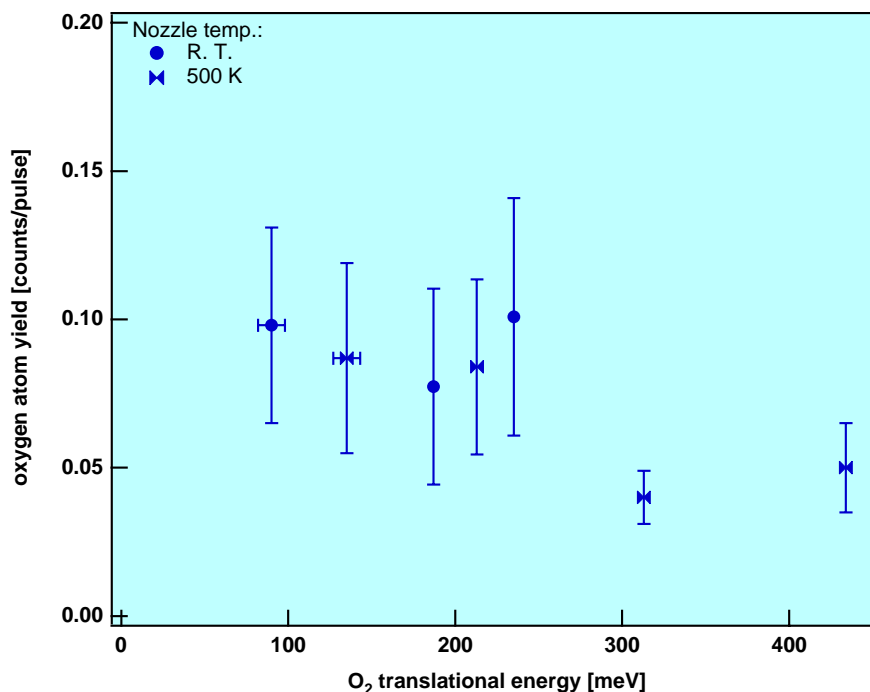


Fig. 4.12: Experimental values of O-atom yield as function of the beam translational energy. The vertical error bars represent the variance of the experimental data. The horizontal error bar shows the uncertainty affecting the beam energy. The displayed data are corrected neither for the  $\text{O}_2$  dilution due to seeding, nor for the effect of different molecular velocities.

$J(\text{O}_2)$  is the flux of incoming molecules hitting the metal surface at the given experimental conditions. It is characteristic for the molecular beam and depends on the stagnation pressure ( $P_0$ , the pressure in the gas reservoir before the nozzle), the seeding conditions ( $S_\alpha$ ),  $\beta$  (a form factor due to the divergency of the beam) and  $v_{\text{O}_2}(T_{\text{Nozzle}}, S_\alpha)$  the velocity of the  $\text{O}_2$  molecules in the beam due to the nozzle temperature and the seeding. In our setup, gas expansion always starts from the poppet valve, that constitutes a reservoir at  $P_0$  and  $T_0$ . This implies that the number of expanding molecules for each gas pulse is constant for a given  $P_0$ . Heating takes place when the gas flows through the capillary and the final gas temperature affects neither the pressure nor the density of the gas before expansion. As a consequence of this peculiarity of the present setup,  $J(\text{O}_2)$  will only depend on the velocity of the  $\text{O}_2$  molecules in the beam and, of course, on  $S_\alpha$  and  $P_0$ . Since  $v_{\text{O}_2}$  affects the geometrical length of the gas pulses, its effect will be to dilute the number of expanding molecules into bigger or smaller volumes, according to the higher or lower molecular velocity. Therefore,  $J(\text{O}_2)$  can be defined as

$$J(\text{O}_2) = \frac{P_0 S_\alpha \beta}{v_{\text{O}_2}(T_{\text{Nozzle}}, S_\alpha)}. \quad (4.24)$$

$P_0 S_\alpha \beta$  is the  $\text{O}_2$  partial pressure at the sample location. It has been experimentally determined with the procedure illustrated in Section 4.4.1.

Based on Eq. 4.24, it is possible to rescale the experimental data displayed in Fig. 4.12, to account for the actual flux of  $\text{O}_2$  molecules in the beam. The result is shown in Fig. 4.13.

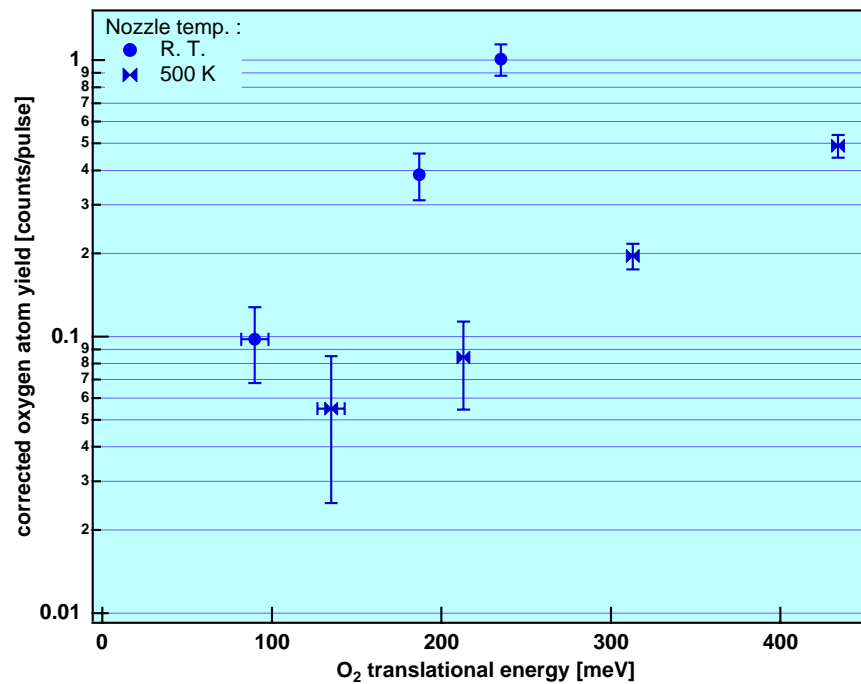


Fig. 4.13:  $\text{O}$ -atom yield as function of the beam translational energy. The displayed data are corrected for the  $\text{O}_2$  dilution due to seeding, and for the effect of different molecular velocities. Error bars as in Fig. 4.12.

The velocity of the species investigated by means of REMPI is such, that their drift within the duration of the probing laser pulse is negligible. Hence, REMPI samples the local density of that species in a defined quantum state, not the flux.

$J(O)$  is a diverging flux of outgoing O-atoms, originating from the sample and crossing the section of the laser active volume ( $V_L^{act}$ ), located 10mm away from the metal surface. Hence, the O-atoms ionized and detected are only a fraction of the O-atoms actually emitted during the oxidation process. With reference to the discussion in Section 2.1, let us call  $I$  the amount of ions detected within a laser pulse and  $n_{O-atoms}$  the number density of O-atoms in the probe volume. These two quantities are linked by the following equation

$$I = n_{O-atoms} S, \quad (4.25)$$

where  $S$  is the detection efficiency of the REMPI-ToF spectrometer. All the information about the physics of the detection process is enclosed in  $S$ . It will be examined in more detail in Section 4.6.1. The flux of O-atoms will be

$$J(O) = (n_{O-atoms} S) / v_O, \quad (4.26)$$

with  $v_O$  being the velocity of the O-atoms. Once the intensity of the molecular beam and the overall cross-section for (2+1)REMPI of O-atoms are known, it is possible to extract the abstraction probability from the measured yield. Alternatively, the same result could be obtained with a calibration of the sensitivity of the REMPI-ToF spectrometer. In Section 4.6.1, these two complementary approaches will be described.

#### 4.6.1 Probability for the abstraction reaction

A calibration of the REMPI-ToF spectrometer was needed to deduce the total amount of O-atoms released during the oxidation process, starting from the experimental O-atom yield. Then, the abstraction probability was determined as the ratio of the released O-atom to the incoming  $O_2$  molecules.

$NO_2$  photodissociation at 225.65nm was used to produce atomic oxygen and the intensity of the  $O(0,1,2 \leftarrow 2)$  transition was measured at different  $NO_2$  pressures. These measurements were performed either in the HV setup or in the UHV apparatus, according to the pressure range investigated. In both cases, the laser pulses were focused using 250mm focal length lenses. The laser power at the focus was 0.9mJ, after correction for transmission losses.

Laser beams show gaussian irradiance profile, and do not follow the usual law of geometrical optics. Hereafter, the focal volume of the laser will be explicitly calculated, following the method originally introduced by Self and successively integrated by Sun [Self, 1983; Sun, 1998].<sup>1</sup> In the following, the contour of the beam will be supposed circular and the radii  $w$  will be defined as radii of the  $1/e^2$  irradiance contour of the beam. As shown in Fig. 4.14, a focusing lens of focal length  $f$  reduces the spot radius  $w_s$  of an incoming laser beam, to a spot of radius  $w_0$  in the rear focal plane.  $w_0$  is defined as

---

1. A simple introduction to this topic can also be found in the 2<sup>nd</sup> chapter of the Melles Griot catalogue, or under the internet address: <http://www.mellesgriot.com/products/optics/ch2-00.htm>.

$$w_0 = \frac{f\lambda}{\pi w_s} M^2. \quad (4.27)$$

$M^2$  is a quality factor, to account for deviations of real lasers from a truly Gaussian profile:  $M^2=1$  for a theoretical Gaussian source;  $M^2>1$  for a real laser. This factor is usually about 2 for dye lasers, but it might reach values of 3 or 4 for high intensity, multimode lasers. The profile of the beam at the output port of the dye laser is approximated with a circular spot of 1.2mm of radius. The calculated focal length of the lens is 21.97cm at the wavelength of 225.65nm. Under these conditions, a value of 26.3 $\mu\text{m}$  for the waist of focused laser beam is found. The *Rayleigh range* or *confocal parameter*,  $z_R$ , is the distance over which the beam radius increases by a factor  $\sqrt{2}$ . It is defined as

$$z_R = \frac{\pi w_0^2}{\lambda}, \quad (4.28)$$

and its calculated value is 9.6mm. The value  $w_R$  for the beam radius at  $z_R$  is 37.2 $\mu\text{m}$ . Referring to the diagram in Fig. 4.14, I assume that ionization only takes place in the volume delimited by  $w_0$  and the two  $w_R$  symmetrically located at  $w_0 \pm z_R$ . Then the ionization volume  $V_{\text{ion}}$  can be calculated as twice the volume of the frustum with bases  $w_R$  and  $w_0$  and height  $z_R$

$$V_{\text{ion}} = \frac{2\pi}{3} z_R (w_0^2 + w_0 w_R + w_R^2). \quad (4.29)$$

This volume corresponds to 6.16 $\cdot 10^{-5}$  cm<sup>3</sup>.

To determine the sensitivity of the REMPI-ToF spectrometer, the number of O atoms detected in each laser pulse must be associated to the number of O atoms present in  $V_{\text{ion}}$ .

The ion gauge read-out (P) has been calibrated against N<sub>2</sub> and the measured partial pressure has been corrected for the ratio of the Electron-Impact Ionization Cross Sections of NO<sub>2</sub>/N<sub>2</sub> ( $\rho=1.47$  according to the NIST Database). This allowed to estimate the partial pressure of NO<sub>2</sub> present in the vessels during the measurement. At the photon energies available in the present experimental setup, NO<sub>2</sub> photodissociation is a one pho-

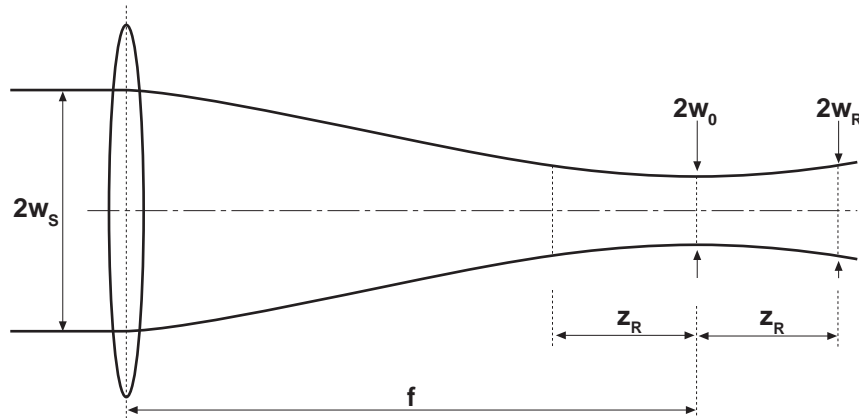


Fig. 4.14: Concentration of a laser beam by a focusing lens of focal length  $f$ .  $w_s$  is the radius of the  $1/e^2$  irradiance contour of the source beam,  $w_0$  is the beam waist,  $z_R$  is the Rayleigh range and  $w_R$  is the beam diameter at that length.

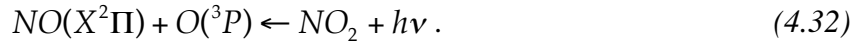
ton process, with a cross-section  $\sigma_{ph}$  of  $3.095 \cdot 10^{-19} \text{ cm}^2$  [Bass, 1976].  $\Phi$  is defined as the flux of photons through a surface normal to the direction of propagation of the light beam normalized to the surface area and can be calculated as

$$\Phi = P_{energy} \frac{\lambda}{1.2397 \cdot 10^{-6}} \frac{1}{\pi w^2}, \quad (4.30)$$

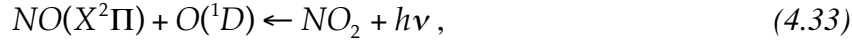
where  $P_{energy}$  is the laser pulse energy expressed in Joule,  $\lambda$  is the laser wavelength expressed in m, and  $w$  is the radius of the laser beam. The value of  $\Phi$  is a function of the laser beam radius. Its values at the location of the focused beam waist and of the confocal parameter are, respectively,  $4.7 \cdot 10^{19} \text{ photons} \cdot \text{cm}^{-2}$  and  $2.4 \cdot 10^{19} \text{ photons} \cdot \text{cm}^{-2}$ . The photodissociation probability per second is

$$\eta_{ph} = \frac{dP(NO + O \leftarrow NO_2 + h\nu)}{dt} = \sigma_{ph} \Phi. \quad (4.31)$$

Assuming the mean value of  $3.5 \cdot 10^{19} \text{ photons} \cdot \text{cm}^{-2}$  for the laser fluence, the photodissociation probability assumes a value of 10.83, showing that all of the  $NO_2$  molecules present in the laser volume are dissociated. As already mentioned in Section 3.2,  $NO_2$  is known to photodissociate with a quantum efficiency  $\eta(^3P)$  of 0.97 at wavelengths shorter than 313.0nm, following the reaction pathway



At wavelengths shorter than 244nm, a competitive photodissociation channel is open



whose quantum efficiency  $\eta(^1D)$  rapidly increases with photon energy. From a compilation of the data available in the literature, a linear correlation between the quantum efficiency of the reaction channel in Eq. 4.33 and the wavelength of the incident laser light can be extrapolated [Richter, 2000; Uselman, 1976]. This allows to estimate the branching ratios  $\eta(^3P)=0.46$  and  $\eta(^1D)=0.54$  respectively, for the processes in Eq.4.32 and Eq. 4.33.

Integrating the area under the O-peaks in Fig. 3.2, it is possible to estimate the branching ratios  $\beta(^3P_i)$  for the occupation of each of the single states composing the  $^3P$  multiplet, after photodissociation. The  $O(^3P_2)$  state accounts for 58% of the overall  $O(^3P_j)$  population. Hence, a value of 0.58 for  $\beta(^3P_2)$  can be deduced. An expression can be written, linking the partial pressure of  $O(^3P_2)$  in the laser focus,  $P(O(^3P_2))$  to the  $NO_2$

**Table 4.6: Quantum efficiency  $\eta(^3P)$  for  $O(^3P)$  production upon  $NO_2$  photodissociation in the UV region.**

wavelength [nm]	$\eta$	Reference
244	threshold	Calvert, 1966
228.8	0.48	Uselman, 1976
212.8	$1 \div 0.7$	Richter, 2000

pressure ( $P$ ), the quantum efficiency of the photodissociation process  $\eta_{\text{ph}}$  and the branching ratios for the production of O atoms in the low-lying state of the  $^3\text{P}$  triplet  $\eta(^3\text{P})$  and  $\beta(^3\text{P}_2)$

$$P(O(^3\text{P}_2)) = P\eta_{\text{ph}}\eta(^3\text{P})\beta(^3\text{P}_2). \quad (4.34)$$

The number of ions measured at a given laser wavelength is proportional to the partial pressure of O-atoms in the corresponding quantum state. Fitting the measured points to a linear function and imposing that the number of detected ions vanishes at vanishing pressures, the following relation is obtained between the ion counts and the O-partial pressure expressed in mbar

$$I = a \cdot P(O(^3\text{P}_2)), \quad (4.35)$$

where the linear coefficient  $a = (1.18 \pm 0.11) \cdot 10^8$ . The results of the calibration measurements are shown in Fig. 4.15, together with the linear fit. Since the calibration procedure has been performed against a background pressure of  $\text{NO}_2$ , in *static* conditions, it was natural to perform the calculation in terms of the partial pressure of the detected O-atoms. Nevertheless, it must be noticed that the partial pressure is directly proportional to the number density of O-atoms ( $n_{\text{O-atoms}}$ ) in Eq. 4.25. Since  $n_{\text{O-atoms}}$  is linked to the flux of O-atoms  $J(\text{O})$  through Eq. 4.26, the formulation in terms of fluxes, densities or partial pressures are completely equivalent.

When a gas pulse hits the surface, a fraction of the incident molecules dissociates emitting neutral fragments in the vacuum. Although O-atoms are highly reactive, at the experimental condition they could not recombine, since their mean free path is ca.  $10^3$  m. The focus of the laser beam was placed 10 mm away from the sample surface and ca. 20 mm away from the entrance of the field-free region of the ToF spectrometer. A fraction of the atoms drifting away from the surface, was ionized at the laser focus. These

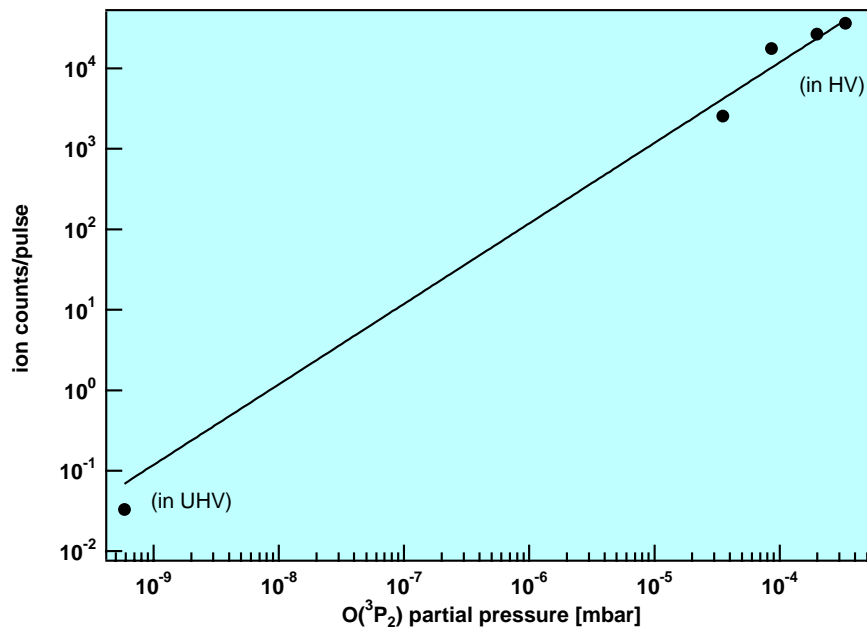


Fig. 4.15: Calibration diagram of the REMPI-ToF sensitivity.

ions were steered through the ToF spectrometer and eventually detected at the MCP's (cf. Fig. 2.3). It is now possible to determine the flux of O-atoms emitted during the interaction between the gas pulse and the surface, as a function of the detected O-ions. The ratio of the O-atoms flux to the incoming O<sub>2</sub> flux, determines the abstraction probability ( $\sigma_{ab}$ ) according to the following equation

$$\sigma_{ab} = \frac{J(O(^3P_2))}{J(O_2)} = \frac{I}{av_O} \frac{v_{O_2}}{P_0 S_\alpha \beta}. \quad (4.36)$$

These values of  $\sigma_{ab}$  are listed in Table 4.7.

Alternatively, the measured ion counts  $I$  can be expressed as

$$I = n_{O-atoms} \sigma^{(2)} \Phi^2 \sigma_{pi} \Phi V_L^{act} \Sigma, \quad (4.37)$$

when the laser is tuned to the center of the resonance frequency. Here  $\Phi$  is the already defined laser fluence. Because of the focusing lens, the beam diameter was not constant along the direction of propagation of the light. Therefore,  $\Phi$  was also dependent on the distance from the laser focus along the same direction.  $V_L^{act}$  is the active laser volume, i.e. the volume occupied by the focused laser beam and delimited by the acceptance angle of the *Time-of-Flight* tube (see Fig. 4.16). The active laser volume was calculated by numerical integration of an equation derived applying the procedure of Self corrected for the non-ideality of the laser profile, assuming a spherical gaussian beam profile for the laser [Self, 1983; Sun, 1998]. The variation of  $\Phi$  along the direction of propagation of the light, has been accounted for in this calculation.  $n_{O-atoms}$  is the number density of O atoms in the detection volume, already defined in Eq. 4.25.  $\Sigma$  is the detection efficiency of the spectrometer, already described in Section 2.1. Eq. 4.25 is similar to eq. 4.37, the only difference being that the dependences of the efficiency on the experimental parameters are now explicit.  $n_{O-atoms}$  represents the fraction of incident molecules, which chemisorbed abstractively. It is connected to the number density of incident molecules through the abstraction probability ( $\sigma_{ab}$ )

$$n_{O-atoms} = N(O_2) \sigma_{ab}. \quad (4.38)$$

**Table 4.7:**  $\sigma_{ab}$  during the initial stage of Al(111) oxidation as function of  $E_{trans}$  [Eq.4.36]

$E_{trans}$ [meV]	$\sigma_{ab}$	Variance [%]
90	0.033	30.5
135	0.023	66.7
187	0.190	27.6
213	0.044	56.8
235	0.556	20.8
313	0.125	20.0
434	0.367	21.1

$\sigma^{(2)} = (2.66 \pm 0.80) \cdot 10^{-35} \text{cm}^4$  is the two-photon absorption cross section for the resonant excitation of O-atoms.  $\sigma_{\text{pi}} = (5.3 \pm 2.0) \cdot 10^{-19} \text{cm}^2$  is the photoionization cross section. Their values are known from the literature, for laser intensities of  $1.6 \text{ MW/cm}^2$  [Bamford, 1986]. As pointed out by Bamford *et al.*, at the intensities commonly used in REMPI experiments (approximately  $3 \cdot 10^4 \text{ MW/cm}^2$  in the present case), the two-photon absorption process should be saturated and the rate equations approach for the determination of the cross sections might no longer be valid. In this case, a complete density-matrix analysis should be performed. Moreover, the effect of ac Stark shifts and *above threshold ionization* (ATI) onto the overall ionization cross-section might become relevant [Bamford, 1986]. Indeed, the slopes of the linear fits to the data shown in Fig. 4.4 are lower than the theoretical values expected for 3-photon and 5-photon processes. This indicates a partial saturation of the processes involved in the overall photoionization reaction. As far as ac Stark shifts and ATI are concerned, the following critical analysis shows that both ac Stark shifts and ATI should not influence the sensitivity of this experimental setup.

According to the Floquet theorem, the wavefunction describing an atom in an intense, monochromatic, electromagnetic field, can be written as

$$\Psi(\mathbf{r}, t) = \exp(-iE_a t) \varphi(\mathbf{r}, t), \quad (4.39)$$

where  $E_a$  represents the initial nondegenerate state and  $\varphi(\mathbf{r}, t) = \varphi(\mathbf{r}, t + 2\pi / \omega)$  is the periodic function which describes the external field.  $\varphi$  can be expanded in a Fourier series in time, so that

$$\Psi(\mathbf{r}, t) = \exp(-iE_a t) \sum_{k=-\infty}^{k=\infty} C_k(\mathbf{r}) \exp(-ik\omega t). \quad (4.40)$$

The wave function can be seen as the superposition of a number of stationary states, called *quasi-energy states*, whose energies are  $E_a + k\omega$ . In a real system, the number of *quasi-energies*  $E_a$  equals the number of its unperturbed states. The set of values of  $E_a + k\omega$  constitutes the *spectrum of quasi-harmonics* [Zel'dovich, 1973], that is the spectrum of the quantum state 'atom+field' (the so called: dressed atom). In this experiment, I am dealing with O atoms in their ground state and the frequency of the transition  $O(3p^3P_0) \leftarrow O(2p^3P_{j'})$  is twice the frequency of the laser light involved. This means that

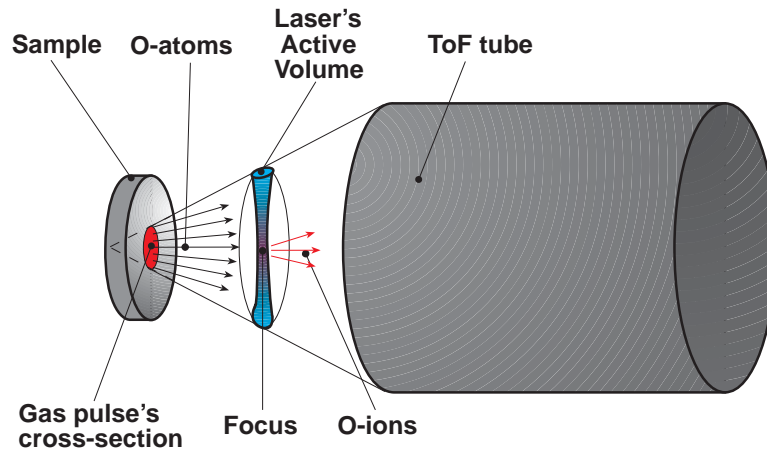


Fig. 4.16: Schematic view of the active volume of the laser.

the radiation field is *low-frequency* and only the ground state will be affected by the incoming radiation. Hence, this system behaves as if it were a one-level atom. In this case, the effect of the external field is reduced to an ac Stark shift of that atomic level [Delone, 1999]. This does not affect the detection efficiency of the setup, because the laser wavelength was calibrated optimizing the O-ion yield and the ac Stark shift was automatically compensated.

Above Threshold Ionization (ATI) is a phenomenon observed in multiphoton ionization experiments in intense laser fields. This process is characterized by a large number of evenly spaced peaks in the photoelectron energy spectrum. These peaks correspond to the absorption of  $n+s$  photons by an atom which requires only  $n$  photons to ionize. The special feature of ATI, which distinguishes it from other multiphoton ionization processes, is the significant number of radiative transitions between continuum states of the atom. However, if ATI were active, ionization processes involving more than 3 photons should be observed. This would raise the power dependency of the ionization signal from the laser fluence above the value of 3, characteristic of the (2+1) process. As shown in Fig. 4.4, O-photoionization is a 3-photon process over the whole range of laser intensities available for these experiments and no ATI process seems to be active.

Although neither ac Stark shifts nor ATI seem to be relevant in the present experimental conditions, the values for  $\sigma^{(2)}$  and  $\sigma_{pi}$  given in the literature should be taken with some care, because of the above mentioned saturation effects and the consequent possible breakdown of the rate equation approach.

The intensity  $I$  of the REMPI signal is proportional to the number density of the O-atoms, because REMPI samples the *density* of the outcoming atoms [Section 4.3]. To connect  $I$  to the *fluxes* of incoming molecules and outcoming atoms, both of the velocities,  $v_{O_2}$  and  $v_O$ , must be taken into account. This leads to the following expression for the intensity

$$I = N(O_2)\sigma_{ab} \frac{v_{O_2}}{v_O} \sigma^{(2)} \Phi^2 \sigma_{pi} \Phi V_L^{act} \Sigma, \quad (4.41)$$

**Table 4.8:**  $\sigma_{ab}$  during the initial stage of Al(111) oxidation as function of  $E_{trans}$  [Eq.4.42]

$E_{trans}$ [meV]	$\sigma_{ab}$	Variance [%]
90	0.022	30.5
135	0.020	66.7
187	0.088	27.6
213	0.019	56.8
235	0.229	20.8
313	0.046	20.0
434	0.111	21.1

where  $\Sigma$ , the estimated value for the detection efficiency of the ToF spectrometer, is approximately 0.8 [Section 2.1]. Finally, an expression for  $\sigma_{ab}$  can be derived,

$$\sigma_{ab} = \frac{I}{N(O_2)\sigma^{(2)}\Phi^2\sigma_{pi}\Phi V_L^{act}\Sigma} \frac{v_O}{v_{O_2}}, \quad (4.42)$$

which depends only on experimental quantities and constants known from the literature and  $\sigma_{ab}$  can be calculated from the experimental data.

The values in Table 4.8 are between 30% and 60% smaller than the one reported in Table 4.7. This discrepancy has to be ascribed to the different methods chosen for the evaluation of the experimental data. But since the difference between the two sets of values is comparable with their experimental variance, I can conclude that the two approaches are consistent with each other. From a different point of view, this result indicates that the accuracy characterizing these measurements is, approximately, one order of magnitude.

#### 4.6.2 About the experimental uncertainty

The errors affecting the measurement of each single experimental parameter combine randomly, to determine the experimental uncertainty affecting the measurement of the abstraction probability. Assuming that all those errors are gaussian in nature, the effect of their propagation can be easily calculated applying the following rules:

$$\frac{\delta(xy)}{xy} = \frac{\delta(x/y)}{x/y} = \sqrt{(\delta x/x)^2 + (\delta y/y)^2} \quad (4.43)$$

and

$$\delta(x^n)/x^n = n(\delta x/x), \quad (4.44)$$

where  $\delta(x)/x$  is the relative error for a given parameter [Capiluppi, 1978]. Applying these rules to Eq. 4.42, I obtain the following expression for the relative error on  $\sigma_{ab}$ :

$$\frac{\delta(\sigma_{ab})}{\sigma_{ab}} = \sqrt{\left(\frac{\delta(I)}{I}\right)^2 + \dots + \left(\frac{\delta(\Sigma)}{\Sigma}\right)^2} + \sqrt{3\left(\frac{\delta(\Phi)}{\Phi}\right)^2}. \quad (4.45)$$

The experimental uncertainties involved in the calculation of the relative error for  $\sigma_{ab}$  are listed in Table 4.9. As far as  $\delta(I)/I$  is concerned, the biggest value among the experimental variances on the measured intensity has been used. The value of  $\sigma_{ab}$  results affected by a relative error of  $\pm 80\%$ .

Applying the same kind of analysis to Eq. 4.35 and Eq. 4.36, I obtain

**Table 4.9: Uncertainty of the experimental parameters affecting  $\sigma_{ab}$  [Eq. 4.45]**

$\frac{\delta(I)}{I}$	$\frac{\delta(v_O)}{v_O}$	$\frac{\delta(v_{O_2})}{v_{O_2}}$	$\frac{\delta(N(O_2))}{N(O_2)}$	$\frac{\delta(\sigma^{(2)})}{\sigma^{(2)}}$	$\frac{\delta(\sigma_{pi})}{\sigma_{pi}}$	$\frac{\delta(\Phi)}{\Phi}$	$\frac{\delta(V_L^{act})}{V_L^{act}}$	$\frac{\delta(\Sigma)}{\Sigma}$
60%	7%	5%	5%	30%	38%	10%	5%	5%

**Table 4.10: Uncertainty of the experimental parameters affecting  $\sigma_{ab}$  [Eq. 4.46]**

$\delta(I)/I$	$\delta(a)/a$	$\delta(P)/P$
60%	9%	5%

$$\frac{\delta(\sigma_{ab})}{\sigma_{ab}} = \sqrt{\left(\frac{\delta(I)}{I}\right)^2 + \left(\frac{\delta(a)}{a}\right)^2 + \left(\frac{\delta(P)}{P}\right)^2}. \quad (4.46)$$

In this case, the experimental uncertainties affecting the calculation of  $\delta(\sigma_{ab})/\sigma_{ab}$  are listed in Table 4.10. The estimated value of the relative error is approximately 60%, substantially coincident with the experimental variance.

Considering the simplicity of the underlying model, the lower uncertainties affecting its results and the possible problems concerning the use of  $\sigma^{(2)}$  and  $\sigma_{pi}$  given in the literature, the set of values in Table 4.7 will be used in the following discussion.

Fig. 4.17 shows  $\sigma_{ab}$  as a function of the beam translational energy. The vertical error bar represents the uncertainty affecting the determination of the abstraction coefficient. The horizontal error bar shows the uncertainty on the beam energy. The nozzle temperatures are also indicated. The measured values of  $\sigma_{ab}$  are generally lower than the values of  $S_0$  at the same energies. This is reasonable, since abstraction is only one of the two

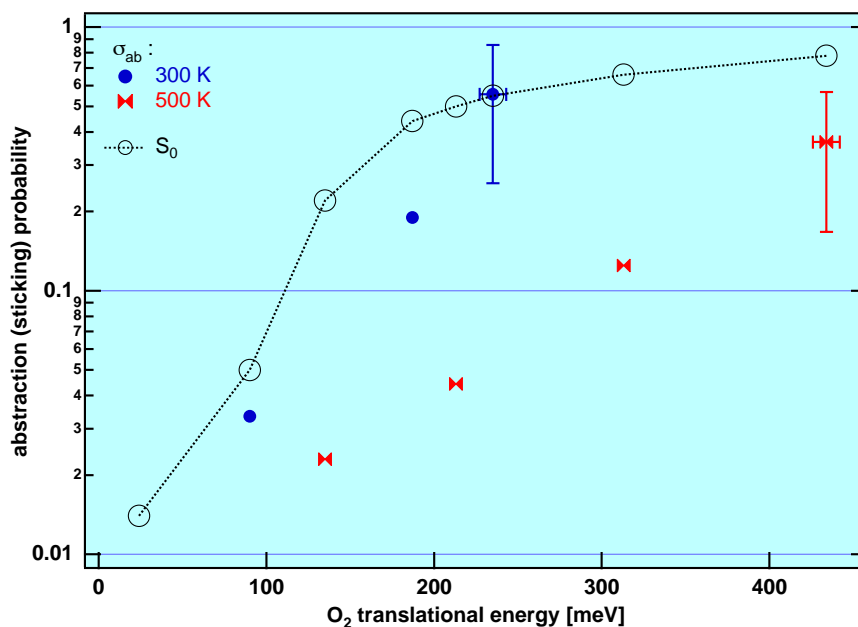


Fig. 4.17: The filled symbols show the values of abstraction coefficient ( $\sigma_{ab}$ ) as a function of the translational energy of the incident molecules. The error bars show the convolution of the variance with the estimated uncertainty (vertical) and the accuracy on the beam energy measure (horizontal). The value of the initial sticking coefficient (void circles), from the work of Österlund et al., is shown as a reference [Österlund, 1997].

reaction channels open for dissociative chemisorption for hyperthermal incident  $O_2$ . The measured value of  $\sigma_{ab}$  at  $E_{\text{trans}}(O_2)=235\text{ meV}$  is slightly higher than the corresponding value for  $S_0$ , but their difference is within the experimental accuracy of the REMPI method. Therefore, it can be concluded, that the determination of  $\sigma_{ab}$  in this work is consistent with the  $S_0$  measurement performed by Österlund and coworkers.

## 5. DISCUSSION

The laser spectrometric data presented in the preceding chapter constitute a direct evidence for the ejection of O-atoms during the reactive scattering of an  $O_2$  molecular beam with an Al surface. In Section 4.2 it is shown, that the different dependency on the laser power allows to unambiguously assign one of the two components in the REMPI ToF of Fig. 4.3 to O-atoms produced upon  $O_2$  photodissociation, the other one to O-atoms present as such in the laser ionization volume. The present work constitutes the first direct experimental evidence for the existence of an abstraction pathway in the dissociative chemisorption of  $O_2$  on Al, proving an hypothesis originally proposed by Wahnström *et al.* [Wahnström, 1996] in order to rationalize the STM findings of Brune and coworkers [Brune, 1992].

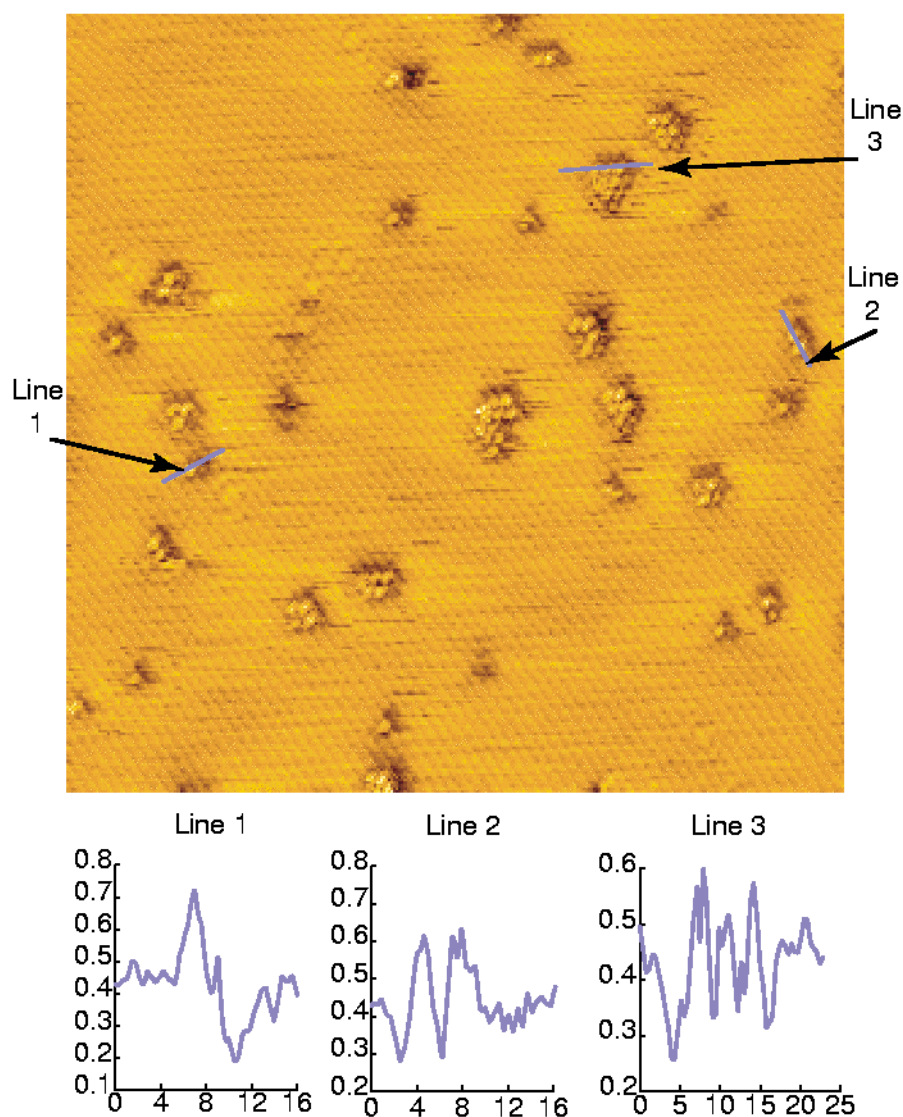


Fig. 5.1: STM image of Al(111) exposed to  $O_2$  from a 0.5 eV molecular beam (imaged area  $200 \times 200 \text{ \AA}^2$ ;  $I_t = 90 \text{ nA}$ ,  $V_t = -0.2 \text{ V}$ ). The three line traces are drawn through O-Al reacted sites and plotted, topographic height [Å] vs. distance [Å]: line 1, across a single oxygen adatom site; line 2, across a paired site; line 3, across a large oxygen island [Binetti, 2000].

The REMPI results are also complementary with the STM data of Komrowski and Kummel. They studied the chemisorption of oxygen on Al(111) at room temperature, exposing clean metal surfaces to  $O_2$  from a 0.5 eV molecular beam, to thermal  $O_2$  from the background or to O atoms from an effusive source [Binetti,2000; Komrowski,2000]. Fig. 5.1 shows the metal surface after exposure to the hyperthermal molecular beam. Oxygen monomers, dimers and larger islands can be recognized in this picture. This proves that STM images produced by single chemisorbed atoms can be distinguished from the images produced by dimers and bigger islands. To double-check this conclusion, the aluminum surface was also exposed to an effusive beam of O atoms, produced by a plasma source. Since the source produced O-atoms with an efficiency close to 50%, the surface was actually exposed to a mixed flux of O and  $O_2$ . However, O-atoms are expected to stick to the surface with a probability equal to one, while the sticking probability of  $O_2$  is two orders of magnitude lower. Therefore, the effect of the  $O_2$  impurities can be safely neglected. A close-up of two single O-atoms chemisorbed upon exposure of the surface to the beam from the plasma source is shown in Fig. 5.2. The small apexes in the middle of the depressions, shown in the lines 1 and 2, have previously been

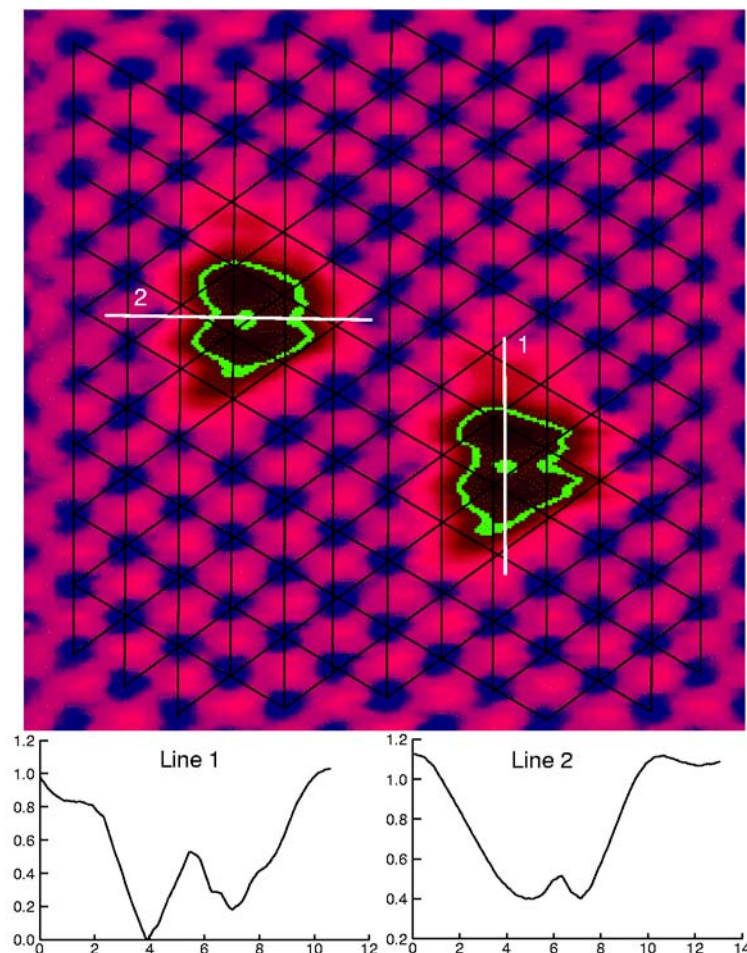


Fig. 5.2: STM image of Al(111) exposed to O from an effusive beam (imaged area  $35 \times 35 \text{ \AA}^2$ ;  $I_t = 70 \text{ nA}$ ,  $V_t = -0.8 \text{ V}$ ). The two line traces are drawn across single O adatoms and plotted, topographic height [Å] vs. distance [Å]. The hexagonal structure of the substrate is clearly visible [Komrowski,2000].

assigned to oxygen adatoms [Wintterlin,1996]. Experimentally, it is seen that changing the tunneling conditions or the tip morphology can increase the height of the oxygen apex. It is interesting to note that none of the apices imaged in this picture is situated directly at a three-fold hollow site nor at an atop site. However, STM images have conclusively shown, that the oxygen apices within larger islands of chemisorbed oxygen do reside at fcc three-fold hollow sites [Trost,1998]. It is possible that the low coverage intermediate position of the single chemisorbed oxygen apex is due to a local substrate lattice re-arrangement, to asymmetric electronic orbital interference in the tip-adsorbate interaction or to a combination of both of them [Yourdshahyan,2001, Henkelman,2001]. The different appearances of line 1 and line 2 sites may be due to occupation of nearly degenerate adsorption sites on the Al(111) surface: similar effects have been reported for other metals [Schintke,2001; Carlisle,2000]. Since exposure of the sample to atomic oxygen produced no new STM feature with respect to those already identified in Fig. 5.1, the single protrusions were positively identified as single O adatoms.

Recently, this interpretation has been questioned by Schmid and coworkers, who used a variable temperature STM (vT-STM) to investigate the initial stage of O<sub>2</sub> chemisorption on the (111) face of aluminum in the temperature range between 80K and 300K [Leonardelli,2000; Schmid,2001]. In Fig. 5.3, the image of an Al(111) surface at 80K is shown. It was taken after exposing the surface to O<sub>2</sub> from the background, at 150K. The pairs of O-atoms are labelled with their O-O distance in multiples of the nearest neigh-

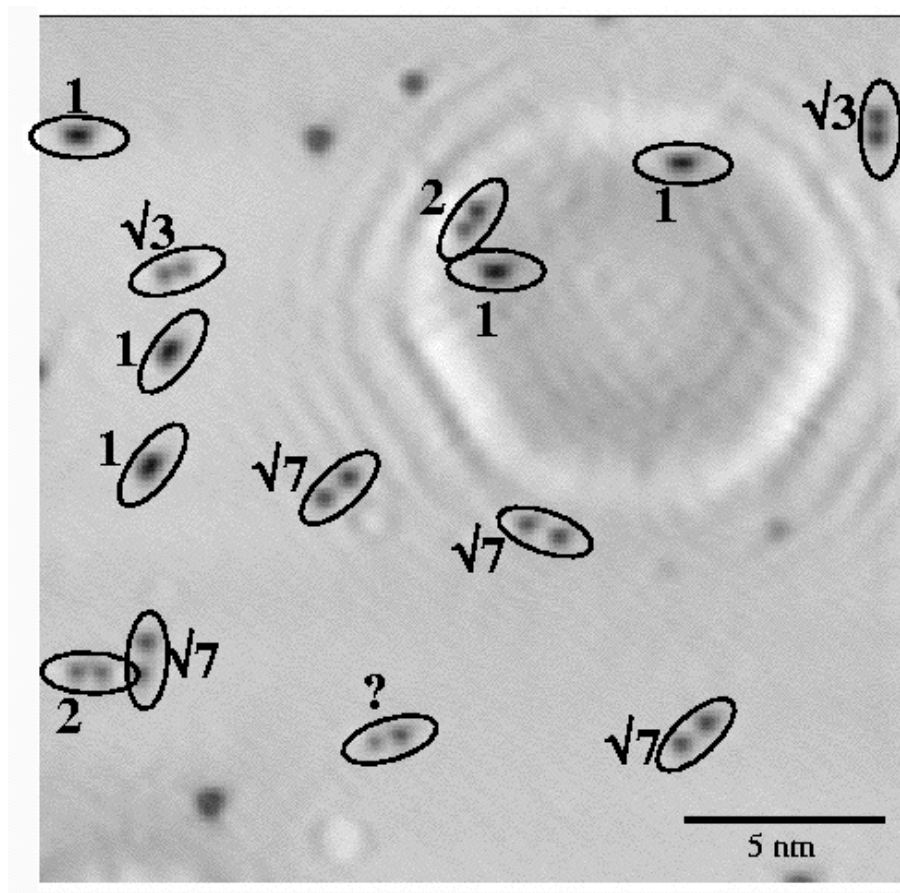


Fig. 5.3: STM image (imaged area  $20 \times 20 \text{ nm}^2$ ;  $I_t = 0.75 \text{ nA}$ ,  $V_t = -3 \text{ mV}$ ) of an Al(111) surface at 80K after exposure to O<sub>2</sub> at 150K. [Schmid,2001].

bour spacing,  $a_s = 2.86 \text{ \AA}$ . The pair labeled “?” has been tentatively attributed to O-atoms adsorbed at two non-equivalent sites (fcc hollow and hcp). The authors attributed the interference pattern to a subsurface argon bubble. The adatom pairs in Fig. 5.3 have been interpreted as the result of *side-on* chemisorption events. The distance between the dissociation fragments should arise from the dissipation of the excess chemisorption energy through transient hyperthermal motion. The measured O-O distances are consistent with the results of the molecular dynamics study of Engdahl and Wahnström [Engdahl, 1994]. The barrier to O diffusion on Al(111) has been estimated to 0.75 eV, corresponding to a diffusion rate of roughly one hop per second at room temperature [Jacobsen, 1995]. Hence, isolated O-atoms should be trapped in metastable states on a cold surface. At room temperature the O-adatoms may coalesce into dimers and larger islands, because of their mutual attraction. Therefore, the exposure of a pristine aluminum surface to  $O_2$  doses in the Langmuir range at room temperature should only produce dimers. The result of such a study is shown in Fig. 5.4. Here dimers and trimers could be detected, but no monomers. The dissociation of  $O_2$  approaching the surface *side-on* cannot explain the existence of trimers, given the low transient mobility of the molecular fragments. The existence of an abstraction pathway for the chemisorption is required to produce single O

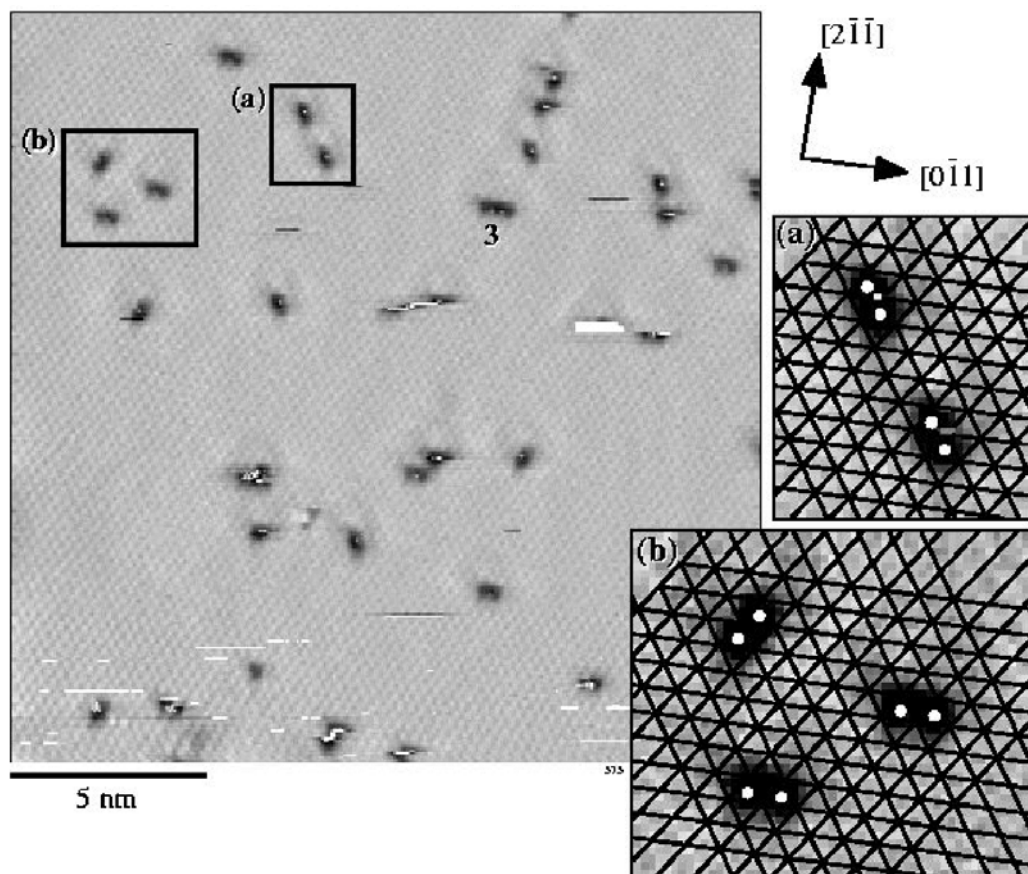


Fig. 5.4: Room-temperature STM image of an Al(111) surface after exposure to  $1.5L O_2$  ( $I_t = 0.46 \text{ nA}$ ,  $V_t = -3 \text{ mV}$ ; imaged area  $20 \times 20 \text{ nm}^2$ ). The aluminum lattice and the positions of the O-atoms (white filled circles) are indicated in the enlarged frames (a) and (b). The location of the protrusions occasionally appearing in the dark spots, e.g. in frame (a), coincides with that of Al sites [Schmid, 2001].

adatoms close to preexistent dimers. Then, the single atom could thermally diffuse until being trapped by the dimer or a higher coordination island.

Here it has to be mentioned that the tunneling conditions chosen by Brune and coworkers and Komrowski and Kummel are comparable, while the tunneling currents chosen by Schmid and coworkers are two orders of magnitude smaller. According to Schmid and coworkers, protrusions similar to those imaged in Fig. 1.5 and Fig. 5.1 are invisible at larger tunneling distances. They only appear when the tunneling current is increased, *i.e.* at small tip-sample distances. Hence, these features should be attributed to tip-sample interaction and not to the local density of states. In this case, each of the single protrusions in Fig. 1.5 and Fig. 5.1 should be constituted by one substrate Al atom among two O atoms [Schmid, 2001].

On the other hand, this interpretation fails to explain the STM results shown in Fig. 5.2, where the imaged features result from absorption of O atoms. If the energy barrier for O atoms diffusion were overcome at room temperature and only pairs of adatoms were to be detected, then the features in Fig. 5.2 should show the same symmetry as the one in the insets of Fig. 5.4. Since this is not the case, it is possible to conclude that O atoms on Al surfaces are stable enough to be detected at room temperature.<sup>1</sup> As already pointed out, this argument would support the interpretation of the features in Fig. 1.5 and Fig. 5.1 as single atoms. Since the atomic structure of the substrate is visible both in Fig. 5.1 and in Fig. 5.4, it is possible to compare the geometrical dimensions of the dimers in the two images. The dimers imaged on a room temperature Al(111) surface by Schmid and coworkers [Fig. 5.5.a)] are very similar to the dimers imaged by Komrowski and Kummel [Fig. 5.5.b)], but quite different from their monomers [Fig. 5.5.c)]. Therefore, I suggest that the interpretation of the features in the STM data of Brune and coworkers as single O atoms is correct. The reason why O monomers were not detected by Schmid and coworkers remains obscure.

It is evident from these notes, that the discussion around the interpretation of the STM data relative to O<sub>2</sub> chemisorption on Al(111) is far from settled. Nonetheless, despite the aforementioned discrepancies, all of the STM results support the hypothesis

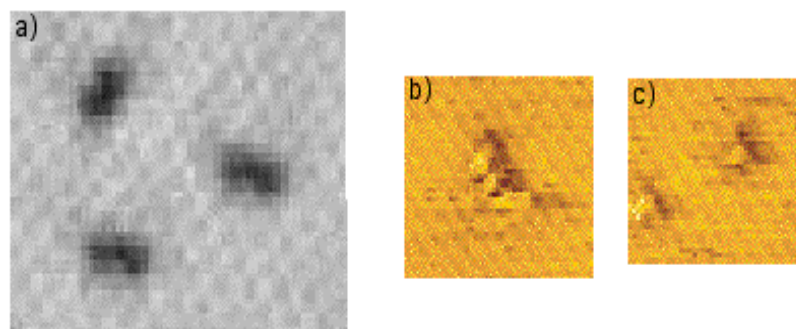


Fig. 5.5: Comparison of monomers and dimers from previously shown STM images; a) is a detail from Fig. 5.4, b) is a detail of a dimer from Fig. 5.1 and c) is a detail of a monomer from Fig. 5.1 [Schmid, 2001; Binetti, 2000].

1. Trost and coworkers studied the O-island formation process on Al(111) at 440K, and derived a migration barrier of  $1.0 \div 1.1$  eV [Trost, 1998].

of the existence of an abstraction channel for O<sub>2</sub> dissociative chemisorption on aluminum, consistently with the present laser spectrometric results.

### 5.1 ON THE REACTION DYNAMICS

One important question concerns the disposal of the heat of reaction. The chemisorption of one single O-atom is estimated to be exothermic by 7.95 eV, exceeding the value of the O<sub>2</sub> bond energy, 5.16 eV, by 2.79 eV [Jacobsen, 1995]. This excess energy ( $E_{\text{ex}}$ ) has to be dissipated between the dissociation fragments and the heat bath of the metal. If the dissociation would take place far away from the surface, where the molecule could be approximated with an isolated system, the exothermicity should be only partitioned between the two fragments. This would imply a translational energy of approximately 1.4 eV for the recoiled atom. On the other hand, if the dissociation takes place with the molecule close to the surface, the abstracted O-atom interacts strongly with the Al surface. Results from a study of O<sub>2</sub>/Al(111) non-reactive scattering indicate, that these events involve the incoming molecule and a cluster of approximately three surface atoms [Weiße, 2001]. Therefore, in the abstraction event, the mass of the abstracted O-atom can be replaced by  $m_{\text{eff}}$ , the mass of a cluster composed by the incoming O-atom and three Al-atoms surrounding the three-fold hollow site where chemisorption takes place [Wahnström, 1996]. If the initial momentum of the molecule is zero, the conservation of energy and momentum imposes a kinetic energy  $E_{\text{trans}}(\text{O}) = E_{\text{ex}} / [1 + m(\text{O})/m_{\text{eff}}] = 2.4 \text{ eV}$  for the recoiled atom.<sup>1</sup> The measured value of  $0.4 \pm 0.1 \text{ eV}$  for  $E_{\text{trans}}(\text{O})$  amounts to approximately 13% of the overall exothermicity. This shows, that no simplified, classical approach can be applied in this case.

From previous studies of abstraction reaction at surfaces it is known, that the energy carried away by reaction fragments in the gas phase is always a small fraction of the total exothermicity. As an example, the median translational energy of halogen atoms ejected upon interaction of an ICl molecular beam with a silicon surface was determined to be well below 20% of the available excess energy (14% for ejected iodine atoms and 9% for ejected chlorine atoms) [Pettus, 1999]. These results again show, that a purely mechanical energy transfer mode cannot explain how the exothermicity is disposed of in these reactions.

The low translational energy measured might result from the concerted motion of the incoming and substrate atoms upon formation of the Al-O bond, while the O-O bond lengthens. This is consistent with what is known for the interaction of heavy atoms with heavy molecules in the gas phase, where the reaction leads to a mixed energy release (i.e.: energy is released into translational as well as internal excitations) [Hodgson, 1971]. Then, at least part of the reaction exothermicity could be dissipated into the phonon bath of the surface.

Another energy dissipation channel is constituted by the possible electronic excitations of the surface. The recoiling O-atom is initially produced as O<sup>-</sup>-ion close to the surface, but its ground state away from the surface is neutral [Lang, 1978]. Therefore, a charge transfer process must take place when the recoiling O-atom leaves the Al surface.

---

1. With the experimental setup used in the present study, the highest  $E_{\text{trans}}$  available for the O<sub>2</sub> molecules is 0.5 eV, only 15% of the overall exothermicity of the dissociation reaction.

The charge transfer is allowed once the oxygen affinity level,  $E_O^A$ , crosses the Al work-function  $\Phi$ . An estimate for this distance, also called *ionization distance*  $z_{\text{ion}}$ , is given by

$$z_{\text{ion}} = \frac{e^2}{4\pi\epsilon_0} \cdot \frac{1}{4(\Phi - E_O^A)} = \frac{3.6\text{\AA}}{\Delta E[\text{eV}]} \quad (5.1)$$

$z_{\text{ion}}$  is referred to the image plane of the metal, positioned  $1.38\text{\AA}$  away from the outermost surface layer [White, 1998]. For  $\text{O}_2$  molecules interacting with a pristine Al surface,  $E_O^A = 1.46\text{eV}$  and  $\Phi = 4.3\text{eV}$ ,  $z_{\text{ion}}$  is only  $1.3\text{\AA}$ , and the charge transfer process should take place when the molecule is located  $2.68\text{\AA}$  away from the surface. Such a small value for  $z_{\text{ion}}$  implies, that even if the atom leaves the surface in a charged state, its most probable state away from the surface will still be a neutral one [Teillet-Billy, 1995]. The charge transfer process can take place starting from the occupied  $E_O^A$ , into one of the empty electronic states above the Fermi level of the metal. This electron will dissipate its excess energy, by thermalization with the electron bath of the solid.

To clearly discriminate between these two energy dissipation modes, at least one of them should be directly investigated. If the molecular heat of adsorption ( $H_{\text{ad}}$ ) could be directly measured, e.g. with a femtomole calorimeter, the energy dissipated in the electron bath could be estimated by subtraction of  $E_{\text{trans}}(\text{O})$  and  $H_{\text{ad}}$  from the O-atom chemisorption energy.<sup>1</sup> Another promising approach is the one followed by Nienhaus and coworkers, who demonstrated the possibility of direct detection of electron-hole pairs generated during chemical reactions on metal surfaces, by means of Schottky junctions [Nienhaus, 2000]. The basic idea is to deposit a thin film ( $\approx 10^2\text{\AA}$ ) of silver on a Si(111) surface in UHV, creating a Schottky diode of approximately  $30\text{mm}^2$ . Exposure of the metal surface to atomic hydrogen or  $\text{O}_2$  caused the creation of  $e$ - $h$  pair in the metal, that could be detected as a chemically induced current (*chemicurrent*) in the diode. An improved design of this experimental setup has been implemented, involving the use of metal-insulator-metal tunneling contacts, to allow spectroscopy of the  $e$ - $h$  pairs, but data relative to the energetic of  $\text{O}_2$  chemisorption are not yet available [Nienhaus, 2001].

The measured value for  $E_{\text{trans}}$  of the recoiled atoms remained constant over the range of incident molecular beam energies investigated ( $90\text{meV} \div 450\text{meV}$ ). This should not surprise: if only 12% of the overall exothermicity is dissipated into the translational degree of freedom of the recoiled atoms, variations of  $E_{\text{trans}}(\text{O}_2)$  in the experimental range should affect  $E_{\text{trans}}(\text{O})$  by approximately 2%. Being approximately 10 times smaller than the experimental variance, this effect could not be detected.

## 5.2 ABSTRACTION PROBABILITY VS. INCIDENT POLAR ANGLE

The yield of O-atoms is directly proportional to the abstraction coefficient  $\sigma_{\text{ab}}$  and to the initial sticking coefficient ( $S_0$ ) in the low  $E_{\text{trans}}(\text{O}_2)$  regime. Therefore, yield variations are expected to mirror  $S_0$  variations at low translational energies. In the present work, I investigated the O-atom yield as a function of  $\theta_i$ , at different beam  $E_{\text{trans}}$ . I also investigated the behaviour of  $S_0$  as a function of  $\theta_i$ , by means of AES, for a thermal  $\text{O}_2$  beam. The results displayed in Table 4.5 show a maximum for  $\theta_i \approx 25^\circ$  and a symmetrical reduction to approximately 86% of that value at higher and lower  $\theta_i$ . On the contrary, Fig. 4.9

---

1. King and coworkers have demonstrated, that it is possible to detect heats of adsorption  $H_{\text{ad}}$  in the femtomole range during chemisorption processes [King, 1998 and references therein].

shows that the O-atom yield drops practically to zero at low  $\theta_i$ , crosses an absolute maximum at  $\theta_i=30^\circ$  and decreases smoothly at higher incident angles, similarly to  $S_0$ . To ease the individuation of general trends, the O-yield distributions displayed in Fig. 5.6 are normalized with respect to their maxima.

Both sets of data present a maximum for  $\theta_i \neq 0$ , suggesting that “Normal Energy Scaling” may not apply to either one of the two quantities. Under this respect, the present findings are qualitatively similar to that published by Österlund *et al.* [cf. Fig. 4.8]. But those sets of data are different under two relevant aspects:

- $S_0$  and O-yield determined in this work are much smoother functions of  $\theta_i$  than the absolute  $S_0$  measured by Österlund *et al.*.  $S_0$  was only determined for a thermal  $O_2$  beam and a reduced set of geometries in the present work. On the contrary, the results published by Österlund *et al.* are relative to molecular beams at higher translational energies. Therefore, a direct comparison within the two sets of measurements might be somewhat misleading.
- Care must be taken when analyzing the REMPI data, since the sensitivity of the REMPI-ToF mass spectrometer depends on the angle  $\theta_i$  between the ToF-tube axis and the surface normal, decreasing at higher  $\theta_i$  values [Section 4.4]. Then, a direct comparison between REMPI data and  $S_0$  might only be meaningful at  $\theta_i > 25^\circ$ . The intensity of the O-yield distributions as a function of  $\theta_i$  seems to follow a general scaling law, independent from the translational energy of the incoming molecules. Once normalized, the experimental distributions converge to a “universal” curve closely resembling a  $\cos^2\theta_i$  distribution, within a variance of  $\pm 10\%$ . This is not the case for  $S_0(\theta)$ . This difference could result from the presence of the competing chemisorption channel at higher energy.

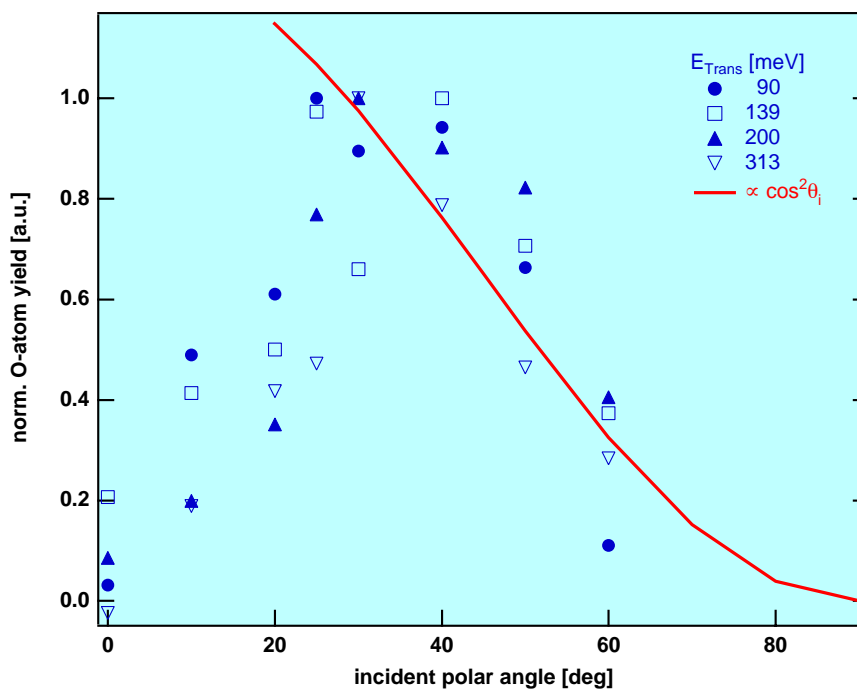


Fig. 5.6: Normalized O-atom yield and as a function of the incident polar angle  $\theta_i$  of the incoming beam. The solid line represents a  $\cos^2 \theta_i$  distribution.

To clarify this topic, I extracted the values of  $\sigma_{ab}$  from the O-yields [Section 4.6.1] and plotted them as a function of the normal energy. The results are shown in Fig. 5.7. Two subsets of values can easily be distinguished, characterized by different nozzle temperatures: the filled symbols indicate the data measured with the nozzle at room temperature (300K), while the void symbols represent data measured with the nozzle at a temperature of 500K. The solid and the broken lines are fit to the data, according to the equation

$$\sigma_{ab}(E_{trans}) = \frac{\sigma_{ab}^{sat}}{2} \left( 1 + \tanh \left[ \frac{E_{trans} - E_{act}}{W} \right] \right), \quad (5.2)$$

originally proposed by Harris to represent the results of quantum calculations for the dissociation of  $H_2$  on copper surfaces [Harris, 1989]. In the present case,  $\sigma_{ab}^{sat}$  is the saturation value for the abstraction probability. The abstraction process takes place on a multidimensional energy landscape, characterized by the existence of different barriers, depending on the orientation of the molecule.  $E_{act}$ , the value of the apparent barrier to abstraction, is the average barrier height. The width  $W$  represents the width of the distribution of the barrier heights [Michelsen, 1991]. The values of the fitting parameter are listed in Table 5.1. The vertical error bar represents the convolution of the variance with the estimated uncertainty. The horizontal error bar shows the accuracy on the beam energy measure. In view of the limited energy range accessed in the present experiment, the saturation region of the abstraction probability growth rate could not be accessed. The value of 0.6 for  $\sigma_{ab}^{sat}$  was borrowed from a very recent STM investigation by Komrowsky *et al.* on the reaction of Al(111) with  $O_2$  from a molecular beam as a function of the beam energy [Komrowsky, 2001]. Due to the uncertainty affecting the mea-

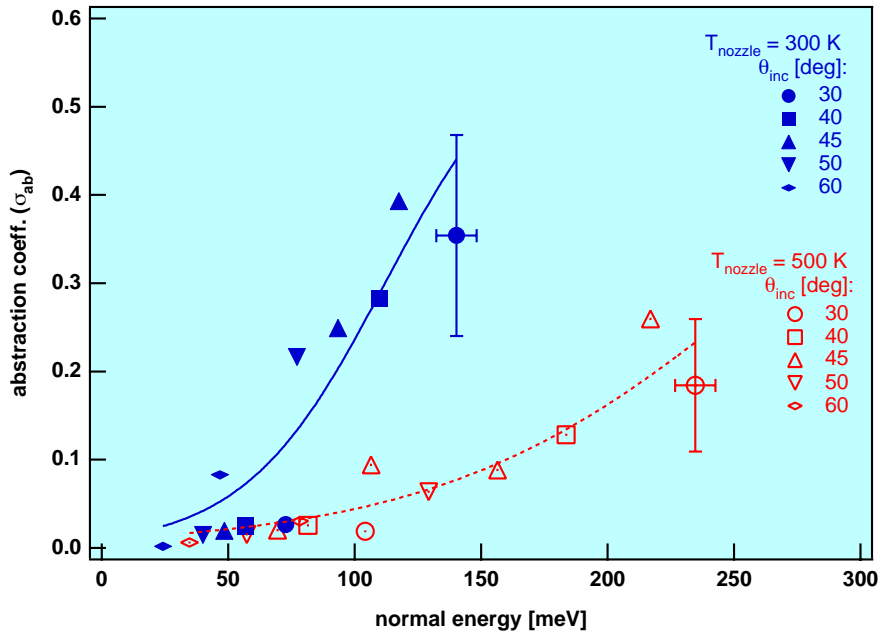


Fig. 5.7:  $\sigma_{ab}$  as function of the normal translational energy. The filled symbols are for the measurements with the nozzle at room temperature. The void symbols show the results with the nozzle at 500K. The solid and broken lines are fit to the data according to Eq. 5.2.

surements, the values of  $E_{\text{act}}$  and  $W$  in Table 5.1 should be taken considered as estimates for those quantities.

The data in Fig. 5.7 show, that within the limits of the experimental accuracy, the abstraction process seems to follow a NES behaviour, with an apparent activation barrier, dependent on the temperature of the incoming gas. However, it should be considered, that the existence of an apparent activation energy for abstraction does not necessarily imply the existence of an absolute barrier for that process, but might result from dynamical effects. This topic will be discussed in the Section 5.5.

As I mentioned in Section 1.3, the Al(111) surface is highly corrugated for the incoming  $\text{O}_2$  molecules. This would suggest a marked dependence of the scattering phenomena from the incidence angle. Nevertheless, by means of molecular dynamics simulations Darling *et al.* have shown, that the geometrical and energetical corrugations of a PES may balance, when the orientation of the approaching molecules during the scattering events are considered [Darling, 1994]. Therefore, the angular dependence of dissociation probability cannot be taken as a reliable indication for the smoothness of the PES. Actually, the observation of *NES* behaviour for processes taking place on highly symmetrical and corrugated surfaces as Al(111) is a rather normal event, while the marked dependence of  $S_0$  on  $\theta_i$  found by Österlund *et al.* is quite unusual.

### 5.3 O-ATOM YIELD VS. SURFACE COVERAGE ( $\Theta$ )

The laser spectrometric results presented in Fig. 4.11 indicate an initial increase in abstraction yield with surface coverage ( $\Theta$ ). After crossing a maximum, the yield drops. Such an effect could be ascribed to the initial decrease of the surface workfunction ( $\Phi$ ) with increasing  $\Theta$ . This is a well-known phenomenon, that has been reported for both contact potential difference and medium-energy ion spectroscopy measurement [Gartland, 1977; Michel, 1980; Ustaze, 1998].

Lowering of  $\Phi$  allows electron transfer to the incoming molecules further away from the metal surface. The likelihood of the abstraction process increases accordingly. At higher  $\Theta$ ,  $\Phi$  increases again, reducing the possibility of electron transfer and, consequently, of abstraction. The fluctuation constituting the fine structure of these diagrams are not reproducible [cf. Fig. 4.11].

### 5.4 ABSTRACTION PROBABILITY VS. BEAM ENERGY

The abstraction of an O-atom from an incoming  $\text{O}_2$  molecule by an Al surface is a complex phenomenon, including several, probably non-adiabatic, charge transfer processes. As already shown in Section 5.2, it strongly depends on the energy of the incoming molecules. In an attempt to isolate the effect of the beam energy on the abstraction

**Table 5.1: Saturation value for  $\sigma_{\text{ab}}$ , activation energy and barrier width for abstraction as a function of  $T_{\text{nozzle}}$  [Eq. 5.2]**

$T_{\text{nozzle}}$ [K]	$E_{\text{act}}$ [meV]	$W$ [meV]
300	$112 \pm 5\%$	$55 \pm 20\%$
500	$264 \pm 14\%$	$129 \pm 16\%$

dynamics, the dependence of  $\sigma_{ab}$  on  $E_{\text{trans}}$  has been investigated for a defined scattering geometry, namely  $\theta_i=45^\circ$ . The results of these measurements are shown in Fig. 5.8 together with  $S_0$  determined by Österlund *et al.* The values of  $S_0$  are displayed as void circles.  $S_0$  steeply rises from the lowest measured value of  $(1.4\pm 0.5)\cdot 10^{-2}$  at  $E_{\text{trans}}=24\text{meV}$  to an almost constant value of  $0.90\pm 0.04$  at  $E_{\text{trans}}$  between 600meV and 2000meV, showing a strongly activated character for the dissociative chemisorption. The sticking coefficient smoothly approaches zero at low energies, showing no evidence for an energy threshold. The inflection point for  $S_0(E_{\text{trans}})$  is located at approximately 200meV. The effect of the vibrational excitation was investigated, preparing the beam with different amounts (up to 20%) of vibrationally excited molecules [Österlund, 1997]. AES and King-Wells techniques were used to determine  $S_0$ . AES was used to determine the amount of O-atoms present on the surface after exposure to the  $\text{O}_2$  beam. It is a highly sensitive technique, but does not provide an absolute measurement of the coverage,  $\Theta$ . It was used to determine  $\Theta$  in the low energy regime, for  $S_0$  lower than 0.2. The King-Wells technique is based on the detection of variation in the background partial pressure of the gas interacting with a surface. It has a lower sensitivity when compared to AES, but can provide an absolute determination of  $\Theta$ . It was used at  $S_0$  higher than 0.1, allowing the calibration of AES in the region where the sensitivities overlap. Both of these techniques allow the measurement of the *integral* sticking coefficient, in the sense that they do not allow to discriminate between alternative chemisorption pathways.

The present experiment consisted in the REMPI detection of O-atoms in the proximity of an Al(111) surface exposed to  $\text{O}_2$  from a molecular beam. With this setup, atoms released during abstraction are selectively observed, and the *differential* sticking coefficient due to this reaction channel ( $\sigma_{ab}$ ) is determined. In Fig. 5.8, the values for the

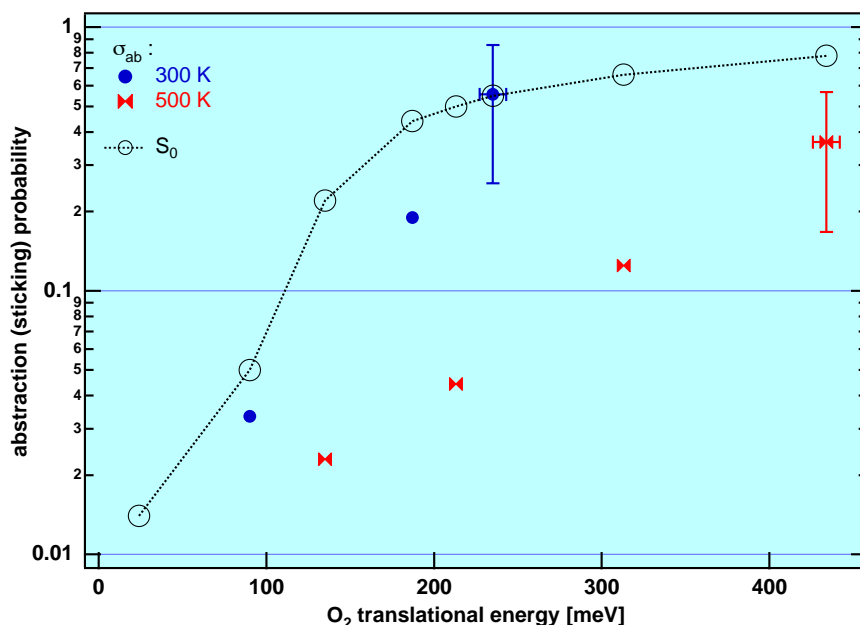


Fig. 5.8:  $\sigma_{ab}$  as function of the translational energy of the incident molecules. The error bars show the convolution of the variance with the estimated uncertainty (vertical) and the accuracy on the beam energy measure (horizontal). The value of the initial sticking coefficient ( $S_0$ ) from the work of Österlund *et al.*, is shown as a reference [Österlund, 1997].

abstraction probabilities are shown as filled symbols. Within the limits of the experimental accuracy, these values are generally lower than the respective ones for  $S_0$  at hyperthermal energies. This is a natural consequence of the coexistence of two alternative chemisorption channels, namely an abstractive one and a normal dissociative chemisorption one, at higher energies [Binetti, 2000].

If the abstraction reaction follows NES, as suggested by the results of the previous analysis of  $\sigma_{ab}$  as a function of  $\theta_i$  [Section 5.2], the data in Fig. 5.8 should be rescaled to account for the lower velocity of the incoming molecules normal to the surface [Eq. 4.36].<sup>1</sup> In the diagram of Fig. 5.9 the rescaled data for  $\sigma_{ab}$  are displayed as a function of the normal translational energy. The diagrams in Fig. 5.8 and Fig. 5.9 are, of course, qualitatively similar. Their main difference is, that the latter shows a steeper rise of  $\sigma_{ab}$  as a function of the beam energy. The values for  $\sigma_{ab}$  measured with the nozzle at 300 K are somewhat higher than the respective  $S_0$  values, but the differences are within the accuracy of the measurement. In view of the difficulties connected with the REMPI calibration [Section 4.6.1], the  $\sigma_{ab}$  values can be considered in good agreement with the  $S_0$  ones.

Based on a statistical analysis of the STM images of Brune *et al.*, abstraction was expected to play a major role in the dissociation processes of thermal molecules, where the incidence of dissociative chemisorption should be marginal. Both in the diagram in Fig. 5.8 and in Fig. 5.9, this expectation is confirmed by the set of REMPI data taken

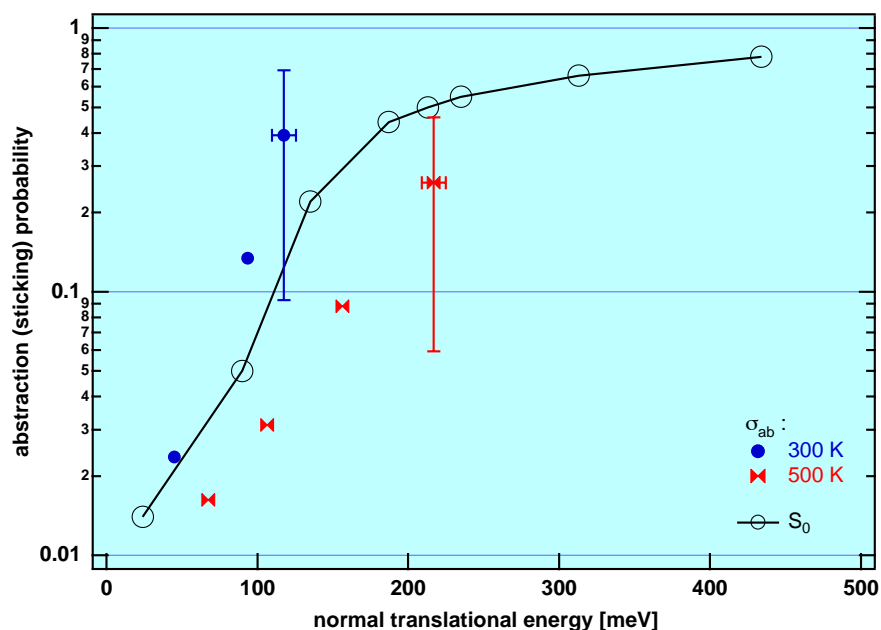


Fig. 5.9:  $\sigma_{ab}$  as function of the normal translational energy of the incident molecules. The values of  $\sigma_{ab}$  from Table 4.7 are rescaled to account for the reduced  $v_{\perp}(O_2)$  normal to the surface. The error bars show the convolution of the variance with the estimated uncertainty (vertical) and the accuracy on the beam energy measure (horizontal). The value of the initial sticking coefficient ( $S_0$ ) from the work of Österlund *et al.* is shown as a reference [Österlund, 1997].

1. Since for  $\theta_i \neq 0^\circ$ , the component of the velocity normal to the surface is  $v_{\perp}(O_2) = v \cdot \cos\theta_i$ , this amounts to multiply the values of  $\sigma_{ab}$  in Table 4.7 by  $\cos(45^\circ)$ .

with the nozzle at 300K, where the discrepancy between  $\sigma_{ab}$  and  $S_0$  at thermal energies is within the experimental accuracy. At a higher nozzle temperature (500K) abstraction is hindered and its apparent activation energy is considerably higher than the one shown at 300K [cf. Table 5.1]. Since  $S_0$  grows continuously with the translational energy, this means, that the probability for dissociative chemisorption must also grow with the  $T_{nozzle}$ . In the next two sections a mechanism will be proposed to rationalize this result.

The present findings are also complemented by very recent STM investigations of the reaction of Al(111) with  $O_2$  from a molecular beam, as a function of the beam energy by Komrowsky *et al.* [Komrowsky,2001]. In particular, in that work it has been demonstrated that the probability for dissociative chemisorption grows faster with the  $E_{trans}(O_2)$  than the abstraction probability. In order to analyze their STM images, Komrowsky *et al.* catalogued each oxygen feature and determined an absolute oxygen coverage of  $0.005 \div 0.037$  ML for the investigated surfaces. The ratio of the number of single chemisorbed O-atoms to O-pairs (S/P) versus  $E_{trans}(O_2)$  gave a measure of the relative probability for the two alternative reaction pathways. The results are shown in Fig. 5.10. For a surface exposed to thermal oxygen, the S/P ratio presents its maximum (15:1). The S/P value rapidly decreases with increasing beam energies: it reaches a stable value of 2:1 for  $E_{trans}(O_2)$  higher than 500meV.

#### 5.4.1 Effect of the vibrational excitation

The data relative to the abstraction probability as a function of the incident polar angle shown in Section 5.2 show, that the apparent activation energies are correlated with the nozzle temperature. A simple inspection of the data in Fig. 5.8, relative to the depen-

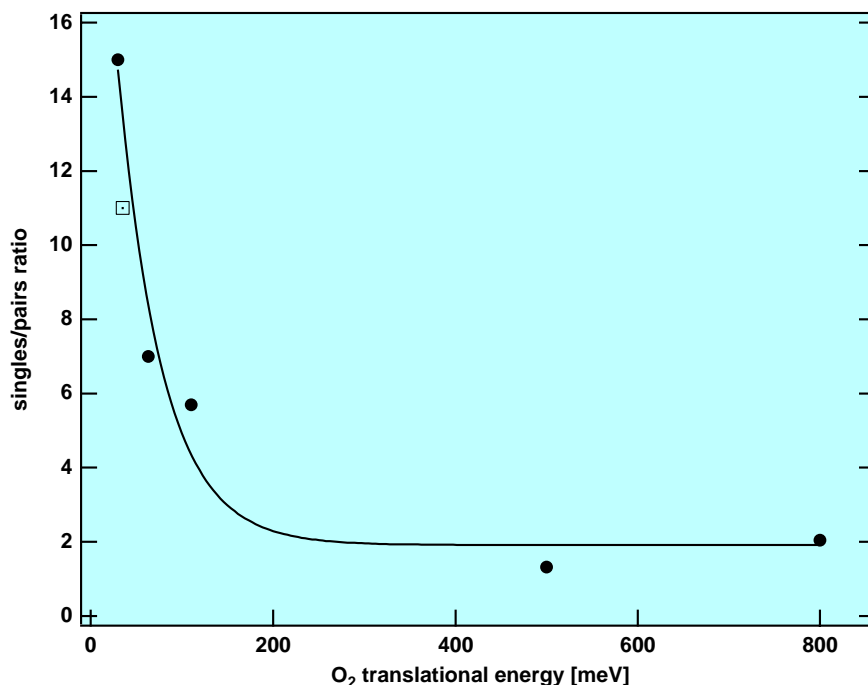


Fig. 5.10: Adsorbate distribution analysis from STM data. The ratio of single chemisorbed O atoms to the oxygen pairs (S/P) as a function of  $E_{trans}(O_2)$  is shown. The filled symbols are relative to the study by Komrowski *et al.* The void symbol is relative to the work by Brune *et al.* for thermal oxygen [Komrowski,2001; Brune, 1992]. The line is drawn to guide the eye.

gency of  $\sigma_{ab}$  on the beam energy at a fixed incident angle ( $\theta_i=45^\circ$ ), allows to draw the same conclusion: the set of  $\sigma_{ab}$  data can be split into two subsets, according to the nozzle temperature, each of them showing an exponential growth with  $E_{\text{trans}}(\text{O}_2)$ . To discriminate between effects due to the translational and roto-vibrational degrees of freedom, an experiment was made to check the dependence of  $\sigma_{ab}$  on the nozzle temperature, at constant  $E_{\text{trans}}$ . A mixture of 35%  $\text{O}_2$  in He was prepared, that produced a molecular beam with a translational energy of 213 meV upon expansion from the nozzle at 500K. The value 0.044 for  $\sigma_{ab}$  measured in this experiment can be compared to the values obtained for thermal beam from a mixture of 20%  $\text{O}_2/\text{He}$  ( $\sigma_{ab}=0.19$ ,  $E_{\text{trans}}=187$  meV) and from a mixture of 10%  $\text{O}_2/\text{He}$  ( $\sigma_{ab}=0.556$ ,  $E_{\text{trans}}=235$  meV). These data are summarized in Table 5.2. The abstraction probability for the beam expanding from the heated nozzle was found to be considerably lower than the one measured for the beam expanding from the nozzle at room temperature. This clearly showed the existence of a correlation between the temperature of the expanding gas and  $\sigma_{ab}$ .

As mentioned in Section 2.2, both thermal and hyperthermal beams are formed by supersonic expansion of gas from a reservoir at room temperature, *i.e.* the pulsed valve. The gas is heated while traversing the ceramic capillary connected to the valve. Emerging from the capillary heated to 500K, the gas has the same translational energy it would have upon expansion from a source in equilibrium at 462K. This temperature difference causes a difference in the vibrational and rotational excitation of the expanding gases.

It is well-known, that vibrational excitations may increase dramatically the reactivity of gas molecules [Hayden, 1989]. During the expansion process, the vibrational degree of freedom of diatomics is largely frozen [Section 2.2.2]. This implies that the vibrational excitation of the expanding gas is the same *before* and *after* the expansion, *i.e.* that the vibrational temperature  $T_{\text{vib}}$  is equal to  $T_{\text{gas}}$ . From quantum statistical mechanics it is known, that the occupation probability of the vibrational levels for a diatomic gas at a given temperature is

$$p_v = \frac{e^{-(v+1/2)\frac{\hbar\omega}{kT}}}{Z_{\text{vib}}}, \quad (5.3)$$

where  $\omega$  is the angular frequency of the molecular vibration and  $Z_{\text{vib}}$  is its vibrational partition function

$$Z_{\text{vib}} = \sum_v e^{-(v+1/2)\frac{\hbar\omega}{kT}} = \frac{e^{-\frac{\hbar\omega}{2kT}}}{1 - e^{-\frac{\hbar\omega}{kT}}}. \quad (5.4)$$

**Table 5.2: Abstraction probability and beam temperature**

$T_{\text{gas}}$ [K]	Seeding [O <sub>2</sub> % in He]	$E_{\text{trans}}$ [meV]	$T_{\text{rot}}$ [K]	$\sigma_{ab}$
300	20	187	55	0.190
462	35	213	150	0.044
300	10	235	57	0.556

Given  $\hbar\omega/k(\text{O}_2)=2260\text{K}$ , it is straightforward to calculate the  $p_v(\text{O}_2)$  at the temperatures of interest and the relative variations [Alonso,1968; Huber,1979]. The results are illustrated in Fig. 5.11. The population of the vibrationally excited state ( $v>0$ ) is one order of magnitude lower than both the initial sticking coefficient and the abstraction probability at the estimated vibrational beam temperature. This shows, that the vibrational degree of freedom plays only a minor role in the dissociation at the investigated beam temperature. Increasing the gas temperature from 300K to 500 K reduces the population in the vibrational ground state by approximately 0.7%. As shown in Fig. 4.17, the value of  $\sigma_{\text{ab}}$  obtained for an heated beam is approximately 30% of the value obtained for a room temperature beam, although  $E_{\text{trans}}$  is comparable in the two cases. Hence, a cause must be found, to explain a 70% reduction of  $\sigma_{\text{ab}}$ . The thermally induced variation of the population in the vibrational ground state seems too small to account for this effect.

#### 5.4.2 Effect of the rotational excitation

Variations in the temperature of the gas reservoir also affect the final rotational temperature of the expanding gas. The rotational degree of freedom thermalizes during the supersonic expansion, freezing when the expansion is complete. Then the gas reaches a final rotational temperature ( $T_{\text{rot}}$ ), whose exact value depends on its composition, its initial temperature and the details of the expansion process [Section 2.2.2].  $T_{\text{rot}}$  has been measured for a molecular beam of NO as a function of the nozzle temperature and of the NO concentration. The results have been shown in Table 2.4.  $T_{\text{rot}}$  increases with the nozzle temperature and the dilution. The  $T_{\text{rot}}$  of a supersonic beam of  $\text{O}_2$  is expected to be very close to the  $T_{\text{rot}}$  measured for a NO beam, in the same condition of heating and seeding.

The effect of the rotational temperature of  $\text{O}_2$  on the abstraction probability can be rationalized as follows. Depending on its initial configuration, a molecule can be fun-

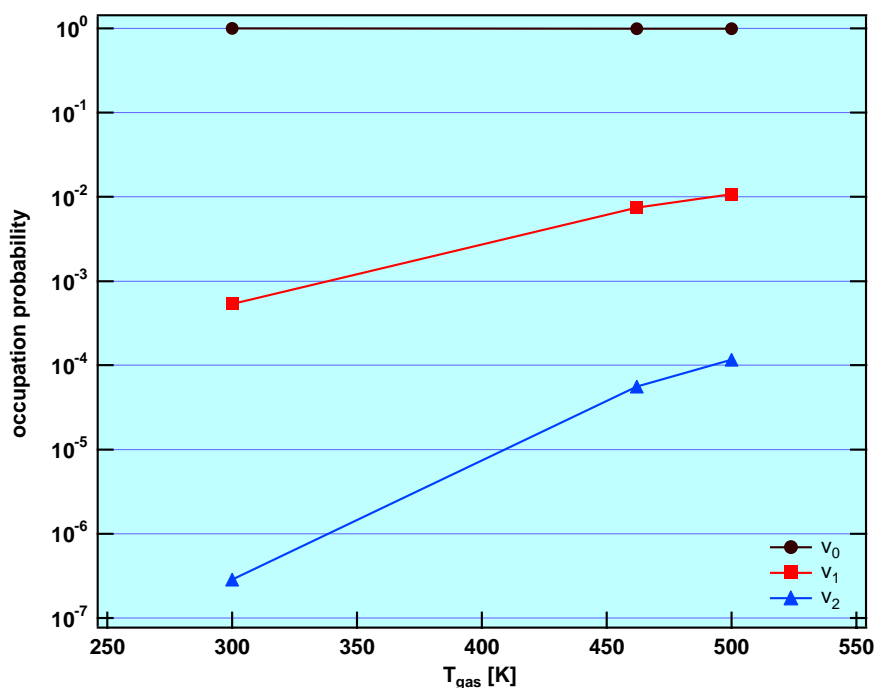


Fig. 5.11: Occupation probability of the first three vibrational states for  $\text{O}_2$  as a function of the gas temperature.

neled into an upright geometry while approaching the surface. According to the Hellman-Feynman theorem, the steering effect can be seen as resulting from the action of a torque on the molecule.<sup>1</sup> An increase in the rotational excitation opposes the steering effect. As a result, the number of molecules striking the surface in an *end-on* configuration is reduced and an anticorrelation between  $T_{\text{rot}}$  and  $\sigma_{\text{ab}}$  ensues.

In order to compare the preceding hypothesis with the experimental data, the occupation probability,  $p_J$ , of the rotational levels of  $\text{O}_2$  as a function of  $T_{\text{rot}}$  has been calculated. The occupation probability for the rotational levels of a gas at a given temperature is

$$p_J = \frac{(2J+1)e^{-J(J+1)\frac{\hbar^2}{2IkT}}}{Z_{\text{rot}}}, \quad (5.5)$$

where  $I$  is the momentum of inertia for the considered molecule. The rotational partition function,  $Z_{\text{rot}}$ , is defined as

$$Z_{\text{rot}} = \sum_J (2J+1)e^{-J(J+1)\frac{\hbar^2}{2IkT}}, \quad (5.6)$$

with  $\hbar^2/2Ik(\text{O}_2)=2.09\text{K}$ .  $Z_{\text{rot}}$  has been calculated iteratively for the expanding gas at the rotational temperatures of interest. The sum in Eq. 5.6 converges for  $J \geq 60$ . Hence, the value of  $Z_{\text{rot}}$  for  $J=60$  has been used hereafter. I define  $P_T(J')$  as the accumulated occupation probability of the first  $J'$  rotational states at a given rotational temperature  $T$ . It is defined by the equation

$$P_T(J') = \sum_{J=0}^{J'} p_J(T). \quad (5.7)$$

$P_T(J')$  decreases with increasing rotational temperature. In order to investigate the effect of the increased rotational temperature on the abstraction probability, it is useful to define a normalized depopulation ratio

$$\Delta P_{T'-T''}(J') = \frac{P_{T'}(J') - P_{T''}(J')}{P_{T'}(J')}, \quad (5.8)$$

whose value gives the difference between the accumulated occupation probability at two different rotational temperatures ( $T'' < T'$ ), normalized with respect to  $P_{T'}(J')$  at the lower temperature. The results for the evaluation of Eq. 5.8 at  $T_{\text{rot}}$  of interest are displayed in Fig. 5.12 as a function of  $J$ . Both of the curves show a maximum at  $J=0$  and approach smoothly 0 at high  $J$ . The amount of the normalized depopulation [Eq. 5.8] at low  $J$ , ( $\leq 3$ ) is close to 60%, in good agreement with the relative variation of  $\sigma_{\text{ab}}$ . This means, that the angular momentum of  $\text{O}_2$  molecules in the low-lying rotational states is already enough to efficiently hinder the steering effect. Assuming that the  $\text{O}_2$  behaves like a rigid rotor, its rotational energy will be

---

1. The so-called Hellman-Feynman theorem of quantum mechanical forces was originally proven by P. Ehrenfest, Z. Phys. **45**, 455 (1927), later discussed by Hellman (1937) and independently rediscovered by Feynman (1939).

$$E_{\text{rot}} = \frac{\hbar^2 J(J+1)}{2I} \quad (5.9)$$

with  $\hbar^2/2I = 0.178 \text{ meV}$ . This allows to estimate, that the corrugation of the PES responsible for the steering effect must not exceed some meV.

The mechanism proposed to explain the rotational hindering of abstractive dissociation is sketched in Fig. 5.13. The best candidate for abstraction reactions are the  $\text{O}_2$  molecules approaching the surface with their axis normal to the surface (*head-on* configuration). At large  $\text{O}_2\text{-Al}(111)$  separation, only the van der Waals interaction is present. Approaching the surface, the molecules can be funneled into an upright geometry, because of a steering force  $\mathbf{s}$  arising from asymmetries in the asymptotic van der Waals energy [Hult, 1999]. This mechanism should be most effective for molecules in the low lying rotational state ( $J \approx 0$ ), with their axis pointing less than  $30^\circ$  away from the surface normal [Yourdshahyan, 2001]. At higher  $T_{\text{rot}}$  the molecular angular momentum is increased. The torque  $\mathbf{r}$ , connected to the angular momentum, effectively counters the steering force  $\mathbf{s}$ . The result is an increase in the number of molecules approaching the surface in a *side-on* configuration, where the charge transfer from the surface is inhibited [Teillet-Billy, 1995]. Therefore, an increase in  $E_{\text{rot}}$  induces a decrease in  $\sigma_{\text{ab}}$ . Molecules approaching the surface with their axis more than  $30^\circ$  away from the surface normal, cannot be steered in an upright geometry and will scatter away, without being dissociated.

The absence of O-O pairs in the STM pictures at low  $E_{\text{trans}}$  indicates, that abstraction is the only open reactive channel in this regime. After supersonic expansion with the nozzle at room temperature  $T_{\text{rot}}$  of the beam should be approximately 55 K [Table 2.4]. Hence, only approximately 10% of the incoming molecules should be in the  $J=0,1$  state. Far away from the surface, the molecular axis points randomly in the space. Only one third of them, *i.e.* 0.03% of the total incoming molecules, can be steered *end-on* onto the

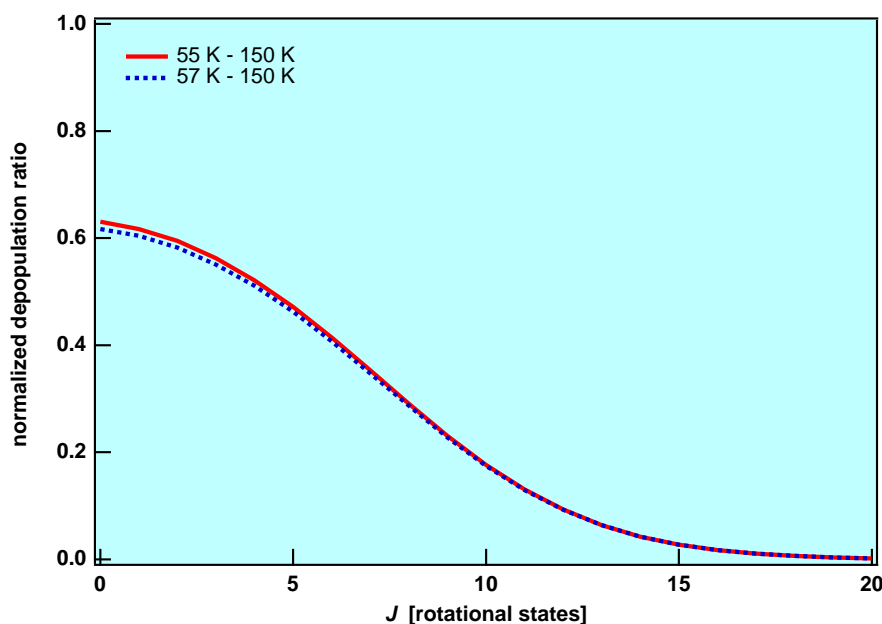


Fig. 5.12: Normalized depopulation ratio for  $\text{O}_2$  at the  $T_{\text{rot}}$  reached by the gas upon supersonic expansion, as a function of  $J$ .

surface. An energy barrier in the entrance channel may further reduce their abstraction probability. In this scenario the low  $S_0$  for thermal molecules ( $\leq 10^{-2}$ ), its stark increase with  $E_{\text{trans}}$  and the negative dependence of the abstraction coefficient from the rotational beam temperature can be understood.

STM images taken after Al exposure to a hyperthermal  $O_2$  beam (500 meV), show that monomers and dimers coexist. The monomers are due to abstractive chemisorption, while the dimers result from dissociative chemisorption (with  $O_2$  molecules in a *side-on* configuration), consistently with theoretical and experimental studies of halogen reactions with semiconductor and metal surfaces. The normal dissociative chemisorption pathway, which was completely closed to thermal  $O_2$ , is now available, because higher energy  $O_2$  can access previously forbidden regions of the multidimensional potential energy surface. The opening of an alternative chemisorption channel, reduces the statistical relevance of abstraction, as shown by recent STM measurements by Komorowski and Kummel [Komrowski, 2001]. Still, even at translational energies of 800 meV, abstraction should be responsible for approximately 60% of the dissociation events.

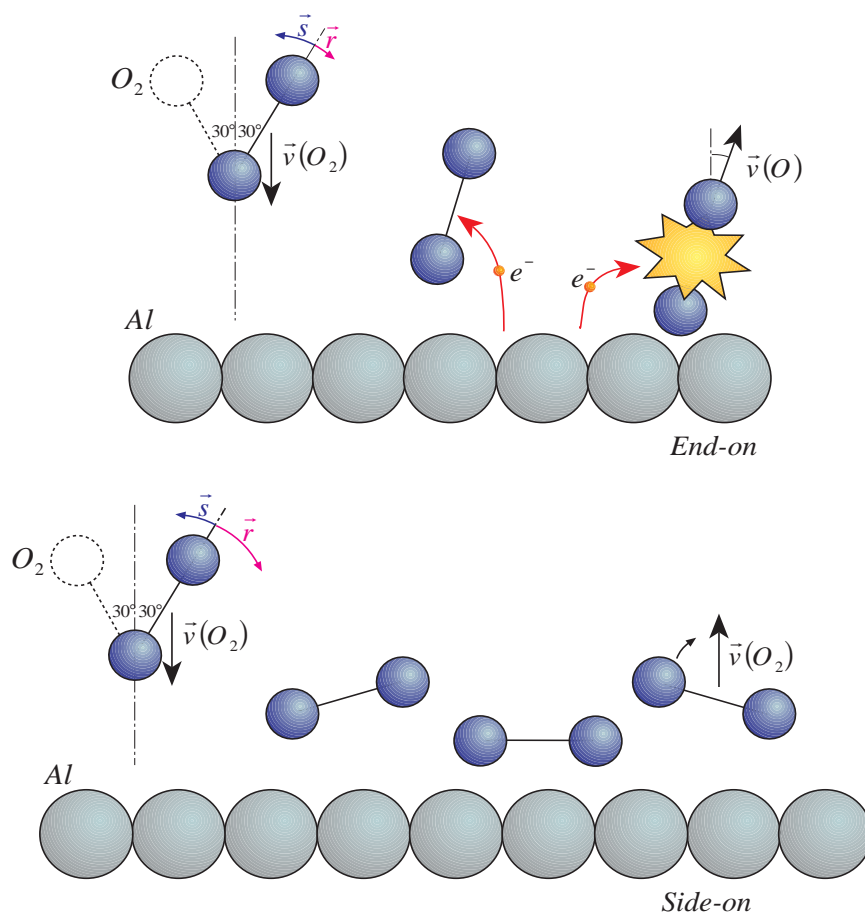


Fig. 5.13: Pictorial representation of the hindrance to abstractive chemisorption due to rotational excitation of the incoming molecules. The effect of the molecular torque  $\vec{r}$  due to the rotational excitation is to counter the steering  $\vec{s}$  arising from the  $O_2/Al(111)$  PES.

## 5.5 A BRIEF REVIEW OF RECENT THEORETICAL STUDIES

Recently, the  $\text{O}_2/\text{Al}(111)$  interaction has been the subject of several theoretical efforts, based either on *ab initio* or on semiempirical methods. *Ab initio* calculations were based on density functional theory (DFT), in terms of spin-polarized general-gradient approximation (GGA) and the pseudopotential method [Sasaki, 1999; Honkala, 2000; Yourdshahyan, 2001]. Their accuracy is currently limited to some hundreds of meV [Gross, 2001]. To have an estimate of the accuracy of such calculations, it is usual to compare measured parameters characterizing the molecules at the equilibrium, such as binding energies and bond lengths for  $\text{O}_2$ , to the corresponding calculated quantities. In the case of  $\text{O}_2$ , binding energy of 5.16 eV and bond length of 1.21 Å have been measured. Sasaki *et al.* obtained an equilibrium bond length of 1.24 Å. Honkala *et al.* calculated a binding energy of 5.3 eV and a bond length of 1.24 Å. Yourdshahyan *et al.* obtained a binding energy of 5.73 eV and a bond length of 1.24 Å.

In all these studies, the driving force for the dissociation is identified with charge transfer from the substrate to the  $2p\pi_g^*$  orbital of the molecule. According to Sasaki *et al.* and Yourdshahyan *et al.*, molecules approaching the surface in the *end-on* configuration should undergo abstractive chemisorption. They also found, that the *end-on* configuration is energetically favoured with respect to the *side-on* configuration, for molecule-surface distances from 3 Å to 2 Å. Closer to the surface, the situation is reversed and the *side-on* configuration is favoured. If the potential energy reduction of roughly 1.2 eV from the vacuum to this point is converted into translational energy, the molecule should reach a velocity of 27 Å/psec. The remaining distance from the surface should then be too small to allow reorientation of the molecular axis and the molecules should still approach the surface in the *end-on* configuration [Sasaki, 1999].<sup>1</sup> This effect has been proposed as the cause for an efficient steering of molecules approaching the surface, with their axis at an angle comprised between 0° and 30° with the surface normal [Yourdshahyan, 2001]. It is also consistent with the interpretation of the measured anticorrelation between  $\sigma_{\text{ab}}$  and molecular  $T_{\text{rot}}$  in terms of rotational hindering of the steering effect, presented in Section 5.4.2.

Sasaki *et al.* found evidence for direct dissociation, independently from the orientation of the molecular axis. Honkala *et al.* and Yourdshahyan *et al.* reported a barrier on the entrance channel of 200 meV, only for molecules approaching the surface in a *side-on* geometry, on the bridge site. The potential energy calculated by Honkala *et al.* are shown in Fig. 5.14. The effect of the different gradient corrections on the PEC is illustrated by the two sets of curves, termed according to the starting geometry of the incoming molecule. The lower set has been calculated applying the correction BP86 [Becke, 1988; Perdew, 1986]. The upper set has been determined using the revised Perdew-Burk-Ernzerhof gradient correction [Zhang, 1988]. The existence of the barrier depends on the chosen GGA. Österlund *et al.* reported a sticking probability of  $10^{-2}$  for thermal oxygen and an apparent activation energy of about 200 meV [Österlund, 1997]. Such barrier heights are at the limit of the current accuracy of the theory. Therefore, the lack of a general barrier in the computational results might be due to theoretical limitation. On the other hand, the measurement of an apparent activation energy does not necessary imply the existence of a dissociation barrier for the minimum energy pathway. In fact, a similar

---

1. This is consistent with the estimate of the velocity acquired by  $\text{O}_2$  molecules as a result of their interaction with alkali metal films [Greber, 1995].

effect could result from a reduced phase for the dissociation at low translational energies. For example, this would be the case if slow molecules could be efficiently steered into unfavorable portions of the potential hyper surface. At higher translational energies, faster molecules might dissociate for a wider range of initial orientation or places in the unit cell, while the steering effect would be less relevant. In this case, an increase of translational energy would induce an increase of  $S_0$  also in absence of an absolute barrier to the dissociation. Experimental evidences for the steering effect discussed in Section 5.4.2 hint, that such a mechanism might be active. Therefore, the theoretical findings are not necessarily conflicting with the experimental ones.

Yourdshahyan *et al.* systematically investigated the effect of the inclination of the molecular axis with respect to the surface normal, on the dissociation mechanism. They calculated the PES for incoming molecules in the *end-on* configuration, molecules with their axis inclined of  $30^\circ$  and  $60^\circ$  with respect to the surface normal and for molecules in the *side-on* configuration. The results of this study are displayed in Fig. 5.15. Whenever the molecule approached the surface in a configuration other than *side-on*, independently from the impact point on the surface unit cell, it had to overcome a relative maximum close to the bottom of the PES, before dissociation could be completed. This could lead to an intermediate molecularly chemisorbed state as a precursor to dissociation, provided that the molecule could dissipate the chemisorption energy efficiently enough. The existence of a molecular chemisorbed state has found no experimental support within low temperature UPS investigation (40K) of  $O_2/Al(111)$  and study of  $S_0$  as a function of the sample temperature [Hofmann, 1979; Österlund, 1997]. This indicates, that even if the PES corrugations exist, the energy dissipation processes are not efficient enough to allow trapping of the incoming molecules.

Another reason for the discrepancies between calculation and experiments might lie in the inability of DFT to accurately describe non-adiabatic phenomena. In DFT calculations the system always evolves on the ground state branch of the PES. This might be a

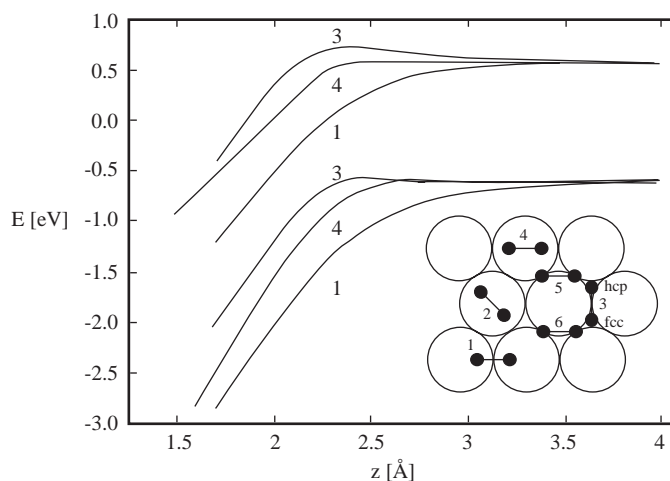


Fig. 5.14: The potential energy along the adsorption trajectories. The upper curves are calculated with RPBE and the lower curves with BP86. The zero energy level is the average of the potentials at 4 Å. The curves are labeled according to the numbering in the inset. The starting geometries: (1) top-bridge-top, (2) hcp-top, (3) hcp-fcc, (4) top-top, (5) hcp-hcp, and (6) fcc-fcc are indicated in the inset [Honkala, 2000].

severe limitation, since experimental findings and theoretical speculations suggest, that the  $O_2/Al(111)$  reaction might take place with the  $O_2$  evolving on excited-state portions of the potential energy hypersurface. Kasemo demonstrated that the initial stage of  $O_2$  chemisorption on Al is accompanied by emission of photons with a probability of  $10^{-7}$  per incident molecule. Spectral analysis revealed a broad emission band with maxima located at 510nm and 590nm [Kasemo, 1974]. This phenomenon has been interpreted in terms of non-adiabatic charge transfer reaction between the surface and the incoming molecule [Kasemo, 1979]. Katz *et al.* investigated the quantum dynamics interaction of  $O_2$  with three metals (Cs, Al and Ag), using a set of semi-empirical diabatic potentials [Katz, 1999]. The metals were only considered as electron donors. So their structural details were omitted and differentiation between the metal species was accounted for by differences in the workfunctions and in the heat of adsorption for  $O_2$ . These differences can significantly change the dissociation mechanism, leading to a long-range charge-transfer (*harpooning*) for metals with lower workfunctions [Gadzuk, 1985]. The dynam-

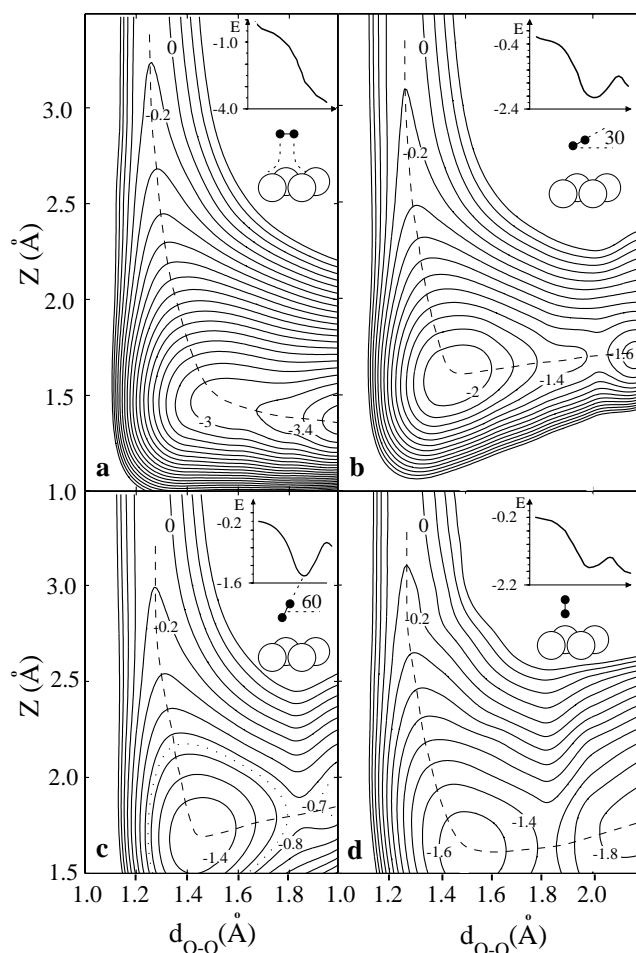


Fig. 5.15: Cuts through the six-dimensional PES for the interaction of  $O_2$  with Al(111).  $d_{O-O}$  is the bond length of  $O_2$ ,  $Z$  is the distance of the center of mass of the molecule from the surface. The molecule is located above the fcc site. The angles between the molecular axis and the surface are:  $0^\circ$  (a),  $30^\circ$  (b),  $60^\circ$  (c),  $90^\circ$  (d). The numbers in the equipotential contour are the energy values in eV measured from the energy of the totally separated  $O_2$  and Al(111) surfaces.

ics was solved by propagation of an initial wave function emerging from the gas phase, and the products were analyzed in terms of integrated fluxes in the different reaction channels. In this case too, theoretical evidence was found for a molecular chemisorbed state, as precursor to the dissociation. This is at variance with known experimental evidence.

Another possible non-adiabatic reaction is the rearrangement of the molecular spin upon chemisorption. The ground state of the O<sub>2</sub> molecule of the O atoms are spin-triplet. Hence, the molecule must undergo a spin-flip transition while approaching the surface, before dissociation at the surface can take place. In the works of Sasaki and Ohno, Honkala and Laasonen and Yourdshahyan *et al.*, the spin was treated as a continuous variable, whereas in reality this transition is quantized. In the O<sub>2</sub>/Al interaction, spin-flip transitions are possible by coupling of the incoming molecule with the magnetic field of the nuclei at the surface (*spin-orbit effect*). Since the magnetic moment of the Al nuclei is weak, a retarded spin-flip transition might ensue, which could result in a non-adiabatic transition.

## 5.6 TOWARD A REACTION MODEL

At this point I will try to summarize the experimental and theoretical findings and rationalize them into a scenario for the dissociative chemisorption in the low coverage regime.

- The dissociative chemisorption of O<sub>2</sub> on Al(111) shows an apparent activation energy of approximately 200 meV. The initial sticking coefficient  $S_0$  is strongly dependent on the translational energy of the incoming molecules, varying from  $(1.4 \pm 0.5) \cdot 10^{-2}$  at 24 meV to  $0.90 \pm 0.04$  above 600 meV [Österlund, 1997].
- Both UPS investigation of O<sub>2</sub>/Al(111) at low temperature (40 K) and study of  $S_0$  as a function of the sample temperature rule out the existence of a molecular physisorbed state as a precursor for the dissociative chemisorption [Hofmann, 1979; Österlund, 1997].
- The REMPI data in this work demonstrate the availability of an abstractive chemisorption pathway for incoming O<sub>2</sub> molecules with  $E_{\text{trans}}$  between 90 meV and 450 meV. Apparent activation energies have been determined, that grow with the rotational excitation of the incoming molecules [Table 5.1].
- The interpretation of the isolated features in the Room-Temperature STM pictures, taken after exposure of Al(111) to O<sub>2</sub> from the background by Brune and coworkers, is still controversial. Anyway, all of the available STM data are consistent with the existence of an abstractive chemisorption pathway for the chemisorption reaction.
- The STM detection of isolated O-atoms, dimers and trimers at  $E_{\text{trans}}(\text{O}_2) = 500$  meV, together with the REMPI data at the higher available  $E_{\text{trans}}(\text{O}_2)$ , show that both abstractive (*end-on* configuration) and *normal* (*side-on* configuration) chemisorption channels are open at such translational energies, consistently with the increase in  $S_0$  [Binetti, 2000]. Evidence has been found for a steep increase in the number of dimers as compared to the numbers of monomers, as a function of the translational energy of the incoming O<sub>2</sub> [Komrowski, 2001].

- Details relative to the partitioning of the abstraction exothermicity and the dynamics of the chemisorption reactions can be inferred by analogies with similar systems, namely the interaction of electronegative gases (halogens,  $O_2$ ) with semiconductor and alkali metal surfaces. Such systems have been intensively studied both theoretically and experimentally, and are quite well understood [Jensen,1995; Strömquist,1996; Greber,1997; Katz,1999]. Chemisorption is believed to start with a resonant charge transfer from the substrate to the affinity level ( $E_A$ ) of the incoming molecule. As shown in Eq. 5.1, this charge transfer can occur when the molecule is still far away from the surface, depending on the workfunction of the metal and on the size of  $E_A$ . Closer to the surface, a second charge transfer takes place and the molecule dissociates. If the final charge transfer takes place with the molecule in an upright geometry, repulsive Coulomb forces may lead to the ejection of the outer fragment. This may neutralize while leaving the reaction region. Non-adiabaticity might play a role in the charge transfer processes.
- All of the potential energy surfaces proposed to model the  $O_2/Al(111)$  interaction show no evidence for a generalized barrier to dissociative chemisorption in the entrance channel [Sasaki,1999; Honkala,2000; Yourdshahyan,2001].
- The existence of a 200meV barrier has been recently predicted, limited to molecules approaching the surface in a *side-on* geometry on a bridge site [Honkala,2000; Yourdshahyan,2001]. The works of Sasaki *et al.* and Yourdshahyan *et al.* show, that the *end-on* approach is energetically favoured with respect to the *side-on* one, and that the incoming molecule should be funneled into an upright geometry. Charge transfer from the substrate should be the driving force for the dissociation mechanism. Abstraction was predicted.

The following scenario for the abstractive chemisorption process can be proposed. As a result of the surface-molecule interaction,  $O_2$  in the rotational ground state can be steered and approach the aluminum surface in an upright configuration. At the same time, two electron transfers occurring in rapid succession cause the dissociation of the incoming molecule. The fragment closer to the surface is chemisorbed. The other one is too far away from the surface to form a bond when dissociation takes place and can permanently escape the reaction region. This mechanism is most efficient for thermal molecules in the low lying rotational states ( $J \approx 0$ ), with their axis at angles less than  $30^\circ$  with respect to the surface normal. If  $T_{rot}$  of the gas is increased, the  $J=0$  state is depopulated. Molecules in higher rotational states cannot be efficiently steered because their rotational energy is comparable to (or even higher than) the steering energy. A decrease of  $\sigma_{ab}$  or, alternatively, an increase in the apparent activation energy for abstraction, results. The order of magnitude of the steering effect can be inferred by comparison with  $\Delta E_{rot}$ . The abstraction probability increases exponentially with the translational energy of the incoming molecules, for energy between 90meV and 500meV. This is in analogy with the known behaviour of the sticking coefficient, in the same energy range [Österlund, 1997]. Non-adiabatic effects due to retarded charge transfer and spin conversion might explain the stark dependency of both  $S_0$  and  $\sigma_{ab}$  on the translational energy of the incoming  $O_2$  molecules.

The charge transfer probability for  $O_2$  and  $O_2^-$  depends on their orientation with respect to the surface, and it is reduced when the surface is approached in a *side-on* geometry [Teillet-Billy,1995]<sup>1</sup>. Hence, before charge transfer can take place, either a

molecule or a molecular ion in this configuration must get closer to the surface than its *end-on* counterpart. The strongly repulsive core of the interaction potential could prevent *side-on* species from accessing a region where resonant ionization would be possible. This might explain the inhibition of dissociative chemisorption of molecules approaching the surface *side-on* at low  $E_{\text{trans}}$ .

At higher translational energies the coexistence of chemisorbed monomers and dimers show that ordinary chemisorption of *side-on* molecules is viable. Opening of this new reaction channel does not suppress the preexisting abstractive one. Accordingly, the sticking coefficient increases, until the saturation value of approximately 0.9 is reached.

In this scenario, the positive correlation between  $S_0$  and translational molecular energy is not necessarily correlated to the existence of an absolute barrier to the dissociation.

- 
1. The symmetry of the system composed by the molecule and the surface depends on the axis orientation. For a molecule in an upright configuration the system is invariant by rotation around its axis and the molecular symmetry is preserved. For other orientations, only the plane containing the molecular axis and perpendicular to the surface is a symmetry element. The two components of the doubly degenerate  ${}^2\Pi_g$  state of the negative molecular (superoxo) ion, mix together to form two states, one symmetric and the other antisymmetric with respect to that state. The symmetric component is significantly less coupled to the surface than its antisymmetric counterpart, whose coupling is comparable to that of the two components in the perpendicular geometry. This results in a reduced charge transfer for  $\text{O}_2$  approaching the surface in a *side-on* geometry.

## 6. CONCLUDING REMARKS

In this work, the dynamics of the initial stage of dissociative chemisorption of  $O_2$  on an Al(111) surface has been investigated and the existence of an abstraction pathway for the reaction has been demonstrated. This reaction, of both scientific and technical relevance, has been intensively studied both theoretically and experimentally in the last thirty years.

$O_2$  chemisorbs dissociatively on Al(111) at low coverages. It is generally agreed that the O-atoms occupy the *fcc* hollow sites located  $(0.7 \pm 0.1) \text{ \AA}$  from the outermost Al layer, with no evidence for a subsurface adsorption site. The chemisorption is a strongly activated process, with  $S_0$  steeply rising from  $(1.4 \pm 0.5) \cdot 10^{-2}$  at  $E_{\text{trans}} = 24 \text{ meV}$ , to an almost constant value of  $0.90 \pm 0.04$  at  $E_{\text{trans}}$  between 600 meV and 2000 meV. Nevertheless, no evidence for a generalized barrier to chemisorption has yet been theoretically found. STM studies of  $O_2$  chemisorption at variable  $E_{\text{trans}}(O_2)$  show the coexistence of monomers with dimers and higher coordination features. These have been interpreted as isolated O-atoms and higher coordination islands on the metal surface. The originally proposed explanation for the existence of isolated O-atoms, in terms of high mobility of hyperthermal species, has been rejected both on theoretical and experimental basis.

In this work, the existence of an abstractive chemisorption pathway for an Al(111) surface interacting with  $O_2$  from a molecular beam has been demonstrated by means of laser spectrometric techniques (REMPI). This explains naturally the occurrence of individually chemisorbed O-atom. The chemisorption dynamics has been investigated by means of REMPI and REMPI-ToF techniques and the role played by both translational and rotational degrees of freedom in the reaction has been highlighted.

Based on the present data, recent STM studies and theoretical calculations, the following scenario is proposed to explain the main features of the dissociative chemisorption process. It is convenient to discuss the effects of the translational and rotational degrees of freedom of  $O_2$  molecules on their dissociative chemisorption on an Al(111) surface, in terms of a low-energy and a high-energy regime. In the low-energy regime, both the rotational and the translational degrees of freedom of the incoming molecule are relevant in determining the outcome of its interaction with the surface. A steering effect is at work, that aligns the axis of the incoming molecules with the surface normal, if the angle between them is less than  $30^\circ$ . Dissociative chemisorption takes place in a reduced phase space, where only molecules approaching with their axis close to the surface normal may dissociate.

In the high-energy regime the importance of the steering effect is reduced because the steering force acts on the faster molecules for a shorter time. Moreover, these molecules can probe a wider portion of the PES. Hence, more phase space becomes available and a larger variety of dissociating trajectories are possible. As a result, dissociation of molecules approaching the surface in a *side-on* geometry becomes also viable, and chemisorbed oxygen dimers can be detected.

The stark dependency of both  $S_0$  and  $\sigma_{\text{ab}}$  on the translational energy of the incoming  $O_2$  molecules might result from the existence of non-adiabatic effects due to retarded charge transfer and spin conversion.

Further theoretical work, possibly including non-adiabatic effects and a real dynamic simulation of the process, and a systematic STM study of the onset and evolution of the frequency of dimer occurrence as a function of the molecular beam energy could foster the understanding of dissociative chemisorption.

## APPENDIX A

### List of the acronyms used in the text:

**AES:** Auger Electron Spectroscopy  
**ATI:** above threshold ionization  
 **$\beta$ -BBO or BBO:** Beta-Barium Borate ( $\beta$ -BaB<sub>2</sub>O<sub>4</sub>) crystal  
**BOA:** Born-Oppenheimer approximation  
**CF:** ConFlat  
**DC:** direct current  
**DFT:** Density Functional Theory  
**EAL:** emission attenuation length  
**FWHM:** Full Width at Half Maximum  
**GGA:** general-gradient approximation  
**HOMO:** Highest Occupied Molecular Orbital  
**HV:** High Vacuum  
**IMFP:** inelastic mean free path  
**LDA:** Local Density Approximation  
**LEED:** Low Electron Energy Diffraction  
**MCP:** Multi-Channel Plates  
**MED:** mean escape depth  
**Nd:YAG :** Neodymium-doped Yttrium-Aluminum-Garnet  
**NES:** Normal Energy Scaling  
**PEC:** Potential Energy Curve  
**PES:** potential energy surface  
**q/m:** charge-to-mass ratio  
**QMS:** Quadrupole Mass Spectrometer  
**Q-switch:** electro-optic switch  
**REMPI:** Resonantly Enhanced Multi-Photon Ionization  
**SHG:** Second Harmonic Generator  
**STM:** Scanning Tunneling Microscopy  
**ToF:** Time-of-Flight  
**TTL:** Transistor-Transistor-Logic  
**UHV:** ultrahigh vacuum  
**UV:** Ultra Violet

## APPENDIX B

### List of the symbols used in the text:

- #: number of photons
- (i,j,k): Miller indexes
- °: decimal degrees [angle]
- a.u.: atomic units
- Å: Angstrom [ $10^{-10}$ m]
- $a_s$ : nearest neighbour spacing, 2.86 Å for Al(111)
- $B$ : dimensionless collision parameter
- $C_p$ : heat capacity of the gas at constant pressure
- $d$ : source diameter
- $d_{\text{sep}}$ : mean separation of adatoms
- $E_A$ : affinity level of the incoming molecule
- $E_{\text{act}}$ : activation energy
- $E_{\text{chem}}$ : chemisorption energy
- $E_{\text{diss}}$ : dissociation energy
- $e-h$ : electron-hole pairs
- $\mathbf{E}_i$ : electric fields [V/m]
- $E_{\text{prec}}$ : physisorption energy
- $E_{\text{th}}$ : thermal energy
- $E_{\text{trans}}$ : translational energy
- eV: electron volt [energy]
- $f$ : focal length
- Hz: Hertz [frequency]
- $I$ : signal intensity
- $I_t$ : tunneling voltage
- $J(X)$ : flux of particles of the species X
- J: Joule [energy]
- K/s: Kelvin/second [heating rate]
- $k$ : Boltzmann constant [J/K]
- K: Kelvin degree [Temperature]
- KLL, LMM: electronic shells for Auger transition
- l/s: liter/second [pumping speed]
- $l$ : wavelength [nm]
- $lN_2$ : liquid nitrogen
- $M^2$ : laser quality factor
- mbar: pressure
- ML: Monolayer (the ratio of the no. of adsorbed species per unit surface area to the no. of surface substrate atoms per unit area)
- MS/s:  $10^6$ sample/second
- $n$ : order of the photoinduced process
- $n_0$ : source density
- $n_{\text{O-atoms}}$ : number density of O-atoms in the probe volume
- $P(X)$ : partial pressure of the species X
- $p_j$ : occupation probability of rotational states for a gas
- $p_v$ : occupation probability of vibrational levels
- s, p, d: electron orbitals

$S_{//}$ : parallel terminal speed ratio  
 $S_0$ : initial sticking coefficient  
 $S_\alpha$ : seeding  
 $t_{\text{flight}}$ : flight time [s]  
 $T_{\text{gas}}$ : gas temperature [K]  
 $T_{\text{nozzle}}$ : nozzle temperature  
 $T_{\text{rot}}$ : rotational temperature  
 $T_s$ : surface temperature  
 $T_{\text{vib}}$ : vibrational temperature of a gas  
 $v(X)$ : velocity of the species X [m/s]  
 $\nu$ : vibrational quantum number  
 $V$ : voltage  
 $V_L^{\text{act}}$ : laser active volume  
 $V_t$ : tunneling voltage  
 $W$ : width of the distribution of the activation barrier heights  
 $w_0$ : beam waist (radius)  
 $z_R$ : Rayleigh range or confocal parameter  
 $Z_R$ : rotational number of a gas  
 $Z_{\text{rot}}$ : rotational partition function  
 $Z_{\text{vib}}$ : vibrational partition function of a gas  
 $\emptyset$ : diameter  
 $\Delta(T_s)$ : energy exchange at a given surface temperature  
 $\Delta E$ : reaction exothermicity [eV]  
 $\Delta\lambda$ : linewidth [nm]  
 $\Delta\nu$ : bandwidth [ $\text{cm}^{-1}$ ]  
 $\Delta V$ : voltage drop  
 $\Phi$ : laser fluence  
 $\mu$ : mass ratio  $m/M$   
 $\Theta$ : coverage [ML]  
 $\theta_i$ : incidence angle  
 $\sigma^{(2)}$ : 2-photon ionization cross section  
 $\Sigma$ : detection efficiency  
 $\sigma_{\text{ab}}$ : abstraction probability  
 $\sigma_{\text{pi}}$ : photoionization cross section  
 $\Omega$ : FWHM of the time of arrival distribution for O-atoms generated in the abstraction process  
 $\Omega_{\text{exp}}$ : measured FWHM of the O-signal due to abstraction at the surface

**REFERENCES**

- Alonso, M. and E. J. Finn (1968), "*Fundamental university physics - III Quantum and statistical physics*", Addison-Wesley, Reading, Mass.
- Amirav, A. and M. J. Cardillo (1986), "*Electron-hole pair creation by atomic scattering at surfaces*", Phys. Rev. Lett. **57**, 2299.
- Ashcroft, N. W., N. D. Mermin (1981), "*Solid State Physics*", Saunders College, Philadelphia, Penn.
- Bamford, D. J., L. E. Jusinski and W. K. Bischel (1986), "*Absolute two-photon absorption and three-photon ionization cross sections for atomic oxygen*", Phys. Rev. A **34**, 185.
- Bamford, D. J., M. J. Dyer and W. K. Bischel (1987), "*Single-Frequency measurements of two-photon cross sections and Doppler-free spectra for atomic oxygen*", Phys. Rev. A **36**, 2497.
- Bartolucci, F., R. Franchy, J. C. Barnard and R. E. Palmer (1998), "*Two chemisorbed species of O<sub>2</sub> on Ag(110)*", Phys. Rev. Lett. **80**, 5224.
- Bass A. M, A. E. Ledford Jr. and A. H. Laufer (1976), "*Extinction coefficients of NO<sub>2</sub> and N<sub>2</sub>O<sub>4</sub>*", J. of Research of the National Bureau of Standard **80A**, 143.
- Batra, I. and L. Kleinman (1984), "*Chemisorption of oxygen on aluminum surfaces*", J. Electron Spectrosc. Relat. Phenom. **33**, 175.
- Baule, B. (1914), Ann. Phys. **44**, 145.
- Beijerinck, H., P. Menger and N. Verster (1979), *11th RGD* **2**, 871.
- Beijerinck, H. and N. Verster (1981), "*Absolute intensities and perpendicular temperatures of supersonic beams of polyatomic gases*", Physica **111C**, 327.
- Beijerinck, H., G. Kaashoek, G. Beijers and M. Verheijen (1983), "*Non-maxwellian velocity distributions in the transition region of supersonic expansions of the noble gases He, Ne and Ar*", Physica **121C**, 425.
- Becke, A. D. (1988), "*Density-functional exchange-energy approximation with correct asymptotic behavior*", Phys. Rev. A **38**, 3098.
- Binetti, M., O. Weiße, E. Hasselbrink, A. J. Komrowski and A. C. Kummel (2000), "*Abstractive chemisorption of O<sub>2</sub> on Al(111)*", Faraday Disc. Chem. Soc. **117**, 313.
- Bornscheuer, K.-H. (1997), "*Mehrdimensionale Reaktionsdynamik am Beispiel der Photororption von Ammoniak*", Dissertation im Fachbereich Chemie, FU-Berlin.
- Brako R., D. M. Newns (1989) "*Theory of electronic processes in atom scattering from surfaces*", Rep. Prog. Phys. **52**, 655.
- Brune, H., J. Wintterlin, R.J. Behm and G. Ertl (1992), "*Surface migration of 'hot' adatoms in the course of dissociative chemisorption of oxygen on Al(111)*", Phys. Rev. Lett. **68**, 624.

- Brune, H., J. Winterlin, J. Trost and G. Ertl, J. Wiechers and R.J. Behm (1993), “*Interaction of oxygen with Al(111) studied by scanning tunneling microscopy*”, J. Chem. Phys. **99**, 2128.
- Budde, F. (1988), “*Dynamik der Streuung und laserinduzierten Desorption im System NO/Ni(100)*”, Dissertation im Fachbereich Chemie, FU-Berlin.
- Bujisse, B., W. J. van der Zande, A. T. J. B. Eppink, D. H. Parker, B. R. Lewis and S. T. Gibson (1998), “*Angular distribution for photodissociation of O<sub>2</sub> in the Herzberg continuum*”, J. Chem. Phys. **108**, 7229.
- Calvert, J. G. and J. N. Pitts (1966), “*Photochemistry*”, J. Wiley, New York.
- Capiluppi, C., D. Postpischl and P. Randi (1978), “*Introduzione alla elaborazione dei dati sperimentali*”, CLUEB, Bologna.
- Carlisle C.I., T. Fujimoto, W. S. Sim and D. A. King (2000), “*Atomic imaging of the transition between oxygen chemisorption and oxide film growth on Ag{111}*”, Surf. Sci. **470**, 15.
- Chiang T-C., G. Kaindl and D. E. Eastman (1980), “*Photoemission from physisorbed CO on clean and Xe-covered Al(111)*”, Solid State Commun. **36**, 25.
- Darling, G. R. and S. Holloway (1994), “*The dissociation of diatomic molecules at surfaces*”, Rep. Prog. Phys. **58**, 1595.
- Darling, G. R. and S. Holloway (1995), “*The role of parallel momentum in the dissociative adsorption of H<sub>2</sub> at highly corrugated surfaces*”, Surf. Sci. **304**, L461.
- Davies, L. E., N. C. MacDonald, P. W. Pamberg, G. E. Risch and R. E. Weber (1976), “*Atlas of Auger Electron Spectroscopy*”, Perkin Elmer Corp., Physical Electronics Div., Eden Prairie, Minn.
- Davis, J. E. and C. B. Mullins (1997) “*Adsorption mechanisms of translationally-energetic O<sub>2</sub> and N<sub>2</sub>: direct dissociation versus direct molecular chemisorption*”, Surf. Sci. Lett. **380**, L513.
- Deézsi, I. (1958), “*Novy vrashchatelny analiz g-Polos NO molekuly (A recent rotational analysis of the  $\gamma$  bands of the NO molecule)*”, Acta Phys. Hung. **9**, 125.
- Delone, N. B., V. P. Krainov (1999), “*ac Stark shift of atomic energy levels*”, Usp. Fiz. Nauk [Phys. Usp.] **42**, 669.
- de Meijere, A. (1993), “*Dynamik elementarer chemischer und photochemischer Reaktionen an Pd(111)*”, Dissertation im Fachbereich Chemie, FU-Berlin.
- De Santis, L. and R. Resta (2000), “*Electron localization at metal surfaces*”, Surf. Sci. **450**, 126.
- Engel, T. (1978), “*A molecular beam investigation of He, CO, and O<sub>2</sub> scattering from Pd(111)*”, J. Chem. Phys. **69**, 373.
- Engdahl, C. and G. Wahnström (1994), “*Transient hyperthermal diffusion following dissociative chemisorption: a molecular dynamics study*”, Surf. Sci. **312**, 429.
- Gadzuk J. W. (1985), “*Surface harpooning*”, Com. At. Mol. Phys. **16**, 219.

- Gartland, P. O. (1977), "Adsorption of oxygen on clean single crystal faces of aluminum", *Surf. Sci.* **62**, 183.
- Gland, J. L., B. A. Sexton and G. B. Fisher (1980), "Oxygen interactions with the Pt(111) surface", *Surf. Sci.* **95**, 587.
- Greber, T., A. Morgante, S. Fichtner-Endruschat and G. Ertl (1995), "On the dissociation of O<sub>2</sub> on alkali metals", *Surf. Rev. and Lett.* **2**, 273.
- Greber, T. (1997), "Charge-transfer induced particle emission in gas surface reactions", *Surf. Sci. Rep.* **28**, 1 and references therein.
- Gross A. (1998), "Hydrogen dissociation on metal surfaces - a model system for reactions on surfaces", *Appl. Phys. A* **A67**, 627.
- Gross A. (2001), private communication.
- Guthrie W. L., T.-H. Lin, S. T. Ceyer and G. A. Somorjai (1982), "The angular and velocity distributions of NO scattered from the Pt(111) crystal surface", *J. of Chem. Phys.* **76**, 6398.
- Hagena, O. F. (1981), "Nucleation and growth of clusters in expanding nozzle flows", *Surf. Sci.* **106**, 101.
- Hall, J., O. Saksager and I. Chorkendorff (1993), "Dissociative chemisorption of O<sub>2</sub> on Cu(100). Effects of mechanical energy transfer and recoil", *Chem. Phys. Lett.* **216**, 413.
- Hammer, B., M. Scheffler, K. W. Jacobsen and J. K. Nørskov (1994), "Multidimensional potential energy surface for H<sub>2</sub> dissociation over Cu(111)", *Phys. Rev. Lett.* **73**, 1400.
- Harris, J. (1989), "On vibrationally-assisted dissociations of H/sub 2/ at metal surfaces", *Surf. Sci.* **221**, 335.
- Hayden, B. E. and C. L. A. Lamont (1989), "Coupled translational-vibrational activation in dissociative hydrogen adsorption on Cu(110)", *Phys. Rev. Lett.* **63**, 1823.
- Henkelman G. and H. Jónsson (2001) "Theoretical Calculations of Dissociative Adsorption of CH<sub>4</sub> on an Ir(111) Surface", *Phys. Rev. Lett.* **84**, 664.
- Hodgson, B. A. and J. C. Polanyi (1971), "Location of energy barriers. IV. Effect of rotation and mass on the dynamics of reactions A+BC", *J. of Chem Phys.* **55**, 4745.
- Hofmann, P., K. Horn, A. M. Bradshaw and K. Jacobi (1979), "The adsorption and condensation of oxygen on aluminum at low temperature", *Surf. Sci. Lett.* **82**, L610.
- Honkala, K. and K. Laasonen (2000), "Oxygen molecule dissociation on the Al(111) surface", *Phys. Rev. Lett.* **84**, 705.
- Huber, K. P. and G. Herzberg (1979), "Molecular spectra and molecular structure constants of diatomic molecules", Van Nostrand, New York.
- Hult, E., H. Rydberg, B. I. Lundqvist and D. C. Langreth (1999), "Unified treatment of asymptotic van der Waals forces", *Phys. Rev. B* **59**, 4708.

- Jacobi, K., C. Astaldi, P. Geng and M. Bertolo (1989) “*Physisorption of  $N_2$  and CO on Al(111): a combined HREELS-UPS investigation*”, Surf. Sci. **223**, 569.
- Jacobsen, J., B. Hammer, K. W. Jacobsen and J. K. Nørskov (1995), “*Electronic structure, total energies and STM images of clean and oxygen covered Al(111)*”, Phys. Rev. B **52**, 14954.
- Jensen, J., C. Yan and A. C. Kummel (1995), “*Energy dependence of abstractive vs. dissociative chemisorption of fluorine molecules on the silicon (111)-(7×7) surface*”, Science **267**, 493.
- Kasemo, B. (1974), “*Photon emission during chemisorption of oxygen on Al and Mg surfaces*”, Phys. Rev. Lett. **32**, 1114.
- Kasemo, B., Tornqvist E., Norskov J. K. and Lundqvist B.I. (1979) “*Photon and electron emission as indicators of intermediate states in surface reactions*”, Surf. Sci. **89**, 554.
- Katz, J., Y. Zehiri, and R. Kosloff (1999), “*Non-adiabatic charge transfer process of oxygen on metal surfaces*”, Surf. Sci. **425**, 1.
- King, D. A. (1998), “*Femtomole adsorption calorimetry on single crystal surfaces*”, Chem. Revs. **98**, 797.
- Kleyn, A. W., D. A. Butler, A. Raukema (1996), “*Dynamics of the interaction of  $O_2$  with silver surfaces*”, Surf. Sci. **363**, 29.
- Knuth, E. L. (1977), “*Dimer-formation rate coefficients from measurements of terminal dimer concentrations in free-jet expansions*”, J. Chem. Phys. **66**, 3515.
- Kolasinski, K. W., F. Cemic and E. Hasselbrink (1994), “ *$O_2/Pd(111)$ . Clarification of the correspondence between thermal desorption features and chemisorption states*”, Chem. Phys. Lett. **219**, 113.
- Komrowski, A. J. (2000), private communication.
- Komrowski, A. J., J. Z. Sexton and A.C. Kummel, M. Binetti, O. Weiße and E. Hasselbrink (2001), “*Oxygen Abstraction from Dioxygen on the Al(111) surface*”, in preparation.
- Krenzen, E. (1999), “*REMPI spectroscopy of oxygen atoms*”, M. Sc. Thesis, Fysisk Institut, Odense Universitet, Odense, Denmark.
- Lang, N. D. and A. R. Williams (1978), “*Theory of atomic chemisorption on simple metals*”, Phys. Rev. B **18**, 616.
- Larsen, R. A., S. K. Neoh and D. R. Herschbach (1974), “*Seeded supersonic alkali atom beams*”, Rev. of Sci. Instr. **45**, 1511.
- Laß, K. (2001), private communication.
- Lennard-Jones, J.(1932), “*Processes of adsorption and diffusion on solid surfaces*”, Trans. Faraday Soc. **28**, 333.
- Leonardelli, G. , E. C. D. Gruber, M. Schmid, P. Varga (2000), *Verhandl. DPG* **35**, 736.
- Li, Y. L., D. P. Pullman, J. J. Yang, A. A. Tsekouris, D. B. Gosalvez, K. B. Laughlin, Z. Zhang, M. T. Schulberg, D. J. Gladstone, M. McGonigal and S. T. Ceyer (1995),

- “Experimental verification of a new mechanism for dissociative chemisorption: atom abstraction”*, Phys. Rev. Lett. **74**, 2603
- McEwan, M. J. and L.F. Phillips (1985), *“Chemistry of the atmosphere”*, Edward Arnold, London.
- Michel, R., J. Gastaldi, C. Allasia, C. Jourdan and J. Derrien (1980), *“Initial interaction of oxygen with aluminium single crystal faces: a LEED, AES and Workfunction study”*, Surf. Sci. **95**, 309.
- Michelsen, H. A. and D. J. Auerbach (1991), *“A critical examination of data on the dissociative adsorption and associative desorption of hydrogen at copper surfaces”*, J. Chem. Phys. **94**, 7502.
- Miller, D. R. (1988), *“Free jet sources”*, in *“Atomic and molecular beam methods”*, Editor G. Scoles, Oxford University Press.
- Mitrovic, B. C. and D. J. Connor (1998), *“Negative direct recoil spectroscopy study of the initial oxidation of Al(111)”*, Surf. Sci. **405**, 261.
- Nessler, W. (1996), *“Dynamik von Oberflächenreaktionen”*, Dissertation im Fachbereich Chemie, FU-Berlin.
- Nienhaus, H., H. S. Bergh, B. Gergen, A. Majumdar, W. H. Weinberg and E. W. McFarland (2000), *“Direct detection of electron-hole pairs generated by chemical reactions on metal surfaces”*, Surf. Sci. **445**, 335.
- Nienhaus, H. (2001), *“Direkter Nachweis von nicht-adiabatischer Energiedissipation bei chemischen Reaktionen an Metalloberflächen”*, Verhandl. DPG **35**, 362.
- NIST-National Institute For Standard and Technology, *“Electron-Impact Ionization Cross Section Database”* (<http://physics.nist.gov/PhysRefData/Ionization/>)
- Normand, D., C. Cornaggia, J. Lavancier, J. Morellec and H.X. Liu (1991), *“Multielectron dissociative ionization of O<sub>2</sub> in an intense picosecond laser field”*, Phys. Rev. A **44**, 475.
- Österlund, L., I. Zoric and B. Kasemo (1997), *“Dissociative sticking of O<sub>2</sub> on Al(111)”*, Phys. Rev. B **55**, 15452.
- Österlund, L. (1997) *“Elementary surface processes on graphite and aluminum”*, PhD Thesis at the Department of Applied Physics of the Chalmers University of Technology, Göteborg, Sweden.
- Perdew, J. P. (1986), *“Density-functional approximation for the correlation energy of the inhomogeneous electron gas”*, Phys. Rev. B **33**, 8822.
- Pettus, K. A., T. S. Ahmadi, E. J. Lanzendorf and A. C. Kummel (1999), *“Comparison of chemical selectivity and kinetic energy release in Si<sub>(s)</sub> + ICl<sub>(g)</sub> and H<sub>(g)</sub> + ICl<sub>(g)</sub>”*, J. Chem. Phys. **110**, 4641.
- Pettus, K. A., P. R. Taylor and A. C. Kummel (2000), *“Chemical selectivity in the remote abstractive chemisorption of ICl on Al(111)”*, Faraday Disc. Chem. Soc. **117**, 321.
- Pölzl, H., G. Strohmeier and A. Winkler (1999) *“Adsorption and abstraction of H(D) on clean and modified Al(111) and Ni(111) surfaces”*, J. Chem. Phys. **110**, 1154.

- Poulsen, P., D. R. Miller (1977), "*The energy balance and free-jet expansions of polyatomics*", 10th RGD, **1**, 135.
- Powell, C. J., A. Jablonski, I. S. Tilinin, S. Tanuma and D. R. Penn (1999) "*Surface sensitivity of Auger-electron spectroscopy and X-ray photoelectron spectroscopy*", J. of El. Spectr. **98–99**, 1.
- Rettner, C. T., D. J. Auerbach and H. A. Michelsen (1992) "*Observation of direct vibrational excitation in collisions of H<sub>2</sub> and D<sub>2</sub> with a Cu(111) surface*", Phys. Rev. Lett. **68**, 2547.
- Richter, R. C., V. I. Khamaganov and A. J. Hynes (2000), "*Correlated photofragment product distributions in the photodissociation of NO<sub>2</sub> at 212.8 nm*", Chem. Phys. Lett. **319**, 341.
- Sasaki, T. and T. Ohno (1999), "*Calculation of the potential energy surface for dissociation process of O<sub>2</sub> on the Al(111) surface*", Phys. Rev. B **60**, 7824.
- Schmid, M., G. Leonardelli, R. Tscheließnig, A. Biedermann and P. Varga (2001), "*Oxygen adsorption on Al(111): low transient mobility*", Surf. Sci. Lett. **478**, L355.
- Schintke S., S. Messerli, K. Morgenstern, J. Nieminen and W.-D. Schneider (2001), "*Far-ranged transient motion of "hot" oxygen atoms upon dissociation*", J. Chem. Phys. **114**, 4206.
- Self, S. A. (1983), "*Focusing of spherical Gaussian beams*", Appl. Opt. **22**, 658.
- Steinfeld, J. I. (1985), "*Molecules and radiation*", MIT press, Cambridge (USA).
- Strömquist, J., L. Hellberg, B. Kasemo, B. I. Lundqvist (1996), "*Ballistic motion and abstraction in dimer dissociation at surfaces: Cl<sub>2</sub> on K*", Surf. Sci. **352–354**, 435.
- Sun H. (1998), "*Thin lens equation for a real laser beam with weak lens aperture truncation*", Optical Engineering **37**, 2906.
- Sur, A., R. S. Friedman and P. J. Miller (1991), "*Rotational dependence of the Rydberg-valence interaction in the IPg states of molecular oxygen*", J. Chem. Phys. **94**, 1705.
- Teillet-Billy D., B. Bahrim, J. P. Gauyacq (1995), "*Multi-electron and multi-state effects in the charge transfer processes between oxygen and metal surfaces*", Nucl. Instr. Methods **100**, 296.
- Trost, J., Brune H., Wintterlin J., Behm R. J. and Ertl G. (1998) "*Interaction of oxygen with Al(111) at elevated temperatures*", J. Chem. Phys. **108**, 1740.
- Uselman, W. M., E. K. C. Lee (1976), "*A study of nitrogen dioxide 2<sup>2</sup>B<sub>2</sub> photodecomposition to O(<sup>1</sup>D) and NO(<sup>2</sup>Π) in its second predissociation region 2500-2139Å*", J. Chem. Phys. **65**, 1948.
- Ustaze, S., S. Lacombe, L. Guillemot, V. A. Esaulov, M. Canepa (1998), "*Electron transfer on oxygen-covered Ag(110) and Al(111) surfaces: work function versus local electronic effects*", Surf. Sci. Lett. **414**, 938.
- Yourdshahyan, Y., B. Razaznejad and B. I. Lundqvist (2001), "*Adiabatic Potential-Energy Surface of O<sub>2</sub>/Al(111): Rare Entrance-Channel Barriers but Molecularly Chemisorbed State Apt for Abstraction*", Solid State Comm. **117**, 531.

- Wahnström, G., A. Lee and J. Strömquist (1996), “*Motion of ‘hot’ oxygen atoms on corrugated metal surfaces*”, J. Chem. Phys. **105**, 326.
- Wayne, R. P. (1991), “*Chemistry of atmospheres*” second edition, pp. 82-86 and 91-92, Oxford, Clarendon Press.
- Weiß, O. (2000), “*Aufbau eines hypertermischen Molekularstrahls und seine Anwendung zur Messung der Streuung von Sauerstoffmolekülen an Al(111)*”, Diploma im Fachbereich Chemie, Universität Essen, and references therein.
- Weiß, O. (2001), private communication.
- Wheeler, M. C., D. C. Seets and C. B. Mullins (1996), “*Kinetics and dynamics of the initial dissociative chemisorption of oxygen on Ru(001)*”, J. Chem. Phys. **105**, 1572.
- White, I. D., R. W. Godby, M. M. Rieger and R. J. Needs (1998), “*Dynamic image potential at an Al(111) surface*”, Phys. Rev. Lett. **80**, 4265.
- Whitten J. L. and H. Yang (1996), “*Theory of chemisorption and reactions on metal surfaces*”, Surf. Sci. Rep. **24**, 59.
- Winterlin, J. (1988), “*Struktur und Reaktivität einer Metalloberfläche - eine Untersuchung mit dem Rastertunnelmikroskop am System Al(111)/Sauerstoff*”, Dissertation im Fachbereich Chemie, FU-Berlin.
- Winterlin, J., R. Schuster and G. Ertl (1996), “*On the existence of a ‘hot’ atom mechanism for the dissociation of O<sub>2</sub> on Pt(111)*”, Phys. Rev. Lett. **77**, 123.
- Zel’dovich, Ya. B. (1973), “*Scattering and emission of a quantum system in a strong electromagnetic wave*”, Usp. Fiz. Nauk **110**, 139 [Sov. Phys. Usp. **16**, 427 (1973)].
- Zimmermann, F. M. and W. Ho (1995), “*State resolved studies of photochemicals dynamics at surfaces*”, Surf. Sci. Rep. **22**, 127 and references therein.
- Zacharias H., R. Schmiedl and K. H. Welge (1980), “*State selective step-wise photoionization of NO with mass spectroscopic ion detection*”, Appl. Phys. **21**, 127.
- Zhang, Y., Y. Wang (1998), “*Comment on “Generalized Gradient Approximation Made Simple”*”, Phys. Rev. Lett. **80**, 890.

## PUBLICATIONS

**Part of the present work has been published in the following article:**

Binetti, M., O. Weiße, E. Hasselbrink, A. J. Komrowski and A. C. Kummel (2000),  
“*Abstractive chemisorption of O<sub>2</sub> on Al(111)*”, Faraday Disc. Chem. Soc. **117**, 313.

Komrowski, A. J., J. Z. Sexton and A.C. Kummel, M. Binetti, O. Weiße and E. Hasselbrink (2001), “*Oxygen Abstraction from Dioxygen on the Al(111) surface*”, submitted.

## ACKNOWLEDGEMENTS

By the end of 1995, after a year at the *Centre for Surface and Low Temperature Physics* (CFSBT) at the University of Genova and an intense summer spent at the *Fritz Haber Institut* in Berlin, I started to consider the idea of pursuing my studies in physics in the field of surface science. For introducing me into the field of Surface Science and providing me with the opportunity to visit Berlin, I want to thank Prof. Dr. Mario A. Rocca.

Prof. Dr. Eckart Hasselbrink accepted me as a PhD student in 1996 and has been my supervisor during the last five years. During this period, I greatly profited from his deep scientific knowledge. I am thankful to him for his continuous support during the daily work in the lab, for answering my questions and improving my exposition's abilities, for his patience with my German and the chance he gave me to widen my knowledge of northern Europe.

I also want to thank Prof. Dr. Aart W. Kleyn for his interest in my work and for his willingness to evaluate this thesis.

Through our "scientific" wandering from Berlin, to Odense, to Essen, I came to know and appreciate Steven Wright's scientific skills and his dry sense of humour.

The time spent at the "Fritz" has been extremely productive and enjoyable thanks to Karl-Heinz Bornscheuer, Matthias Bittner, Olaf Dippel and Winfried Nessler. For the particular atmosphere reigning in that institute, as well as for his interest in my work, I am thankful to Prof. Dr. Gerhard Ertl. At that time, in order to solve whatever scientific and technical problem I encountered, I used to random-walk through the halls and dungeons of the institute. I usually ended up at Rolf Schuster's and Herbert Over's office and, more often than not, at the electronic workshop. Despite moving to Odense first and to Essen later, this state has hardly changed: here I want to thank Georg Heyne and Peter Zilske for reviving some old electronic control units, that I kept mistreating. With his lab's tips & tricks, his understanding of physics and his support, Rolf has always been of great help. Especially when I needed to understand what was I actually seen in otherwise nicely coloured STM pictures.

The active collaboration and friendliness of the whole staff at the Physics Department of the University of Southern Denmark in Odense, helped to transform the short period I spent there in a fruitful one. Gratefully acknowledged are the lively discussions with Claes Åkerlund, Arnd Baurichter, Lars Diekhöner and Prof. Alan Luntz.

Arrived in Essen, after unloading the truck, I sat fairly desperate in the new lab amidst boxes and UHV chambers. Elke Normann and Heinz Sprünken, and Dirk Gründer with them, were of great help in reversing this situation. Rebecca Reibke and Isabel Nieto introduced me to the subtlety of (Ruhr-)German language and into the artistic scene of Essen. For this and the ensuing vernissage parties, I will always be grateful. Isabel also endured proof-reading the manuscript. Eventual mistakes still present after her careful work, are entirely my fault. I hope they will not affect the general understanding of the text. Nils Hartmann's insightful remarks on AES, as well as his mastery in the preparation of "Feuerzangenbowle" were highly appreciated. For their work on the upgrading and characterization of the molecular beam source, I am thankful to Olaf Weiße and Kristian Laß. Ayse Neren Ökte helped me a lot to transform my scientific *new-speech* into a decent English. To Fritz Stricker I am particularly indebted for one

month of strenuous but successful efforts to repair the QMS. The lunch- and coffee-breaks have been treasured moments of relax, away from the noises of the lab, where valuable discussion about everything and the sense of life have been carried out, usually moderated by Dr. Ernst-Peter Röth and Wilhelm Dettmer.

I would also like to thank George Darling, for interesting remarks on the reliability of first principles and semi-empirical calculations, and Andrew Hodgson and Kurt Kolasinski for useful suggestions on the calibration of REMPI spectrometers.

Partial financial support of the present work by the EU through the Human Capital and Mobility (HCM) network and the network on *Surface Photochemistry* sponsored by the Training and Mobility of Researchers (TMR) Programme is gratefully acknowledged.

I would also like to thank my parents for their moral and practical support throughout the (long) period of my studies.

Last but not least, I want to thank Ira for her close support throughout these five years.

---

## CURRICULUM VITÆ

### Marcello Binetti

Born on March 4<sup>th</sup>, 1965 in Brindisi, Italy.

Nationality: Italian.

1984-1990: Undergraduate studies in Physics, Bari University (Italy).

1991-1992: Reserve Officer in the Italian Navy.

1992-1994: Graduation in Physics : “*Etheroepitaxy of ZnTe thin films on GaAs (100) with MOCVD technique; effect of two alternative Zn precursors*”, Bari University.

1995-1996: Genova University - Genova (Italy): Graduate Course on Material Science and Technology;

Department of Physics of Genova University: Experimental studies in surface science (temporary collaboration);

Fritz-Haber-Institut - Berlin, GFR: studies on the dynamics of ammonia UV-photodesorption (E.E.C.-HCM Fellowship).

1996-1997: Fritz-Haber-Institut - Berlin (Germany): Graduated Student at the Physical Chemistry Dept. (Max-Planck Fellowship);

Supervisor: Dr. E. Hasselbrink.

1997-1998: Odense Universitet - Odense (Denmark): Graduated Student at the Physics Dept. (Danish Academy of Science Fellowship);

Supervisor: Lektor Dr. E. Hasselbrink.

Oct. 1998-: Essen University - Essen (Germany): Graduated Student at the Chemistry Dept. (Scientific Coworker; E.E.C.-TMR Fellowship);

Supervisor: Prof. Dr. E. Hasselbrink.

